6-12-2009

Material selection for the actuator design for a biomimetic rolling robot conducive to miniaturization

Zachary S. Dotson

Material Selection for the Actuator Design for a Biomimetic Rolling Robot Conducive to Miniaturization

By
Zachary S. Dotson

A Thesis Submitted in Partial
Fulfillment of the Requirements for the

MASTER OF SCIENCE
IN
MATERIALS SCIENCE AND ENGINEERING

Approved: June 12, 2009

CENTER FOR MATERIALS SCIENCE AND ENGINEERING
ROCHESTER INSTITUTE OF TECHNOLOGY

COMMITTEE SIGNATURE PAGE

Approved By:

Dr. Kathleen Lamkin-Kennard
Department of Mechanical Engineering

Signature: _____

Dr. Massoud Miri
Department of Chemistry

Signature: _____

Dr. Gerald Takacs
Department of Chemistry

Signature: _____

CENTER FOR MATERIALS SCIENCE AND ENGINEERING
ROCHESTER INSTITUTE OF TECHNOLOGY
JUNE 2009

********** REPRODUCTION PERMISSION STATEMENT **********

Permission Granted

MATERIAL SELECTION FOR THE ACTUATOR DESIGN FOR A BIOMIMETIC ROLLING ROBOT CONDUCIVE TO MINIATURIZATION

I, Zachary S. Dotson, hereby grant permission to the Wallace Library of the Rochester Institute of Technology to reproduce my thesis in whole or part. Any reproduction will not be for commercial use or profit.

JUNE 12, 2009. Signature of Author: _____

ABSTRACT

The purpose of this thesis was to research, select, and test an actuator mechanism for ultimate use on a centimeter scale biomimetic rolling robot. The design of the actuator will allow a rolling motion that closely mimics cellular locomotion in addition to providing a novel motion for other applications.

The basis of the design has been completed through previous mechanical design research. The existing robotic mechanism consists of a larger scale spherical body with legs which controllably extend and contract, yielding a trajectory which results in a rolling motion of the body. The previous research also derived a mathematical model of the kinematics of the motion. The current work seeks to improve on the previous work by selecting an actuation mechanism that preserves the biomimetic motion and that allows this device to eventually be utilized at the microscale.

Material selection is of critical importance in developing actuation mechanisms at the microscale. Smart materials were extensively researched because of their actuation properties. Based on the strain percentage, power requirement, and force output, it was determined that the preferable actuation material was an electroactive polymer (EAP). Samples of Ionic Polymer-Metal Composite (IPMC), a type of EAP, were then fabricated, purchased, and tested. Test results from this work will enable future actuator designs and configurations to be fabricated with predicted results. This research also provided a basis for further mechanical design of the rolling robot with the incorporation of EAP actuators. Lastly, future work of combining sensors with the design, therefore compounding capabilities, of the rolling robot is discussed.

Table of Contents

Section ***Page***

Section ***Page***

Section ***Page***

List of Figures

Figure ***Page***

Figure *(Continued)* ***Page***

List of Tables

Table ***Page***

1. INTRODUCTION

Recent advances in MEMS (Micro-Electro-Mechanical Systems) devices have provided the technology necessary for many new applications, designs, and scales of devices used in the fields of engineering and research. One of these areas is in the use of robotics. These advances have specifically impacted the scalability of mobile robots. Recent technology has allowed the use of mobile robots for the use of exploration, reconnaissance, micro assembly, and medical devices. One of the most promising fields is the medical industry. Such technology could be used in drug delivery, diagnosis, and minimally invasive surgical techniques. However, even with the recent developments, many challenges still exist. For example, limitations of miniature robotics are power supplies, manufacturing of the mechanical designs, actuation mechanisms, and controllability [2,3,18].

1.1 Motivation of Research

The motivation of the rolling robot is to create a novel biomimetic robot that uses rolling as a method of locomotion. Most biomimetic robots are designed to model insects or human movements. There are many existing biomimetic robots [24, 25, 29]. However, most designs model jumping insects or crawling "bugs". For example, models of grasshoppers, centipedes, and spiders have been created using miniature robots [6,7]. This research focuses on the movement of lower level organism motion, such as cellular motion [7]. More specifically, this research is on modeling the rolling motion that closely mimics the locomotion of neutrophils within blood vessels. No biomimetic robot has been designed to model this type of motion. A

key requirement of this research is the ability for future work to miniaturize the design to the microscale for implementation into the human body [7].

1.2 Previous Research on the Rolling Robot

Background information on neutrophil cells and an overview of a rolling robot are provided in this section. For additional information, refer to Appendix A [7] and the research by Caputo [5].

1.2.1 Biological Background

Cell adhesion is an important phenomenon in many biological processes from neutrophil attraction near inflammatory regions to cancer metastasis [5]. Neutrophil rolling occurs during the inflammatory immune response and is how neutrophils are able to migrate from the blood stream along a blood vessel wall to the location of the infection [5,7]. Neutrophil rolling along the blood vessel wall is a key step in the inflammatory process [7].

During the inflammatory response, neutrophils are attracted to the blood vessel walls from the blood stream [5]. This attraction is due to molecular interactions. L-selectin on the surface of the neutrophil is attracted to intercellular adhesion molecule -1 (ICAM-1) on the surface of the endothelial cells lining the blood vessel walls. As pathogens enter the body, macrophages release cytokines [7]. One cytokine released is Tumor Necrosis Factor α (TNFα). Sensing the TNFα release, the endothelial cells, which line the blood vessel walls, begin to exhibit surface adhesion molecules [5,7]. These activated endothelial cells, near the pathogen [4], attract the neutrophils to the vessel wall [5]. Following the attraction, the initial adhesion of the neutrophils

to the blood vessel walls initiates the rolling of the neutrophils along the endothelial cells. Once the neutrophils are near the vessel wall, the surface adhesion molecules of the endothelial cells bind with glycoproteins on the surface of the neutrophils [7]. Only a small number of bonds form at the onset, and are easily broken with the shear force of the blood flow [7]. The repeated formation and breaking of the bonds are what cause the rolling motion of the neutrophil [7]. As rolling progresses, neutrophils are thought to be further activated by chemical signaling processes as a result of the transient binding to the vessel walls [5]. This is believed to contribute to the slowing of the neutrophils near the site of the pathogen. After a period of rolling, the neutrophil bonds become stronger as a result of the chemical signaling. Ultimately, the rolling motion is ceased as a result of strong bonds to the vessel wall [5]. Once firmly attached, the typically spherical neutrophils undergo a conformational change and undergo transmigration through the blood vessel wall into the surrounding tissue [5,7]. This is known as diapedesis [7]. Once in the tissue, the activated neutrophil is attracted to the infected region by chemoattractants. Figure 1 depicts the process flow.

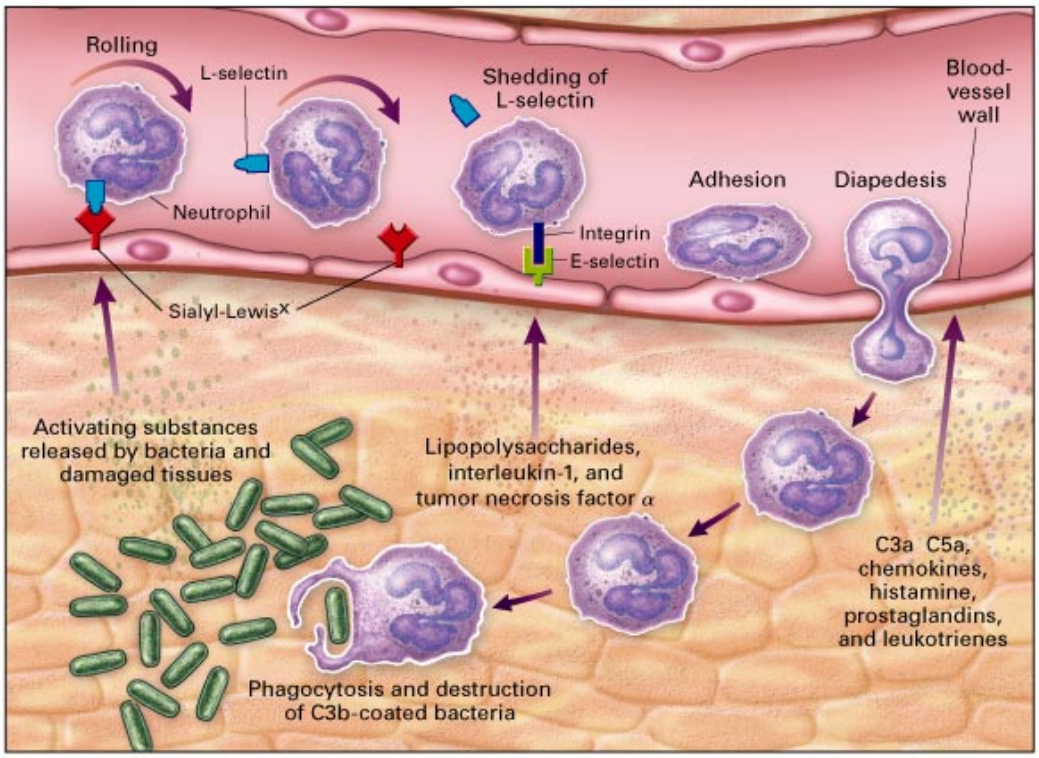

Figure 1. Depiction of neutrophil rolling, adhesion, conformational change (diapedesis), and encapsulation of bacteria which caused the acute inflammatory response [8].

1.2.2 Mechanical Design and Kinematics

Previous research has been conducted on the mechanical design of a large rolling robot [7]. The research focused on a spherical mobile robot designed to have superior structural and maneuverability properties [7]. Furthermore, important design objectives included fabrication by micro-fabrication techniques without limiting the mobility, and also minimizing sensors, actuators, and power requirements. The design, shown in Figure 2, has the following design characteristics [7]:

1. Four legs that form a regular tetrahedron. Increasing the number of legs will produce a smoother motion, yet increase complexity of sensing, actuation, and hardware required.

2. Unlike other rolling robots, the propulsion mechanism is external to the spherical core, but will require a more advanced computational control system. Other rolling robots have the means of propulsion in the interior of the spherical shell.

3. The rolling robot does not require a particular starting orientation. This preserves the true arbitrary posture of the robot.

4. The design relies on surface contact and friction as opposed to a weight unbalance to generate the propulsion moment.

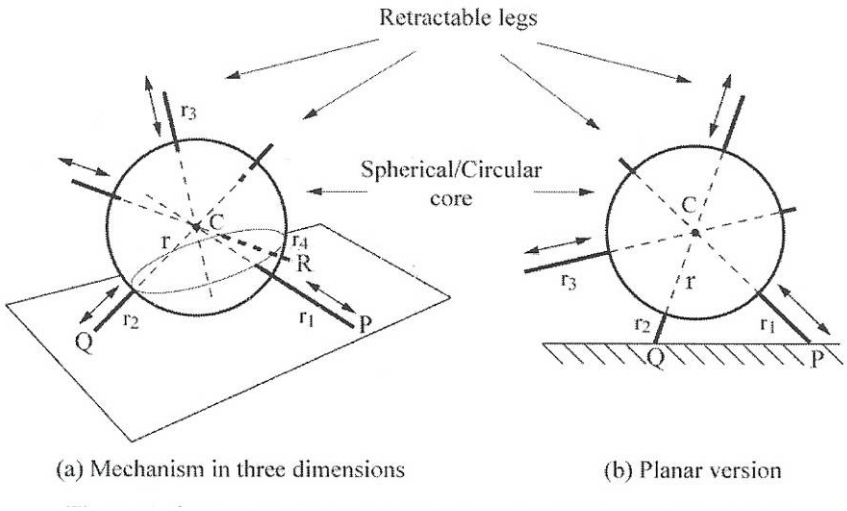

Figure 2. Schematics of the 3-D (left) and 2-D (right) rolling robot proposed by Dr. Das. [7].

Improvements to the original design could include adding degrees of freedom to the appendages. With the addition of rotational degrees of freedom to the linear motion of the first design, the robot could perform even in a varying environment, and ultimately, the human body. A spider-like movement could result from the addition of rotational degrees of freedom as shown in Figure 3 [7]. To optimize the functionality of the improved design, a thorough investigation of materials and fabrication techniques must be conducted [7]. Investigation of materials for design optimization is the focus of this thesis.

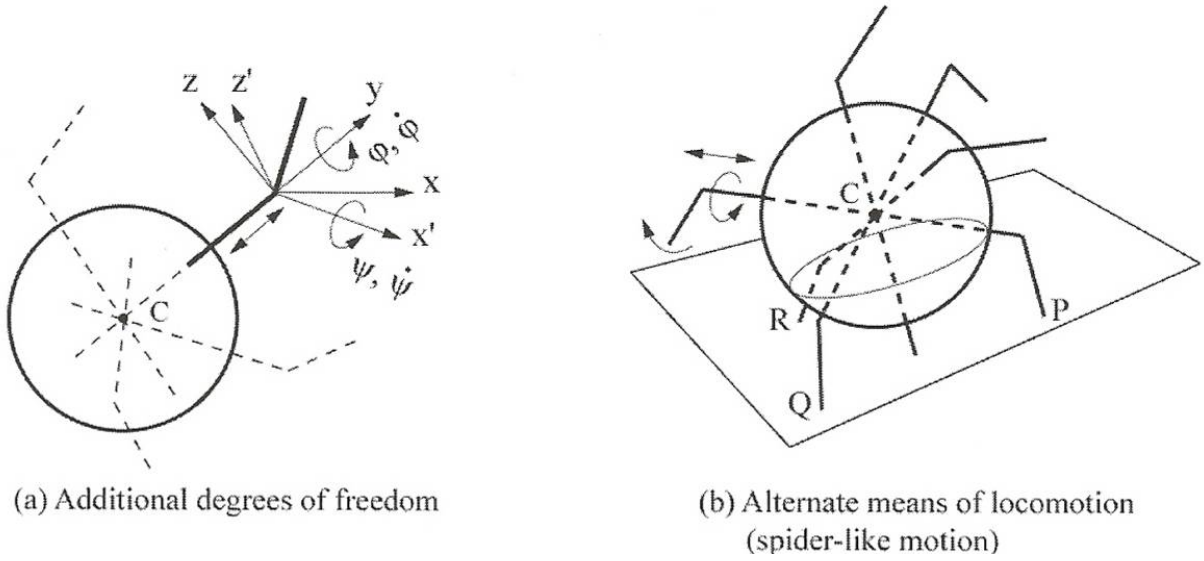

(a) Additional degrees of freedom

(b) Alternate means of locomotion (spider-like motion)

Figure 3. Schematics of the addition of rotational degrees of freedom (left) giving rise to the spider-like motion [7].

2. THEORY

In recent years, the size of many consumer goods has decreased as new technologies are developed and applied to various industries. Computers, cell phones, digital cameras, and medical equipment are just a few examples. Minimally invasive surgery relies on such miniature technologies that allow their passage through veins or arteries during surgical procedures [28].

However, electronics and electromagnetic mechanisms have limits for scalability and lose efficiency as their sizes decrease. This problem has led to more research in the area of new actuator technologies to overcome this scaling issue. Some of the new types of micro-actuators include piezoelectric, electrostrictive, magnetostrictive, electroactive polymers, and shape memory alloy (SMA) mechanisms [28].

As micro-robots are reduced in scale, problems are also encountered as the motion mechanisms are scaled down. Some of these mechanisms are very complex in design, involving many integrated parts. Therefore, the manufacturing of these mechanisms becomes increasingly difficult [33].

2.1 Biomimetic Robots

Biomimetic robots have been a popular area of research for many years, but more recently advancements in technology have allowed for unique designs and new applications. Many robots have been developed to mimic the movements of higher level organisms such as fish, insects, spiders, and humans. However, very few biomimetic robots have been inspired by low level organisms.

Back in 1970, a crayfish and lobster inspired robot was designed at Northeastern University. Uniquely implemented, the actions of real lobsters were programmed into the robot to allow realistic movements and actions [25].

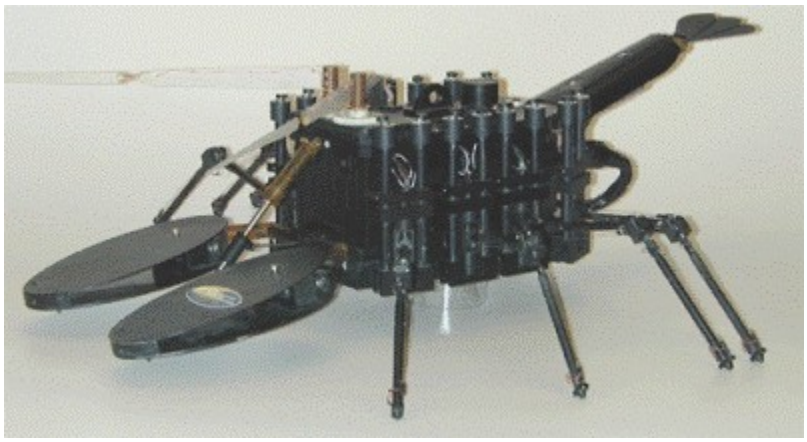

Figure 4. Lobster robot designed at Northeastern University in 1970 [25].

Figure 5 shows a low mass muscle gripper with fingers made from Ionic Polymer Metal Composite (IPMC). The gripper can lift a 10.3 gram rock using 5V with four IPMC fingers. The total weight of the IPMC fingers is a mere 0.4 grams [29].

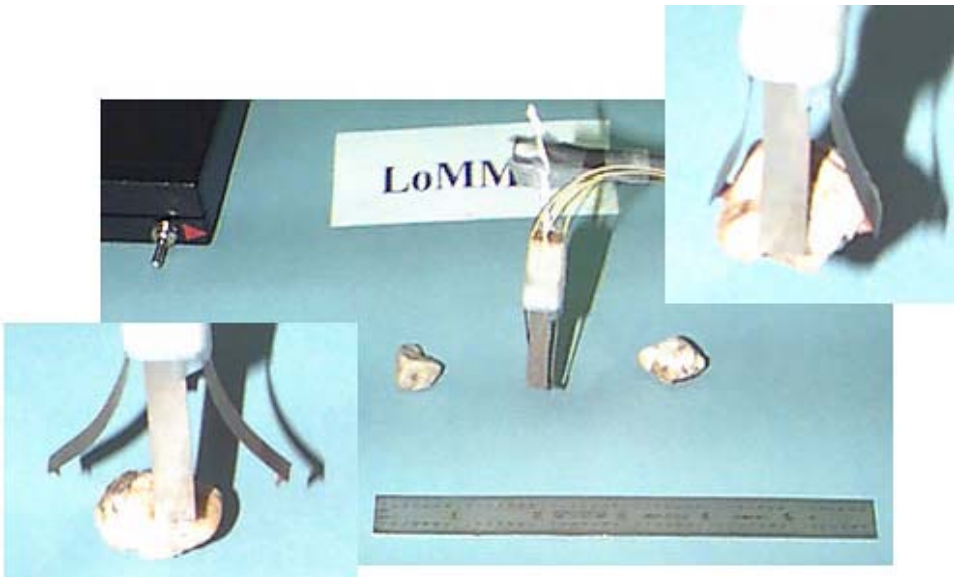

Figure 5. Microgripper made from an Ionic Polymer Metal composite actuators [29].

Using an IPMC actuator with a frequency of 5Hz, a noiseless swimming robot was fabricated [29]. Figure 6 shows frames of the robot swimming at 1/3 second intervals. A cilia-like robot was also designed utilizing IPMC artificial muscles (Figure 7) [29]. This robot mimics the movement of coral reefs, and has potential applications in the prevention of bio-fouling [29].

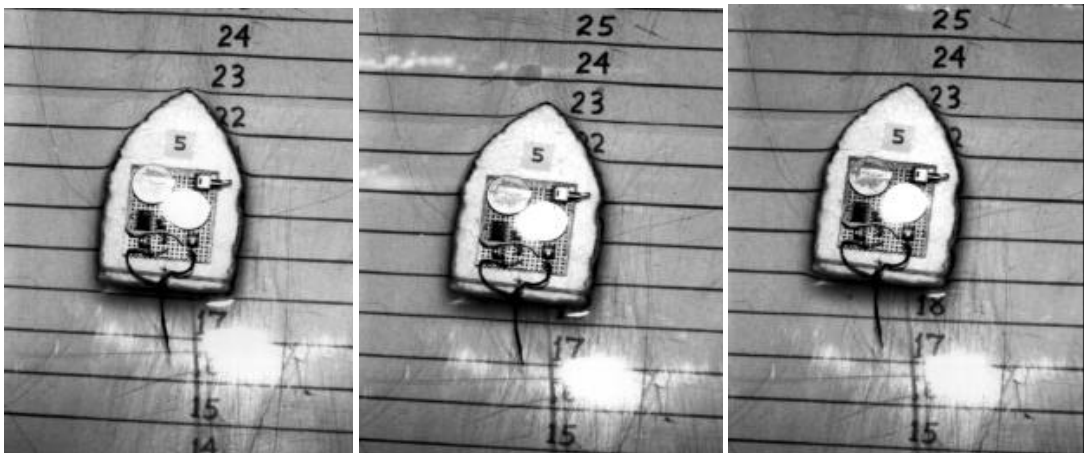

Figure 6. Noiseless swimming robot [29].

Figure 7. Cilia-like assembly of IPMC actuators to simulate coral reefs [29].

The iSprawl, shown in Figure 8, was inspired by the cockroach and designed by the Center for Design Research by Stanford University. iSprawl is about 11 centimeters in length, yet can move at over 2.3 meters/second [25]. iSprawl utilizes an electric motor that powers reciprocating legs [25].

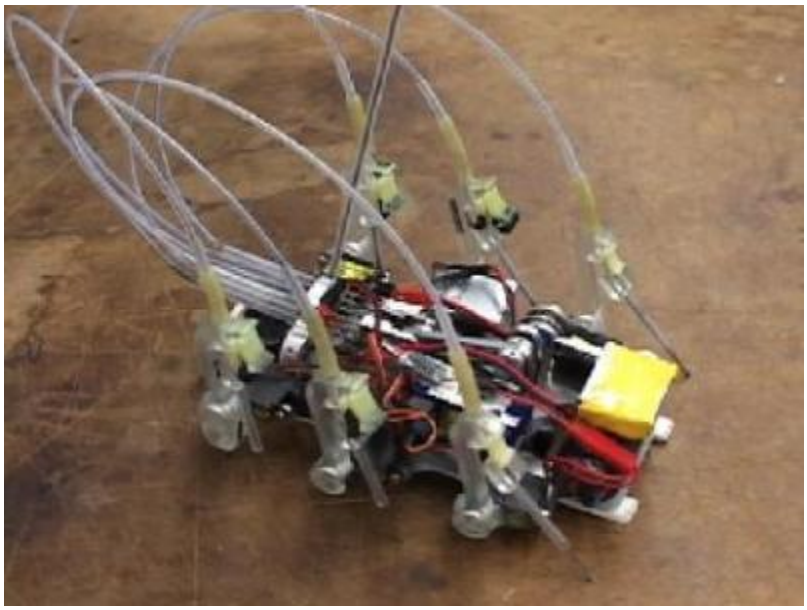

Figure 8. iSprawl [25].

The Center for Biologically Inspired Robotics Research at Case Western Reserve University has developed several robots based on biological organisms. One robot under development is the micro-cricket. This micro-robot, once completed, will be no longer than 5cm in length. The cricket robot can both walk and jump. A second robot is the Mini-Wheg™ which is based upon a spoke-like wheel drive. The unique feature of this robot is the ability to negotiate terrain with obstacles much larger than the diameter of the "wheels" [24].

Figure 9. Robotic Cricket designed at the Case Biorobotics Lab [24].

A climbing Mini-Wheg™, shown in Figure 10, makes use of adhesive pads attached to the rotating legs. The sticky additions permit the climbing of smooth vertical surfaces such as glass [24].

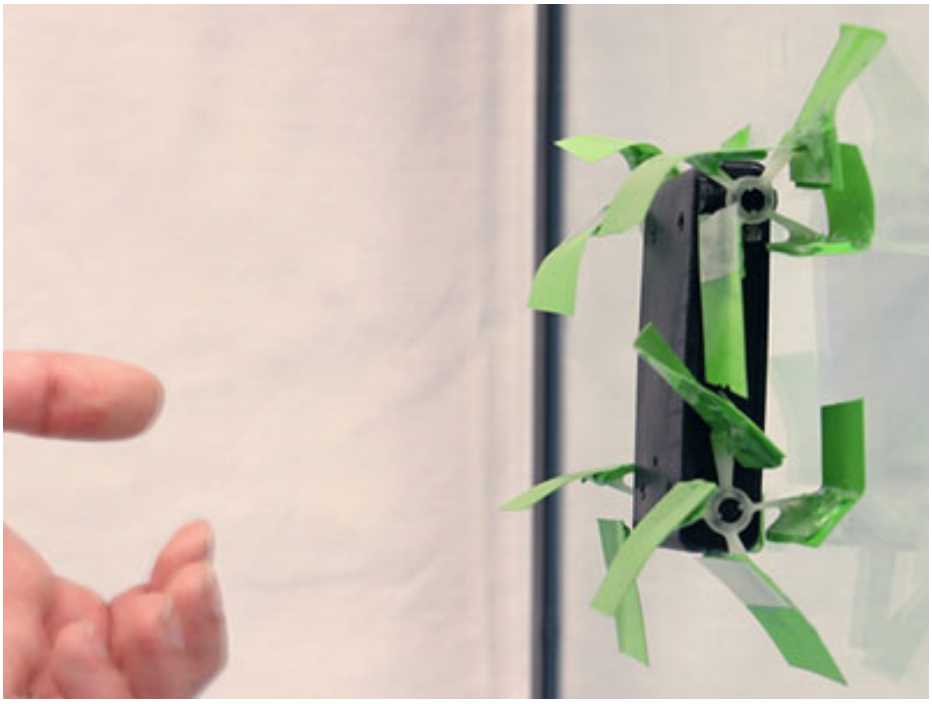

Figure 10. Climbing Mini-Wheg™ ascending glass [24].

The most unique biomimetic robot developed by the Case Western lab is the Softworm, shown in Figure 11. This robot uses the same locomotion as earthworms. The locomotion, known as peristalsis, functions by using a braided mesh exterior to create fluid waves of motion along the robot body. Their design has earned Honorable Mention distinctions at the Research Showcase two years in a row [24].

Figure 11. The Softworm using peristalsis to generate motion [24].

2.2 Actuation Mechanisms

As previously discussed, a wide range of actuation mechanisms have been implemented in robotic designs. Electric motors, solenoids, smart materials, and many others have been utilized depending on the application. The goal of this research is focusing on an actuation mechanism to mimic a low-level organism that can be fabricated at a small scale. The ultimate goal is micro-scale fabrication, thus this research will neglect mechanisms used primary for larger scale robotics. The focus here will be on "smart materials" that have potential of fulfilling the design requirements of the biomimetic rolling robot at various scales. The smart materials that are most promising for the rolling robot, as determined by preliminary research and existing biomimetic robot designs, include:

1. Shape Memory Alloys.

2. Piezoelectric Materials.

3. Electroactive Polymers.

2.2.1 Shape Memory Alloy Actuators

First discovered by the US Navy while developing new materials for submarines, Nitinol (Nickel Titanium Naval Ordinance Laboratory) is a shape memory alloy consisting of nickel and titanium in near 50-50 ratios. It is also referred to as NiTi and TiNi with the dominate element conventionally listed first. The ability of this alloy to be largely deformed and then upon heating, it will return to its original shape. This alloy has both the shape memory properties as well as super elastic properties [1,4]. The internal structure of phases is the driving force of SMAs. While at low temperatures, the SMA is in the martensite phase and can be deformed. Next, the strain imposed by the deformation is then recovered through heating the material. Cooling the sample will not reverse the process to the sample's original shape. Deforming a SMA slightly above the martensitic formation temperature during cooling initializes stress-induced martensite formation. Afterwards, when the induced stress is released, the martensite disappears resulting in a super elastic stress-strain hysteresis. This is caused by the stress-induced martensitic transformation. The super elasticity of NiTi permits reversible deformations with strains up to 10% due to the stress-induced phase [11,20]. As the load is removed, this stress-induced phase becomes unstable and reverts back to its original shape. The main difference between these two properties of shape memory and super elasticity is that super elasticity does not require a temperature gradient to return to its original shape. With the advantages of these two properties,

SMAs have many industrial and medical uses [20]. Advantages of SMAs include good mechanical properties, corrosion resistance, diverse applications, and biocompatibility [11,31].

Shape memory alloys permit three distinct functions- shape memory, super elasticity, and high dampening capabilities [4,28]. The ability of this class of materials to demonstrate such unique properties lies in the complex microstructure. A thorough explanation is necessary to understand how and why the macroscopic properties function [28].

The shape memory effect is due to the phase transitions between martensite and austenite [4,11,28]. This process begins when a SMA is deformed in the low temperature (martensite) phase. After heating the deformed sample to the high temperature (austenite) phase, the sample returns to its shape prior to deformation. Both the austenite and martensite have start and finish temperatures denoted by A_s, A_f, M_s, and M_f [28]. Shown in Figure 12 shows the process flow of SMAs.

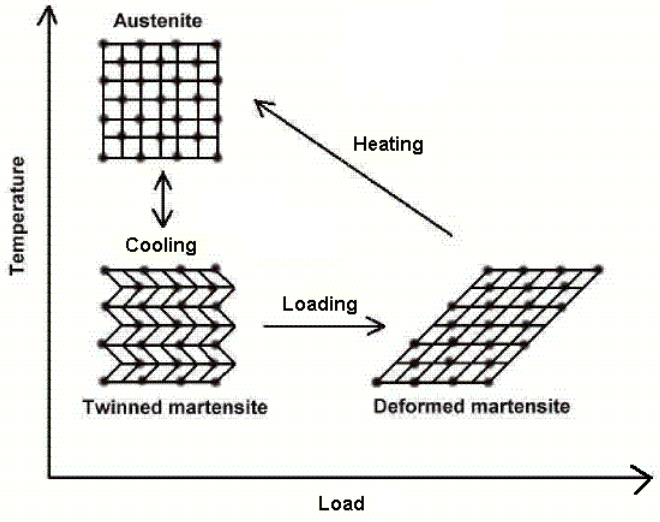

Figure 12. Microscale changes during the SMA effect [31].

An example to illustrate this effect is to consider a strip that when in the austenite (memorized shape) phase. As a force is applied below the M_f temperature and if it is great enough to detwin the martensite, the strip undergoes plastic deformation. Therefore, when the force is removed nearly all plastic deformation still exists. Next the deformed sample is heated above the A_f temperature. This allows the sample to transform to the austenite phase and recover to its original flat shape. Further cooling however does not invoke any shape change. This example demonstrates what is known as a "one-way" shape memory effect, because the sample remains in the austenite shape when cooled repetitively below M_f. This is due to the creation of randomly oriented martensite during cooling. The martensite structure has the same macroscopic volume as the austenite structure. A plastic deformation in martensite is needed to cause the "detwinning" resulting in a shape change during a heat treatment to the austenite phase [28].

The super elastic property of SMAs is caused when the application of a stress at a constant temperature causes the martensitic transformation [4,28]. As a material in its austenite phase at a constant temperature is under a load, the mechanical transformation is limited to elastic deformation until the critical stress limit where the transformation initiates. Then at the critical stress, the stress remains constant and the strain increases. This continues until the strain reaches about 8% (in single crystals up to 15% or more). Once the austenite has been transformed to martensite and the load is removed the material shows a hysteresis. This occurs at a constant temperature; however, it is important to note that the critical stress level where the strain begins to increase is temperature dependent [28].

Shape memory alloys have a unique property, known as damping, which allow the material to dissipate energy. The dissipation of energy is a result of the large number of dislocations that occur during martensitic transformation between martensite variants and the austenite matrix. Also, in the martensite phase SMAs have high damping abilities that result in the internal friction of martensitic variants. SMAs are also unique in that their damping abilities do not affect important mechanical properties like other common damping metals [28].

There are many types of shape memory alloys, but there are three main classes that are commercially available: Cu-Zn-Al, Cu-Al-Zn, and Ni-Ti-X (where X denotes another element such as Cu, Pd, or Hf). The following is a list of some common shape memory alloys [1]:

Titanium-palladium-nickel	Iron-manganese-silicon
Nickel-titanium-copper	Nickel-titanium
Gold-cadmium	Nickel-iron-zinc-aluminum
Iron-zinc-copper-aluminum	Copper-Aluminum-Iron
Titanium-niobium-aluminum	Titanium-niobium
Uranium-niobium	Zirconium-copper-zinc
Hafnium-titanium-nickel	Nickel-zirconium-titanium

Ni-Ti alloys have the most desired properties. Ni-Ti alloys are very ductile (30-40%) which allows for easy shaping without breaking caused by brittleness. Also, they have a high level of biocompatibility which is widely exploited in the medical device industry. Finally, they exhibit a high level of electrical resistivity which provides the basis of efficient activation by Joule heating. Table 1 compares Ni-Ti and stainless steel properties [28]. A comprehensive table

containing many different compositions of SMA metals and their material properties are provided in Appendix B [10].

Table 1. Mechanical Properties of Ni-Ti vs. Stainless Steel [28].

Property	Ni–Ti	Typical Data for a Stainless Steel
Max. Reversible Elastic Deformation	Typ. 8%	0.8%
Mass Density	6450 $kg.m^{-3}$	7850 $kg.m^{-3}$
Young's Modulus (*E*)	M: 28–41 GPa A: 83 GPa	190–210 GPa
Shear Modulus (*G*)	M: 10–15.5 GPa A: 31 GPa	75–80 GPa
Poisson's Ratio (*v*)	0.33	0.27–0.30
Yield Stress[a]	A: 195–690 MPa M: 70–140 MPa	400–1600[b] MPa
Ultimate Stress	895–1900 MPa	700–1900 MPa
Coefficient of Thermal Expansion	A: 11 × 10^{-6}/◦C M: 6.6 × 10^{-6}/◦C	(8–10) x 10^{-6}/◦C

Notes: "M" refers to martensite and "A" refers to austenite.
[a]The yield stress for the SMA is not really a yield stress but rather a critical stress to induce martensite when in the austenitic state and a critical stress to reorient martensitic variants when in the martensitic state.
[b]These values apply typically to a spring steel.

Some Ni-Ti alloys undergo an additional "martensite-like" transition. The transition is referred to as the R-phase transition. The R-phase transition occurs during cooling before the martensitic transformation under only certain conditions of the material fabrication and processing. The R-phase results in a very narrow hysteresis (about 1.5^{o}C) and great thermal cycling stability. The narrow hysteresis and cycling stability make Ni-Ti even more applicable for actuator designs. However, the strain is limited to about 1% [28].

One of the many uses that exploit the properties of SMAs is in actuation mechanisms. SMAs are attractive for this application because many actuation other mechanisms do not scale down to the micro- and nano-scales. The ability of SMAs to perform at these scales is very attractive for actuation designs. However, certain design principles must be considered based on the material properties [28].

Shape memory alloys (SMAs) are great material choices for biomedical applications due to their biocompatibility [11,20,31]. Shown in Figure 13 are SMA cardiovascular stents. SMAs show high biocompatibility even with 50 mol% Nickel in their compositions. Nickel can give rise to sensitivity complications when used on or within the body. However, no cases have been reported of nickel sensitivity due to SMAs [20].

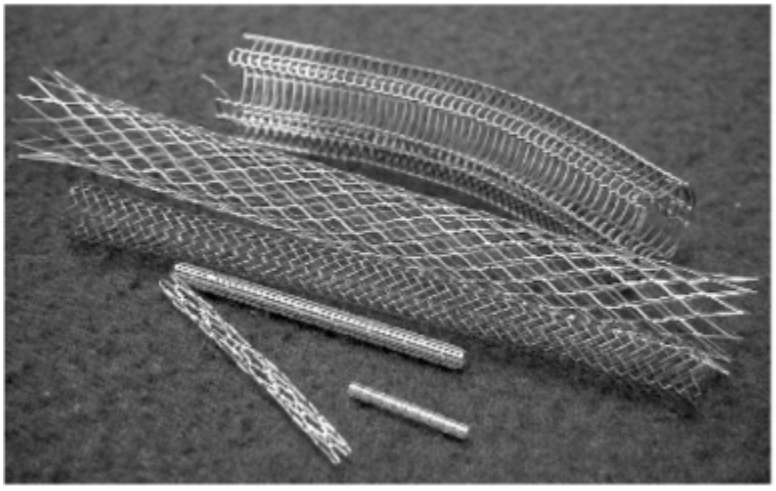

Figure 13. SMA self-expanding stents [15].

Shape Memory alloys have complex thermo-mechanical behaviors which include nonlinear, dissipative, and temperature dependent mechanical properties. In turn, design methodologies based on linear mechanics such as Castigliano's theorem and the superposition principle can only be applied in the elastic case. However, isothermal characteristics can be modeled appropriately when an elastoplastic model is used [28].

Since the shape memory property is a "one-way" effect by itself, it is not appropriate for actuator purposes. In order to overcome this impasse, there are two processes that can be added. The first method requires the material to be trained through thermo-mechanical treatment or manufacturing processes to be reversible without any outside influence. The second is to make the material reversible through the addition of a biasing component. This bias supplies the energy necessary to return the martensite to its original configuration during cooling thus completing one full cycle [28]. With that, there are two primary classifications of shape memory

alloy actuators: reversible with external bias and reversible with internal bias. SMA actuators require some bias force to restore the actuator to the starting orientation. The external bias can be a constant force, spring-biased, or antagonistic force. The internal bias can be a two-way shape memory effect, "all-round" effect, or can occur as a result of irradiation [28].

The most basic actuator design using SMAs consists of an SMA working under a constant force. This constant force automatically serves as the outside bias or restoration force. By examining the intersections of the austenitic and martensitic characteristics and the straight line denoting the force level, the stroke can be determined. The stroke is the displacement the SMA actuator is capable of providing. For an actuator that is mechanically constrained during the transition to the austenite phase, the recovery stresses form at a constant rate until the yield strength of the material is reached. Using this property, a design can be made that has a gripping force almost independent of the tolerances of the object being grabbed. The stress is also well defined. For SMAs, the force remains constant when the SMAs have at least 1.5% unresolved recovery [28].

The spring-biased design relies on some spring element to exert a force on the SMA. The spring element must apply sufficient force necessary for the recovery of the deformation of the SMA. The spring bias must have some elastic property to enable this. Here the SMA is formed and pre-stressed while in the martensitic phase. Then, as the material is heated to its austenitic phase, it generates a recovery force as it returns to its original shape. This, in turn, exerts force on the bias spring which has elastic energy. During cooling, the opposite transformation occurs. The Young's modulus of the SMA decreases and martensite forms. Also, the elastic energy of

the spring bias induces the reorientation of martensite. This ends in the overall deformation of the SMA [28].

Often referred to as a "push-pull" design, the antagonistic method utilizes two SMA components that operate in opposing directions. Again, the SMAs are deformed and pre-stressed in the martensitic phase. As the actuators are then independently heated to the austenitic phase, the heated actuator moves the opposing element, deforming it in the process. To reverse the motion, the opposite SMA actuator is heated. It is possible to supply one actuator at a time with power (heat), or one power supply can be biased between the two resulting in a different dynamic action [28].

For reversible actuators with internal biasing, there is the two-way shape memory effect [4,28]. The two-way effect must be taught to and learned by the material. In essence, the material memorizes a particular shape during the cooling steps. The shape memory effect results in an unassisted shape change. It is important to emphasize that this is not an intrinsic property of the material, thus the material must "learn" this effect. In order to learn this property, materials must be subjected to specific thermo-mechanical treatments. The basis of this effect is the presence of internal stresses resulting from the training of the shape. This allows a given organization of martensitic variants during cooling. The shape training process creates preferred martensitic variants. Two-way effect SMAs have a strain of 1-2%, but the force created during heating cycles is much greater than the forces of cooling cycles. This shortcoming limits two-way SMAs to specific designs and applications [28].

Another internal biasing is the "all-round" SMA effect observed in nickel rich Ni-Ti alloys where the Ni content is in excess of 50.6 at%. A flat strip is annealed in a round shape at a temperature above 673 K so that precipitates form. After the heat treatment, the sample in the austenitic phase will have a ring shape. In the martensitic phase, the sample will have the opposite ring shape. In other words, the outer part of the ring becomes the inner part and vice versa. Under compression, the precipitates from the annealing process are oriented perpendicularly to those precipitates in the segment of the material is under tension. As the material is cooled, the martensitic variants form due to the internal stresses caused by the precipitates. The matensitic variants results in the opposing round shape to form [28].

Another method of creating an internal bias in SMAs is neutron irradiation. Neutron irradiation prevents martensitic transformations in Ti-Ni alloys. Neutron irradiation can be used to create cantilever actuators by irradiating half of the beam thickness, leaving the other half unaffected. For the cantilever application, the neutron irradiation creates two distinct regions of the material. The unaffected zone acts as the actuator, and the irradiated region acts as the biasing element resulting in a bending motion. The two distinct regions of the SMA material resemble a bimorph structure [28].

The manufacturing process can also help designate which type of bias will be used. Certain material production methods create reversible effects in shape memory alloys. For example, melt spinning creates reversible effects under certain conditions. Another example is the production of Ni-Ti SMA films. The film method deposits successive layers of pure Ni and

Ti each 10-20nm thick. Then as heated, the Ni and Ti diffuse and form subsequent crystallization. The result of melt spinning is a two-way bending motion [28].

The time response of SMAs is one of the biggest limitations of this type of material. Only limited bandwidth can be achieved due to the thermal activation requirement. As mass decreases, such as in scaling down actuators, SMAs response time is increased. Table 2 shows some of these related properties of Ni-Ti in comparison to pure copper [28].

Table 2. Thermal Properties of Ti-Ni and Copper @ 300 K [28].

Property	Ti-Ni	Copper
Density	6450 kg/m^3	8933 kg/m^3
Thermal Conductivity	A: 18 W/m*K M: 8.6 W/m*K	401 W/m*K
Specific Heat	836 J/kg*K	385 J/kg*K

The basis of the lifetime of SMA actuators is rooted in the level of strain the actuator undergoes. For example, actuators working at their maximum potential of about 8% do not have the same lifetime of actuators working at lower strain rates. Lifetime of SMA actuators is an important design property that must be examined carefully for each application. Other lifetime factors include the specific alloy compositions, heat treatments, cold work, and loading speed [28].

There are also different types of fatigue in SMA actuators. First, fracture failure is caused by stress or strain while cycling at constant temperature. A second fatigue failure is due to changes in the physical, mechanical, and functional properties. A final type of failure is due to the degradation of the shape memory effect due to stress, strain, or temperature cycling in the transformation region. Many variables are involved in the lifetime of SMAs, thus it is difficult to generalize operating conditions. However, Table 3 has some expectations of the number of cycles with corresponding strain rates [28].

Table 3. Strain rate vs. # of cycles [28].

Number of Cycles	Strain (%)	Stress (MPa)
1	8	500
100	4	275
10000	2	140
+100,000	1	70

2.2.2 Piezoelectric Actuators

Another common actuation material is piezoelectric. Piezoelectrics are functional materials often associated with MEMS technology. The working principle is the transformation of electrical and mechanical energy. Since piezoelectrics can both detect changes and provide changes, they are able to act as both sensors and actuators. This property allows them to be commonly categorized as smart materials [4]. Piezoelectrics are most often used in sensing and micro-positioning applications.

Like any type of material, piezoelectrics have both advantages and disadvantages. Advantages of piezoelectrics include high force output, short response times, low noise, and high

sensitivity. However, the disadvantages include high voltage requirements, very small displacements, and quasi-static sensing [4,33]. Voltage requirements are often in the 10-100 kV range, making piezoelectric actuators difficult for small scales and untethered robots.

Piezoelectric materials are manipulated upon the application of an electric field. Application of an electric field results in the material expanding and contracting [4,21]. Furthermore, when a piezoelectric material is subjected to a mechanical force, an electric field is produced across the material due to the asymmetrical crystalline structure [33]. Conventional piezoelectric materials are limited to about 0.1% deformation. That is, for a 5cm robot appendage, the movement is only 50μm with an applied voltage of 100 kV. The limited range of movement can be enhanced through design features such as cantilevers to achieve more desirable results [33].

Piezoelectric materials can be natural, ceramic, and polymeric. Natural piezoelectric materials include quartz, seignette, and turmalin. Ceramic piezoelectrics include lead-zirconate-titanate (PZT) and lead-magnesium-niobate (PMN). Ceramics piezoelectrics are appealing for many applications as they can be engineered to best suit the properties desired. Polymer piezoelectric materials also exist. Poly-vinylidene fluoride (PVDF) is one example of a piezoelectric polymer [28].

Classification of piezoelectric actuators is typically done by the piezoelectric coefficient utilized by the actuator [32].

- d33- This is a 33 mode actuator that generates a displacement in the same direction as the electric field that is applied parallel to the actuator material's polarization direction.
- d31- This is a 31 mode actuator that generates a displacement normal to the applied electric field that is parallel to the material's polarization direction.
- d15- This is a 15 mode actuator that utilizes the shear strain from the electric field when applied normal to the material's polarization direction.

A d33 actuator can produce nearly twice the strain than a d31 actuator with an identical applied voltage because of the magnitudes of the two different piezoelectric coefficients. The d15 actuators are not as common because of their difficulty to manufacture [32].

There are many different piezoelectric actuator designs, but arguably the three simplest designs include the bimorph, multilayer, and cylindrical actuators. Bimorph actuators are constructed by two layers which operate in d31. These actuators produce large displacements, but they have low output forces.

In order to overcome the low force output, bimorph actuators can be layered together, forming multilayer actuators. Essentially, the bimorph actuators layers are combined in parallel with all the other layers. Thus, the displacements of each layer sum together. Advantages of the multilayer design include the ability, at a given voltage, for the total strain to be multiplied by the number of layers in the structure. This is N (number of layers) greater than the strain produced by a single layer bimorph design of the same overall dimensions. Another advantage is that the

voltage will be N (number of layers) times lower for the multilayer than a single bimorph of the same dimensions. In general, it is desirable to use many thin layers in order to reduce the operating voltage [32]. Lastly, cylindrical designs operate in d31 with an applied voltage across the walls of the cylinder resulting in the elongation of the cylinder. The cylindrical design, often used for precision positioning applications, is shown in Figure 14 [22].

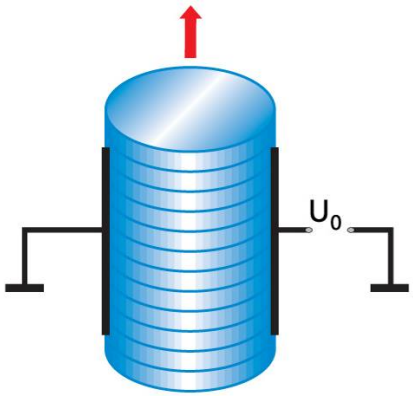

Figure 14. Cylindrical piezoelectric actuator [22].

2.2.3 Electroactive Polymer Actuators

Electroactive polymers (EAPs) have some unique material characteristics. These properties, such as high stress and energy density, preventive damage operation, large actuation strain, and fast response times, have attracted the attention from many fields and industries. The unique material properties associated with EAPs, have led to their successful use as actuation mechanisms. EAPs demonstrate superior properties and may soon replace many actuation mechanisms currently in use [19].

The use of EAPs as artificial muscles is a very popular area of research. EAPs have been modeled as both capacitive and resistive actuators, behaving much like biological muscles. The similarity of EAPs to biological muscles has evolved the development of biomimetic robots and biomechanical applications. One of the most popular EAPs for robotic and biomechanical applications is the ion-exchange polymer-metal composite (IPMC). The ability of IPMCs to operate in wet, humid, or even dry environments if correctly designed, allows for a wide range of applications [29].

EAPs are being utilized in devices not previously possible due to restrictions on size and effectiveness. Systems such as surgical micro-robots, artificial muscles and organs, and biomimetic devices are now possible with the implementation of EAP actuators [19].

The basis of EAPs lies in the use of polymers which expand and contract when electric or magnetic fields are induced in the material. Other similar polymers used in artificial muscles make use of stimulation by light, pH change, and temperature change. EAPs are often divided into two main categories with respect to the activation mechanism [19]. Respectively, they are Dry (electronic) EAPs and Wet (ionic) EAPs.

2.2.3.1 Dry EAP

Dry EAPs are activated by electrical stimulation. These polymers are for use in dry environments. Dry EAPs include dielectric elastomer actuators (DEAs), electro-viscoeleastic elastomers, electrostrictive graft elastomers, ferroelectric polymers, and liquid crystal elastomers (LCEs). Dry EAPs allow high mechanical energy densities, and under a DC voltage can hold a strain. The practical limitation to electronic EAPs is the high voltage (>1 kV) necessary for

actuation. Three of the best studied and most promising dry EAPs are the dielectric elastomer actuators (DEAs), electrostrictive relaxor ferroelectric polymers, and liquid crystal elastomers [19].

DEAs function by the application of an electric field. A DEA consists of an elastomer sandwiched between two electrodes. As a voltage is applied to the electrodes, the thickness of the elastomer is then increased or decreased depending on the bias of the voltage. In other words, the DEA appears to be "squished" or "pulled apart" by the electodes. Advantages of DEAs are simple construction, high efficiencies, moderate bandwidths (over 1kHz in silicon), operation over large temperature ranges (-100^{o}C to 250^{o}C in silicone and -10^{o}C to 90^{o}C in acrylic elastomers), and high strain rates (up to 380%). These properties have been utilized with the implementation of DEAs in systems that function as electroactive fluid pumps, spring roll actuators for insect robotics, and heel-strike generators in shoe soles [19].

Ferroelectric polymers are a subclass of electronic EAPs. Ferroelectric polymers are characterized by dipoles attached to the backbone of the polymer chain. Those dipoles are then able to be aligned by electric fields, producing polarized regions. The polarization is responsible for contractions of up to 10% in the direction of the electric field. Hysteresis effects can be avoided by creating imperfections by irradiation or also by a small mass of bulky monomers. The result of the imperfections is the reduction the Curie point below room temperature, thus preventing the creation of large ferroelectric regions. Also, the imperfections reduce the energy barrier of the phase change between nonpolar and polar phases. Ferroelectric polymers that exhibit polar and nonpolar phase change are known as relaxor ferroelectric polymers [19].

Advantages of ferroelectric polymers include strains of up to 10%, high stresses (45MPa), energy densities of 1 MJ/m^3 (similar to DEAs), and good electromechanical coupling (0.42). However, disadvantages include the high voltage (>1kV), large energy dissipation, and limited temperature range. Ways to reduce the activation voltage requirements include reducing the thickness or increasing the dielectric constant [19].

2.2.3.2 Wet EAPs

Ionic EAPs (often referred to as "wet" EAPs) function by having an electrolyte between two electrodes. As a voltage is applied to the electrodes, the ions in the electrolyte move thus creating a macroscopic bending of the actuator. There are several different types of ionic EAPs: ionic polymer-metal composites (IPMCs), carbon nanotubes (CNTs), conductive polymers (CPs), electrorheological fluids (ERFs), and ionic polymer gels (IPGs). The advantages are the ability of these EAPs to undergo large bending displacements, allow polarity dependent bi-directional actuation, and low activation voltages of less than 2V. Disadvantages of ionic EAPs include low electromechanical coupling and evaporation of the electrolyte in air [19]. Since these actuators are light and soft, depending on the thickness, the actuator responds rapidly and with a large displacement with low voltage [9].

Compared to previously discussed actuation mechanisms, polymer based composites provide many advantageous characteristics. Most commonly used, IPMC strips are found to be superior to any similar actuation mechanism existing. IPMC actuators rely on the metal acting as an electrode as a voltage is applied. Their results yield high accuracy and repeatability [29]. The

motion control is dependent on the shape of the polymer and is electrically controlled. Another unique characteristic is that the actuator is totally silent. The actuator is also lightweight and can be made very thin (about 0.1 mm). These properties are most useful for the scalability of miniature robotics and other applications. Furthermore, the shape and design of these actuators provide nearly limitless movement arrangements. Different shapes and sizes combined together can result in many different movement configurations. The versatility of IPMCs allows for the replication of movements by living organisms. Biomimetic movement was not previously achieved with SMA or piezoelectric actuation mechanisms. Another feature of IPMCs is the ability for actuations to take place under low voltage (about 1-2volts), and also low power (0.05 to 0.2W) [9].

The operating principle of IPMCs is a bending motion, which is the most common form of actuation using ionic conducting polymers. The basis of this movement is rooted in the uni-directional electro-osmosis by cations with their polar solvent in the direction of the cathode. The depletion of solvent at the anodic side and the increase at the cathodic side respectively cause shrinking and swelling which results in the bending motion. Figure 15 depicts this process [9].

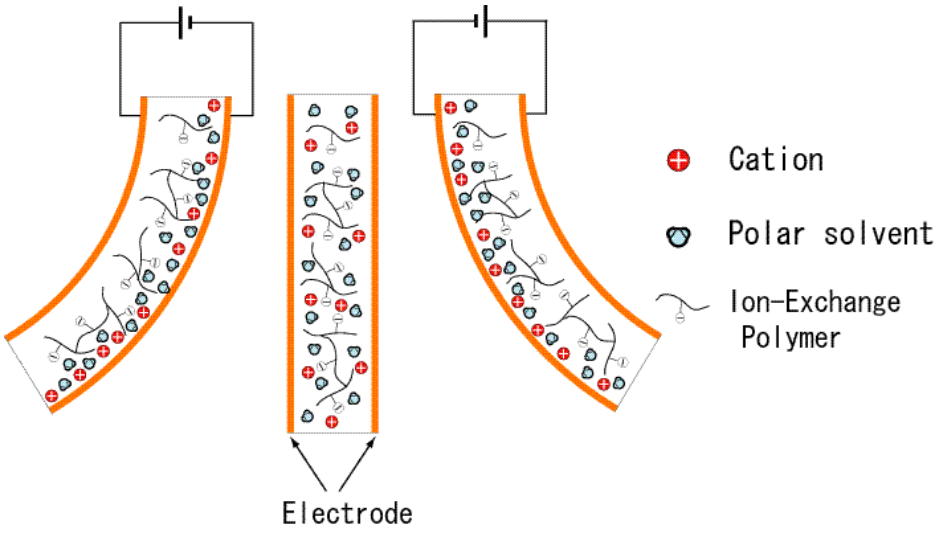

Figure 15. Ion Exchange Process [9].

Outlined below are the general design principles of electroactive polymers [9]:

- **Actuator size**: Generating power becomes large by enlarging thickness. The motion generated also depends on the shape of the cut or casted polymer film used.
- **Actuator shape**: The generation power depends on the rigidity of the actuator and the position of the fulcrum. Large power is generated if there are a lot of fulcrums. A tube actuator enables bending of all directions.
- **Ditch for electric insulation**: A curved direction can be controlled by making the insulation ditch. Moreover, because the resistance of each insulated actuator changes by making the insulation ditch, various movements can be made.
- **Two or more connections**: It moves in the counter direction respectively.

- **The kind of ion**: Because the displacement rate and the amount of displacement depend on the kind of the ion, it is possible to select it by the usage.
- **Control of operation**: The displacement, the displacement rate, and the position can be controlled by a low electric power.
- **Waveform of applied voltage**: The displacement rate can be controlled even by one cycle or less. Movements similar to the living organism are possible.
- **Position of lead terminal supplying electricity**: The voltage depends on the distance from the terminal because the actuator has a little electric resistance. Therefore, because displacement depends on the distance from the terminal. The movement can be controlled by the position of the terminal.

2.3 Actuator Selection for a Rolling Robot

In selecting the most appropriate actuation method for any application, several criteria must be satisfied. The most important factors include the necessary force outputs or strains, frequency range, stability, linearity, signal to noise ratio, power consumption, compatibility with the desired application, and ultimately cost.

Based on the material properties described previously, the two most promising candidates for rolling robot actuators were shape memory alloys and electroactive polymers. First, the properties of SMAs are superior compared to piezoelectric, mangetostrictive, and bimorph actuators. Table 4 compares SMA properties to other materials such as piezoelectric, magnetostrictive, conducting polymers, and bimorph actuators [28].

Table 4. Properties of SMAs vs. other Smart Material Actuators [28].

Property	SMA	Piezoelectric	Giant Magnetostrictive	Conducting Polymers	Bimorph Actuators
Physical Phenomena	Martensitic Transformation	Piezoelectricity	Magnetostriction	Electrochemical Doping	Differential Thermal Expansion Coefficient
Actuation Principle	Thermal	Electric Field	Magnetic Field	Voltage	Thermal
Energy Density (J/m^3)	10^6-10^7	10^2 (PZT)	10^4-10^5	10^3	10^5
Bandwidth (Order of Magnitude)	Low (10^2 Hz)	High (100 kHz)	High (100 kHz)	High (10 kHz)	Low (10^2 Hz)
Working Mode	Bending Torsion Tension	Dependent on Electric Field Direction	Dependent on Magnetic Field Direction	Electrolyte Storage Scheme	Bending
Typical Strain	1-8%	0.12-0.15%	0.58-0.81%	>10%	$5\text{-}23*10^{-4}$%/^oC

Next was a closer comparison of SMAs and electroactive polymers. These two materials were chosen based on their properties as compared to other actuators. When comparing material choices, the most important factors are dependent on the application, function, machinability, however the physical properties of the material choices allow for a direct comparison between materials. Table 5 compares properties of EAPs and shape memory alloys (SMAs) [3].

Table 5. Comparison of EAP and SMA Properties [3].

Property	Electroactive Polymers (EAP)	Shape Memory Alloys (SMA)
Actuation Strain	>10%	<8%
Force (MPa)	0.1-3.0	About 700
Reaction Speed	μsec-sec	sec-min
Density	1-2.5g/cm^3	5 - 6 g/cc
Drive Voltage	2-7V	N/A
Consumed Power	m-Watts	Watts
Fracture Toughness	Resilient, Elastic	Elastic

As shown in Table 5, electroactive polymers have highly desirable characteristics. Actuation strain, force, reaction speed, density, drive voltage, and consumed power are the most important characteristics. The requirements set forth by the rolling robot necessitate an actuation mechanism that has low power consumption for scalability, appropriate force output, and low drive voltage. From these requirements, the actuation mechanism most appropriate was chosen to be the electroactive polymers. Furthermore, electroactive polymers also provide fluid actuation movements that more closely mimic the natural movement flow found in nature. The

other actuation mechanisms were unable to demonstrate qualities that were superior to EAPs in neither properties nor the fluidity of movements. For example, the large actuation stain of greater than 10% for electroactive polymers provide more flexibility with the mechanical design of an actuation mechanism compared the limiting actuation strain of only 8% for SMAs. Additionally the low density of EAPs can provide lightweight actuators to help decrease the overall mass of the rolling robot. The reduction in mass will help offset the lower force output of the EAP actuators. Also, the reaction speed of EAPs is on the order of milliseconds whereas SMAs react on the order of seconds to minutes. Such slow reaction speeds of SMAs would result in very slow movements. EAPs, with the faster response time, can make faster actuations. Fast reaction speed is especially desirable for a rolling robot that utilizes several actuators that must work together in sequence. Most likely, the rolling robot with rely on multiple actuators to make one revolution. If individual actuators have slow response, increasing the number of actuators will result in an equally increased response time for one revolution of the robot. Lastly, yet most important for the miniaturization, is the drive voltage required. EAPs have the lowest voltage requirements of any of the researched actuators. Since miniaturization is an important consideration in this research, a low voltage requirement of the actuation mechanism is crucial.

With electroactive polymers selected as the actuation material, the previous research on the mechanical design of the robot must be capable of implementing EAP actuation. Figure 16 illustrates how the proposed robot design and EAP actuation can be combined.

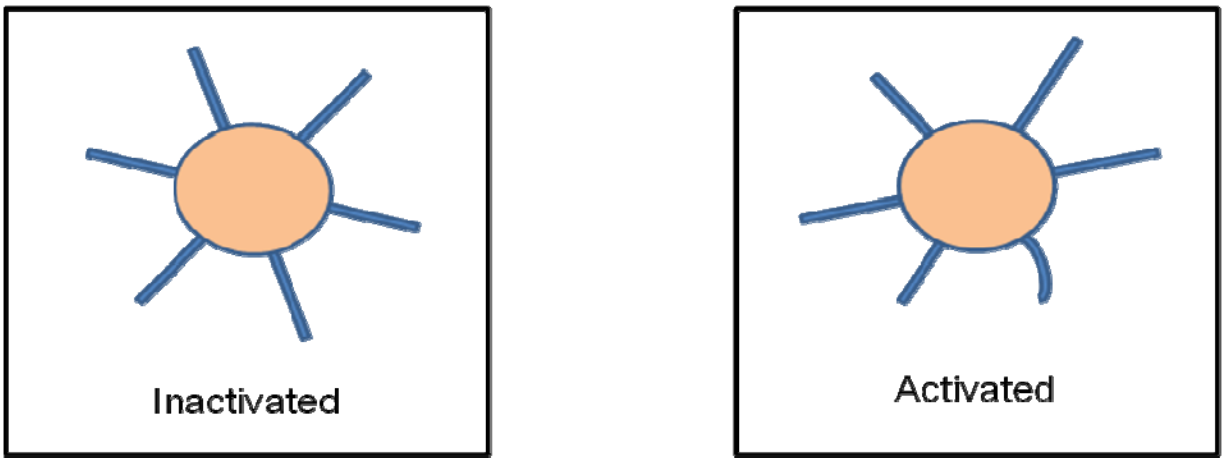

Figure 16. Rolling robot with EAP legs. On the left is the robot design with EAP appendages. On the right is the robot design with one activated EAP leg.

2.4 EAP Availability

Electroactive polymers are not readily available through commercial suppliers. The cost of manufacturing, along with quality and control of EAPs is not advanced enough to make EAPs viable for commercial use [9]. Several companies are currently refining their manufacturing process to overcome these issues [9]. However, some companies offer sample kits of EAP for educational demonstration purposes. The costs of the kits are still quite high for widespread use ($200- $2,000). Furthermore, many companies protect their EAP fabrication processes. As a result, it is difficult to find explicit processing procedures in the literature as most companies do not disclose the actual methods. However, one fabrication process for an ionic EAP was found on a website by Dr. Keisuke Oguro, one of the pioneers of IPMC, and a leading EAP scientist [18]. Given the limited commercial availability of EAPs and lack of detailed methodologies for

fabricating EAPs, the process described by Oguro [18], involving electroless plating of platinum onto a polymer substrate, was thus selected for this thesis work. An IPMC meets our actuation material requirements of low supply voltage, scalability, and large displacements.

2.5 Electroless Plating Background

The electroless plating process (often referred to as chemical or auto-catalytic plating) is similar to electroplating processes [14,27]. However, the primary difference is the lack of an applied voltage which induces the chemical reactions of electroplating. Electroless plating relies on the addition of a reducing agent to chemically initiate the plating. Electroless plating is particularly useful in plating non-metal substrates [14]. For example, shown below are before and after photographs of polyester fabric and polyimide film plated with gold [17].

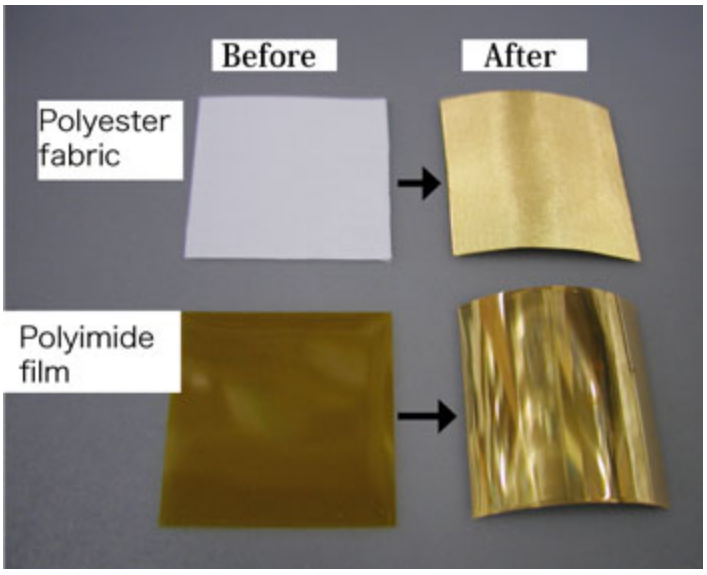

Figure 17. Gold electroless plating of non-metals [17].

Electroless plating is a non-galvanic plating method that involves multiple simultaneous chemical reactions occurring in an aqueous solution. The chemical reactions allow the plating process to occur without the addition of a supplied voltage, thus making it ideal for use with non-conducting substrates. There are many types of metals used in electroless plating. Gold, silver, rhodium, chrome, zinc, tin, and nickel are all common in industrial applications. These plating processes provide enhanced material properties for given applications. Corrosion resistance is one common use of this plating process along with interconnect applications in micro-fabrication of electronic devices [14].

Electroless plating of platinum group metals are less common in industrial applications. However, some research has been done in this area. Reducing agents that have been used for such reactions include hypophosphate, amine borane, and formaldehyde. A hydrazine bath was created in 1958 for the use with a palladium electroless plating method. With hydrazine as the reducing agent, palladium was used in the form of tetraamine chloride, $Pd(NH_3)_4Cl_2$. The solution was prepared by dissolving palladium diammine chloride, $Pd(NH_3)_2Cl_2$ in dilute ammonia [14]. The resulting reaction believed to have occurred is

$$2Pd(NH_3)_4^{2+} + N_2H_4 + 4OH^- \rightarrow 2Pd + NH_3 + N_2 + 4H_2O \quad [1]$$

The rate of the plating process increased linearly between 40^oC and 80^oC. An EDTA salt was added as a stabilizer, for without it, the bath decomposes at temperatures above 70^oC. If the bath is held stationary at a given temperature, the plating rate decreases quickly with respect to time. This is due to the catalytic decomposition of hydrazine by the palladium [14].

Electroless plating involving platinum deposition is often associated with a hydrazine bath. An example is a solution of $Na_2Pt(OH)_6$ prepared by boiling chloroplatinic acid solution with an excess of NaOH. Then, the hydrazine is added prior to the plating initiation, with the concentration of hydrazine being maintained by continuous or intermittent additions during the plating cycle. Hydrazine is also used in platings of Fe, Mo, Ni, Ag, and Ti [14].

2.6 Fabrication Process of IPMC by Dr. Oguro

The following is a procedure to prepare an ion-exchange polymer metal composite membrane (IPMC). This process was obtained from Dr. Keisuke Oguro, one of the pioneers of IPMC, and a leading EAP scientist [3]. It makes use of a platinum electroless deposition along with a hydrazine bath similar to the one discussed by Mallory [14].

2.6.1 Materials

- Base polymer: Nafion 117 by Dupont
- Aqueous solution of platinum ammine complex ($[Pt(NH_3)_4]Cl_2$ or $[Pt(NH_3)_6]Cl_4$) [Can be purchased from: Aldrich Chemical Co., Milwaukee, WI phone 800-558-9160, Catalog #275905]
- Sodium borohydride ($NaBH_4$, reducing agent for primary reduction)
- Hydrazine hydrate (NH_2NH_2- ~$1.5H_2O$, reducing agent for secondary reduction)

- Hydroxylamine hydrochloride (NH_2OH-HCl, reducing agent for secondary reduction)
- Dilute ammonium hydroxide solution (NH_4OH 5% solution)
- Dilute hydrochloric acid (HCl aq, 2 *N* solution and 0.1 *N* solution)
- Deionized water

2.6.1.1 Nafion 117

Dupont was the first to manufacture perfluorinated membranes back in the early 1960's under the registered trade name of Nafion. Designed for ion-exchange processes, Nafion is a copolymer of tetrafluoroethylene and perfluorinated vinyl ethers which contain terminal groups consisting of sulfonyl fluoride groups. These terminal groups are then processed to become proton conducting $–SO_3H$ or $–CO_2H$ groups [30]. These sulfonic acid groups in the terminal group produce highly acidic environments. In turn, noble metals (most often platinum) are often the electrocatalyst used with these membranes [30]. More detailed information on Nafion membranes and their working principles are readily available.

2.6.2 Step 1: Membrane Preparation

a) Mild Sandblast- The sandblasting increases the surface area of the membrane. Fine glass beads (GP 105A, Toshiba Co. Ltd.) should be blown onto the dry membrane using compressed air. The speed should be approximately 1 (sec/cm^2) of the membrane area. A secondary method is to use emory paper for the same result.

b) Ultrasonic Washing- This removes any residues from the sandblasting or sanding left behind from the previous step. An ultrasonic bath produces the best results.

c) HCl Treatent- The membrane is boiled in dilute hydrochloric acid (HCl aq, 2 *N* solution) for 30 minutes to remove impurities and ions in the membrane followed by a rinse of deionized water.

d) Water Treatment- The membrane is then boiled in a bath of deionized water for a duration of 30 minutes. This removes the acid and the membrane swells. The membrane should then be stored in deionized water.

2.6.2.1 Surface Roughening Effects

When attempting to chemically deposit metal onto a Nafion membrane, it has been shown that by increasing the surface area leads to better results during the plating process [30]. The increase in surface roughness provides many more nucleation sites for the metal. Also, it has been shown that the increase in nucleation sites decreases the particle size of the metal being deposited [30]. Table 6 summarizes the effect of surface roughness on platinum depostion [30].

Table 6. Effects of surface roughness on Pt deposition [30]. The higher roughness factor leads to a much higher density of Pt per cm^2.

$[H_2PtCl_6]$/mol*dm^{-3}	**Pt Loading (mg Pt /cm^2)**	**Roughness Factor R_f/cm^2 Pt cm^{-2}**	**Specific Surface Area (m^2/g Pt)**
0.02	3.8 [3.9]	278 [997]	7.3 [25.6]
0.04	6.7 [7.1]	895 [2014]	13.4 [28.4]

*Values in brackets are the values after surface roughening with 1200 grit wet carbide paper.

2.6.3 Step 2: Ion-exchange

Prepare the platinum complex of ($[Pt(NH_3)_4]Cl_2$ or $[Pt(NH_3)_6]Cl_4$) solution of 2 mg Pt/ml. Either complex yields good electrodes, however the amount of the platinum complex adsorbed depends upon the charge of the complex used.

a) Immerse the roughed membrane in the solution chosen, making sure the solution contains greater than 3 mg of platinum per cm^2 of the membrane area. (Example- >45 ml of Pt solution is necessary for a membrane area of 30 cm^2.) It is advantageous to use an excess of solution.

b) Add 1 ml of ammonium hydroxide solution (5%) to the Pt solution to neutralize, after immersing the membrane. Leave the membrane in this room temperature solution for more than 3hrs (or overnight).

2.6.4 Step 3: Primary Plating

a) Prepare a 5 wt% aqueous solution of sodium borohydride.

b) Place the membrane of 30 cm^2 in 180 ml of stirring water in a water bath at 40^oC after rinsing with water.

c) Add 2 ml of the 5 wt% $NaBH_4$ every 30 minutes for 7 times. The amount of reagent needs to be proportional to the surface area of the membrane. While in this process, the temperature should be raised gradually up to 60^oC.

d) Next, add 20 ml of the reducing agent and stir for 1.5 hr at 60^{o}C. The Pt particles are deposited only on the surface of the membrane appearing as a black layer.

e) Rinse the membrane with water, then immerse it in 0.1 N hydrochloric acid for 1 hour.

2.6.4.1 Solution Agitation Effects

Another important processing condition is the effect of solution agitation. During the chemical deposition, the flow of the electrolyte is required to aid in removing the hydrogen gas bubbles which form on the surface on the membrane [30]. The hydrogen bubbles formed during the reaction will inhibit the deposition of Pt particles on the surface of the membrane if they are not removed through a means of agitation. The agitation can be in the form of manual shaking, magnetic stirrer, mechanical shaker, or flow-through cell [30]. The following table compares the effectiveness of these methods [30]. Furthermore, agitation reduces effects of electrostatic repulsion of BH^{4-} and $PtCl_6^{2-}$ by the sulfonic acid groups, thus aiding the ionic migration [30].

Table 7. Effect of solution agitation on Pt deposition [30].

Type of Agitation	Pt Loading (mg Pt/cm^2)	Roughness Factor R_f/cm^2 Pt cm^{-2}	Specific Surface Area (m^2/g Pt)
Manual Shaking	3.9	278	7.1
Magnetic Stirrer	4.1	686	16.7
Mechanical Shaking	5.5	568	10.3
Flow-through Cell	3.8	640	16.8

2.6.5 Step 4: Secondary Plating

The amount of Pt deposited by the first plating (reduction process) is less than 0.9 mg/cm^2. The deposit amount depends on several factors such as the ion exchange capacity, thickness of the membrane, and the Pt complex structure used. Additional Pt is plated by the developing process on the deposited Pt layer. When adding 2 mg/cm^2 of Pt on the area of the 60 cm^2 (both sides of the membrane being 30 cm^2), a Pt complex solution of 120 mg of Pt.

a) Prepare a 240 ml aqueous solution of the complex ($[Pt(NH_3)_4]Cl_2$ or $[Pt(NH_3)_6]Cl_4$) containing 120 mg of Pt. Also add 5 ml of the 5% ammonium

hydroxide solution. The plating amount is dependent on the content of Pt in the solution.

b) Prepare 5% aqueous solution of hydroxylamine hydrochloride (NH_2OH-HCl) and 20% solution of hydrazine (NH_2NH_2).

c) Place the membrane in the stirring Pt solution at 40^oC. Add 6 ml of the hydroxylamine hydrochloride solution and also 3 ml of the hydrazine solution every 30 minutes for 4 hours while gradually raising the temperature to 60^oC. Gray metallic layers will form. At the end of this process, sample a small amount of the solution, and boil it with the strong reducing agent ($NaBH_4$) to check the end point. **[CAUTION: It is dangerous to add $NaBH_4$ powder to a hot solution due to the potential of a gas explosion. Instead, add $NaBH_4$ solution to a cold solution, then warm the solution using a water bath.]**

d) If any Pt ion remains in the plating solution, the solution will turn black. In such a circumstance, continue to develop Pt with the addition of NH_2OH-HCl and NH_2NH_2 solutions. If there is no residual Pt ions in the plating solution, rinse the membrane with water, and boil in dilute (0.1 N) HCl to remove any ammonium cation in the membrane. After rinsing with water, H^+ in the composite membrane can be exchanged for any cation by immersing in a solution of the chloride salt of the cation.

2.7 Testing Methods of IPMC

Testing different parameters of the IPMC helps in quantifying and evaluating the important actuation properties of the material. The following are testing methods described by other researchers who have investigated IPMC [6]. Similar tests were completed in this research after the selected fabrication process was complete to evaluate our IPMC samples.

2.7.1 Deflection Testing

A simple test, the deflection test is designed to measure the displacement of the biased actuator from the "0" voltage position. From this test, the results can be used to determine the length of the actuator needed to produce the desired degree of movement [6]. This test is accomplished by forcing one section of the EAP to remain stationary and applying the bias voltage. This in turn, allows a measureable deflection from the "0" voltage or relaxed state. The point chosen to remain stationary should affect the measured deflection. Figure 18 shows two setups with different stationary points.

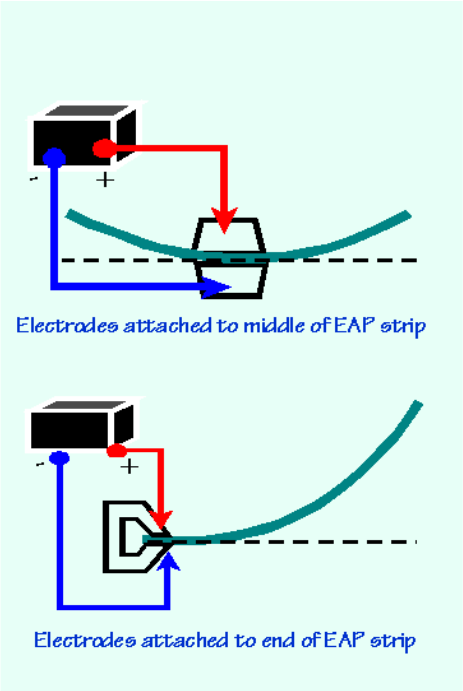

Figure 18. Deflection Testing [6].

2.7.2 Force Testing

Force testing is a key parameter in characterizing the EAP actuator. From this data, design quantities such as thickness and length of the actuator can be determined to meet design requirements. The force testing is accomplished by placing increasing masses on the actuator to measure the force output. The mass can be placed at varying distances from the electrodes. These results will yield valuable data necessary for determining the thickness and length, along with configuration of the actuator [6]. Figure 19 shows this test used by Cohen [6].

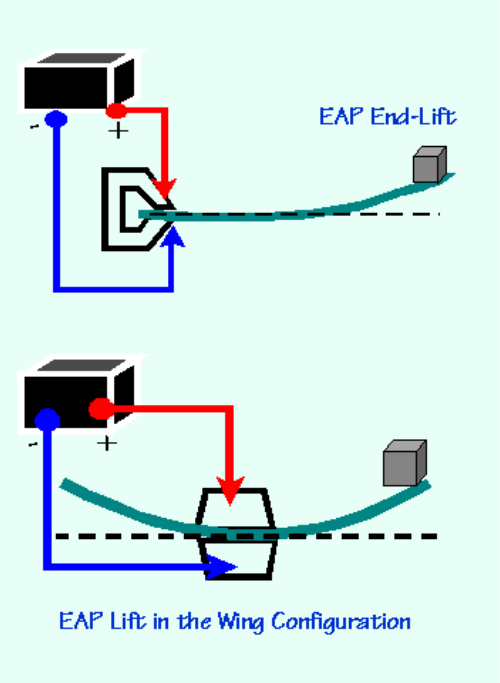

Figure 19. Force Testing [6].

3. EXPERIMENTAL PROCEDURES

The following high level experiments were performed to confirm the actuation properties of EAPs. First, the fabrication process of EAPs was investigated, and ultimately attempted. Then, high level testing was done to provide data on the voltage requirements, displacements, and force outputs. Also, the experiments will help provide insight for future designs of the actuation mechanisms for a biomimetic rolling robot.

It was decided to purchase an educational IPMC kit from Environmental Robots, Inc (ERI). The ERI kit consisted of a circuit board, gold plated electrodes on a clothespin, and two IPMC samples. Although the exact fabrication method of the ERI samples were not able to be disclosed, the samples are most likely a Pt deposited membrane based on their characteristics and appearance. Inclusion of commercially produced IPMCs was done as a benchmark comparison of IPMC behavior and helped troubleshoot technical issues encountered during initial testing of the lab fabricated IPMC.

3.1 Fabrication

Using the processing procedure from Dr. Keisuke Oguro [18], a Nafion 117 membrane on which platinum was deposited to form two electrodes was used to form an ionic polymer metal composite. This process was completed twice on two membrane samples in order to help eliminate process variations.

Step one began with roughening the surfaces of the Nafion 117 membranes. Since no sandblasting equipment was available, the substitute of emory paper was made as suggested by Dr. Oguro. The transparent membranes were sanded with 200 grit sand paper on both sides until they visibly yielded an even opaqueness over the entire membrane surface.

Figure 20. Photographs of the Nafion 117 membrane prior to surface roughening (left) and after surface roughening (right).

Next, the roughened membranes were placed in an ultrasonic bath set at medium agitation for 15 minutes. This step ensured the loose particles from the surface roughening were removed from the membranes. Following the ultrasonic bath, the membrane was boiled in a 2 N HCl solution for 30 minutes to remove impurities and ions from the membranes. Lastly, after a quick deionized water rinse, the membranes were boiled again for 30 minutes, but in deionzed water this time to remove any remaining chloride ions.

As the membranes boiled in deionized water, Step two preparations were made. The platinum complex was prepared as described in Step 2 of the fabrication process, ensuring the solution contained greater than 3 mg Pt/ml. Also in preparation, a solution of 5% ammonium hydroxide was made. After the membranes were allowed to boil in deionized water, the membranes were added to the platinum complex, along with the addition of 1 ml of the ammonium hydroxide solution which helped neutralize the platinum complex. At this point, a very slight yellowish tint was visible around the edges of the membranes (Figure 21). The

membranes were allowed to soak overnight in this solution during which there was no visible change in the appearance of the membrane.

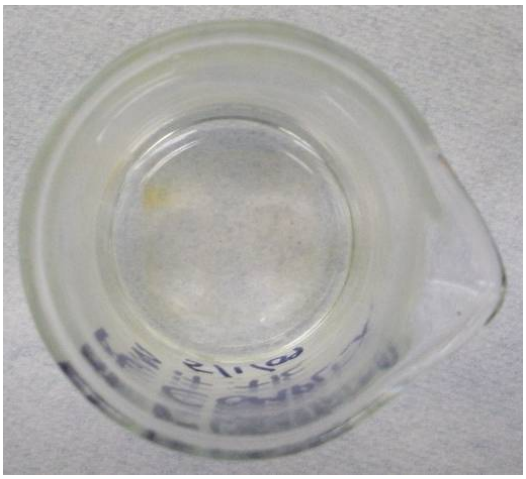

Figure 21. Membrane appears mostly transparent, but with slight yellow tint around the edges after the overnight soak.

The third step of the processing procedure was the primary plating of the membranes. Approximately 40 ml of 5 wt % aqueous solution was made of sodium borohydride. Next, the membranes were rinsed with deionized water and placed in 180 ml of stirring water at 40^{o}C initially by using a hotplate with magnetic stirrer. With this setup, shown in Figure 22, 2 ml of the sodium borohydride reducing agent was added every 30 minutes for seven times. Step 3 begins depositing the Pt onto the surface of the membrane. It is important that the reducing agent is added at the specified intervals provided in the fabrication process above. The intervals help maintain the concentration of reducing agent necessary for the reduction to occur. During this process on the first membrane, the membrane became briefly trapped underneath the stirrer resulting in a dark region on the membrane, shown in Figure 23, where contact was made.

Figure 22. Photograph of plating process setup.

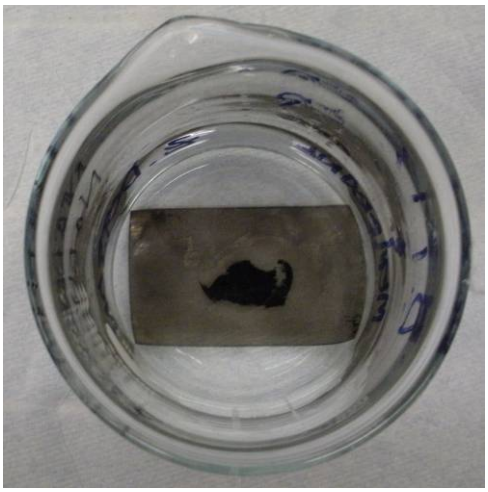

Figure 23. Photograph dark plating region where membrane was trapped underneath the magnetic stirrer.

The temperature was gradually and linearly increased with respect to time throughout this addition process to 60^{o}C. As the reducing agent was added each time, it was observed that hydrogen bubbles were rapidly forming on the membrane surface (Figure 24) and escaping with the agitation of the stirring solution.

Figure 24. Close-up photograph of the hydrogen formation during reduction process.

The hydrogen formation gradually faded toward the end of the 30 minute intervals. The fading of the hydrogen formation demonstrated the importance of the regular interval of the additions of reducing agent. Also, fine black deposits began forming from the addition of the first 2 ml of reducing agent. At the end of the 7 additions, 20 ml of the 5 wt % sodium borohydride was added to the solution with the membrane, and was kept stirring and held at 60^{o}C for another 1.5 hours. The addition of the 20 ml of reducing agent caused even more deposition of Pt particles onto the membrane surface. Lastly the membrane was boiled in 0.1 *N* HCl for 1 hour and then stored in deionized water until last step could be completed the following day. Figure 25 shows photographs of both membrane samples after completion of the primary plating.

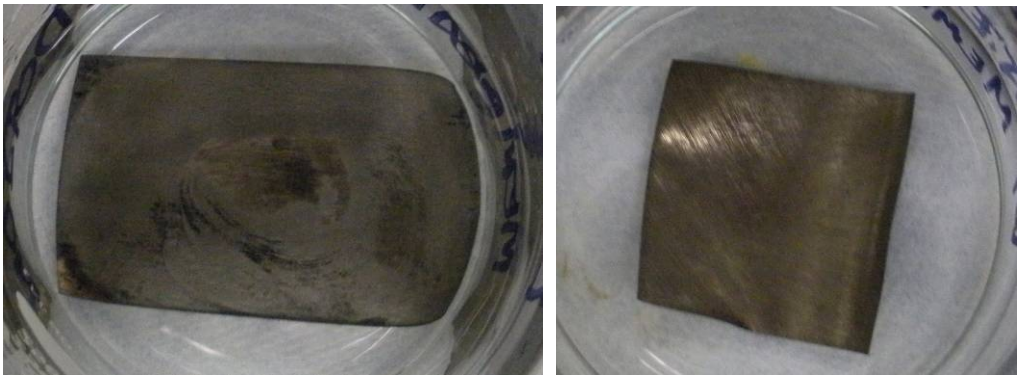

Figure 25. Photographs of the first sample (left) and second sample (right). The second sample is a more uniform deposit even though there was no change in processing conditions.

According to Dr. Oguro, the primary plating (step three), deposits less than 0.9 mg/cm^2 onto the membrane. Additional Pt was deposited during the secondary plating of step four. Here, a 240 ml aqueous solution of the Pt complex was made by adding 120 mg Pt to deionized water. This aqueous solution of the Pt complex was heated while stirring to 40^{o}C again. While the Pt bath was heating, aqueous solutions of 5% hydroxlylamine hydrochloride (about 40 ml needed) and 20% hydrazine hydrate (about 20 ml needed) were made. Once the Pt solution reached 40^{o}C, the membrane was added to the solution and 6 ml of hydroxylamine hydrochloride and 3 ml of hydrazine hydrate were added every 30 minutes for four hours. Again, the solution was gradually and linearly with respect to time increased to 60^{o}C throughout the four hours. During this secondary plating, the black deposits of Pt on the surface of the membrane became more defined and uniform compared to the result of the first plating of step three. At the end of the four hours, a 5 ml sample of the solution was boiled with the strong reducing agent, sodium borohydride, to verify the endpoint. The 5 ml sample was allowed to cool prior to adding the sodium borohydride as indicated by the safety note in the process procedures. Since the boiling

sample did not turn black, which would signify remaining Pt ions, it was determined that the endpoint was reached, and the plated polymer sample was removed. Next, the now black Pt coated membrane was rinsed with deionized water and boiled in dilute 0.1 *N* HCl thus removing any remaining ammonium cation. At this point, hydrogen protons in the now metal composite membrane can be exchanged for other cations by immersing in a solution of the chloride salt of the cation. The photographs below in Figure 26 depict the final membranes after the secondary plating. Visibly, there was not much difference in the appearance between completion of step 3 and 4. With the chemical plating process complete, the membrane must now be stored in deionzed water.

Figure 26. Photograph of the completed plated membranes. Shown on the left is the first sample, and on the right is the second sample.

3.2 Verification of Fabricated IPMC

During the plating process, platinum was deposited on all surfaces of the membrane. Very little resistance would be expected between the top and bottom surfaces of the membrane because the surfaces are not isolated. In other words, the top and bottom are still connected via the very thin edges of the membrane which have been deposited with Pt as well. To verify this, a multi-meter was used to check the resistance of the membrane.

For the IPMC to function as an actuator, the two sides of the sample must be electrically isolated. In order to isolate the two surfaces of the plated membrane, all edges must be trimmed. All four edges were trimmed as shown in the following figure. It was possible to visibly check which edges were trimmed as compared to the untrimmed edges that were deposited with Pt. The untrimmed edges appeared just as the top and bottom surfaces of the plated membrane. The edges, once trimmed, appeared black (Figure 27). The black, trimmed edges provided a visual verification that the top and bottom of the membrane was electrically isolated. All samples were trimmed to 18mm in length and 5mm wide for uniformity during testing. The fabricated membrane thickness was 0.19mm.

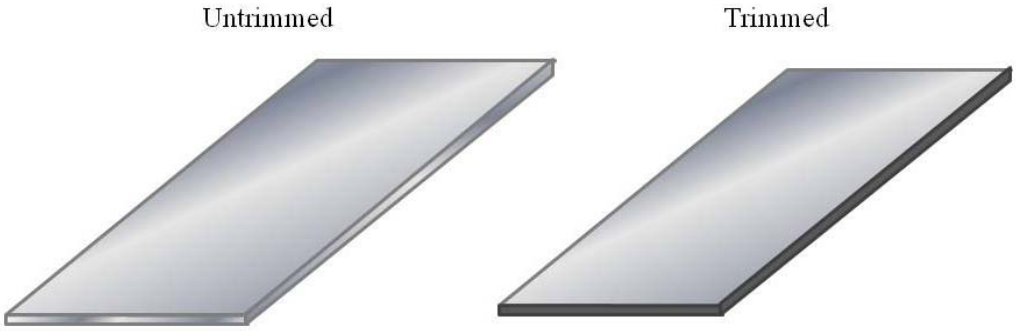

Figure 27. Untrimmed and trimmed membrane edges.

While awaiting the arrival of the ERI kit, it was decided to fabricate a similar test setup to begin testing of the lab fabricated samples. First, a clamping device had to be fabricated in order to hold the IPMC sample and allow electrical contact to both sides of the membrane. Similar to the clothespin and gold electrodes provided with the ERI kit, copper electrodes were epoxied to a wooden clothespin as shown in Figure 28.

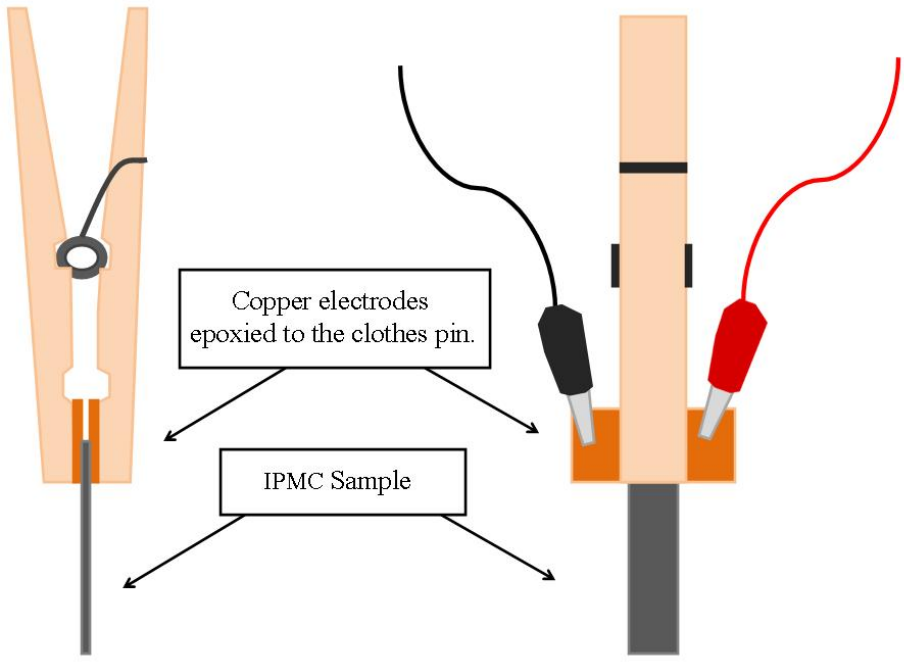

Figure 28. Fabricated clothespin with copper electrodes.

Next, to check the functionality of the IPMC sample, a test setup consisting of a variable power supply, the fabricated clothespin with copper electrodes, a beaker of water, and the sample as shown below in Figure 29.

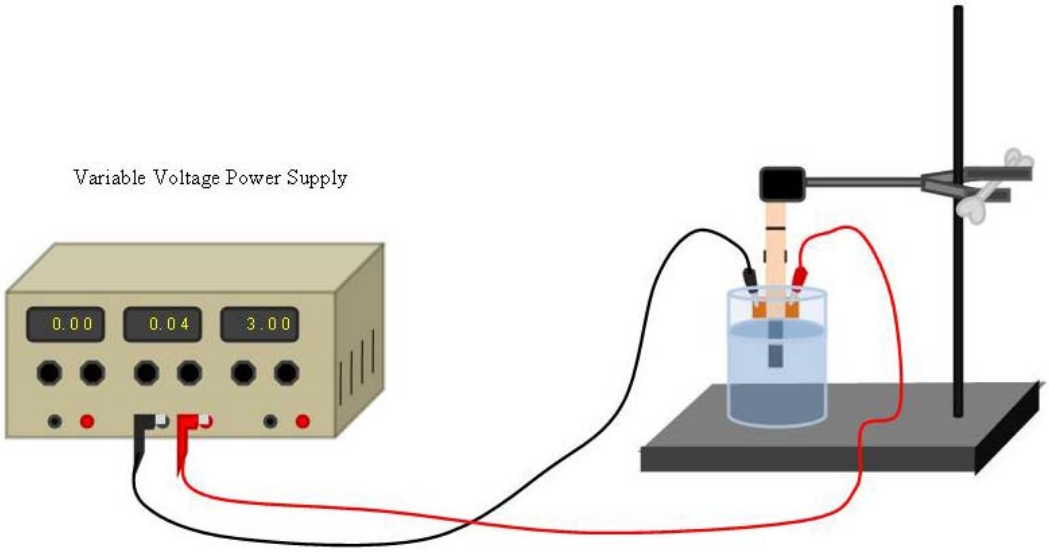

Figure 29. Experimental test setup.

This setup was used with and without a beaker of water which immersed the IPMC sample halfway in the water. Both versions were tried to see if there were any differences in the actuation of the IPMC sample. However, no deflection occurred in either case and the current was limited. The voltage was applied for short periods of time while attempting to not current limit with the test setup. The only observation was of a "sizzling" noise produced by the sample during the application of the voltage. After closer inspection, it was observed that the "sizzling" noise was the production of bubbles at the copper-platinum interface. The sample was removed from the clothespin, and the initially shiny copper electrodes were covered in black and green discolorations indicating the presence of a corrosion reaction.

There are many types of corrosion involving metals. However, the most likely cause of this rapid corrosion was due to galvanic corrosion. Galvanic corrosion is corrosion between two dissimilar metals that are placed in a conducting solution (electrolyte) and placed in contact with

each other [34]. This type of corrosion is electrochemical in nature and is based on the difference of the electrode potentials of the metals involved. The electrolyte provides the ion transport of the ions from the more active metal (anodic metal) to the more noble metal (cathodic metal). As this occurs, the anodic metal will get oxidized (corrode) and the cathodic metal will get reduced. A large difference between the potentials of the metals results in greater corrosion of the anode [34].

The corrosion appeared to be at the platinum coated membrane and copper electrode interface. Table 8 shows the emf series of various metals from most noble to active [34]. The emf series is a list of metals organized by their standard potentials. Also, the corrosion will occur with the more active metal. As seen in Table 8, copper is much more active than Pt. This is consistent with our observations of the discoloration of the copper electrodes. Also, one of the factors governing galvanic corrosion is the resistance of the metals involved. Higher resistance metals will corrode slower than low electrical resistance metals. This also explains why the corrosion occurred in such a short period of time of only five minutes. Table 8 indicates that gold electrodes are much more compatible for use with Pt than copper, thus the electrodes were switched to gold electrodes.

Table 8. Electrode potentials of various metals [34].

Electrode Reaction	Standard Potential $\phi°$(in volts) at 25°C
$Au^{3+} + 3e^- = Au$	1.50
$Pt^{2+} + 2e^- = Pt$	ca. 1.2
$Pd^{2+} + 2e^- = Pd$	0.987
$Hg^{2+} + 2e^- = Hg$	0.854
$Ag^{+} + e^- = Ag$	0.800
$Hg_2^{2+} + 2e^- = 2Hg$	0.789
$Cu^{+} + e^- = Cu$	0.521
$Cu^{2+} + 2e^- = Cu$	0.337
$2H^{+} + 2e^- = H_2$	0.000
$Pb^{2+} + 2e^- = Pb$	−0.126
$Sn^{2+} + 2e^- = Sn$	−0.136
$Mo^{3+} + 3e^- = Mo$	ca. −0.2
$Ni^{2+} + 2e^- = Ni$	−0.250
$Co^{2+} + 2e^- = Co$	−0.277
$Tl^{+} + e^- = Tl$	−0.336
$In^{3+} + 3e^- = In$	−0.342
$Cd^{2+} + 2e^- = Cd$	−0.403
$Fe^{2+} + 2e^- = Fe$	−0.440
$Ga^{3+} + 3e^- = Ga$	−0.53
$Cr^{3+} + 3e^- = Cr$	−0.74
$Cr^{2+} + 2e^- = Cr$	−0.91
$Zn^{2+} + 2e^- = Zn$	−0.763
$Nb^{3+} + 3e^- = Nb$	ca. −1.1
$Mn^{2+} + 2e^- = Mn$	−1.18
$Zr^{4+} + 4e^- = Zr$	−1.53
$Ti^{2+} + 2e^- = Ti$	−1.63
$Al^{3+} + 3e^- = Al$	−1.66
$Hf^{4+} + 4e^- = Hf$	−1.70
$U^{3+} + 3e^- = U$	−1.80
$Be^{2+} + 2e^- = Be$	−1.85
$Mg^{2+} + 2e^- = Mg$	−2.37
$Na^{+} + e^- = Na$	−2.71
$Ca^{2+} + 2e^- = Ca$	−2.87
$K^{+} + e^- = K$	−2.93
$Li^{+} + e^- = Li$	−3.05

After switching to gold electrodes, the same test was repeated. Using the gold electrodes, the current was not limited, the IPMC deflected as expected as voltage was applied, and no bubbling occurred even as higher voltages (up to 6V) were imposed on the IPMC sample. The

confirmation that the fabricated samples of IPMC did work yielded confidence in the continuation of the experimental testing procedures previously outlined.

Another interesting characteristic of the IPMC samples observed was the capacitance. As applied voltages on the IPMC samples were varied during the testing, it was observed that the samples were sometimes unable to completely discharge. The samples often held a charge ranging from 0.25-1.0V even as the applied voltage was decreased to 0V. When these charged samples were immersed back into DI water to keep hydrated, the samples often curled instantly when discharging in the DI water. The curling motion upon the charge release of the samples often folded the sample in half or in a spiral configuration. The ability of the IPMC samples to hold a charge suggests that IPMCs act as parallel-plate capacitors.

3.3 Deflection Testing

The deflection test was modeled after the experiment used by Cohen [6] as previously described. Using the setup, shown in Figure 30, with 1/10 inch grid paper, the gold electrode contacts from the ERI Kit, a variable voltage supply, and a digital camera, deflection testing was done on both the lab fabricated IPMC sample and also the samples provided in the ERI kit. The deflection test was recorded digitally with a Nikon Coolpix (10.0 megapixel) camera and measurements were made offline as the video was replayed. The video was played in Windows Media Player under “Slow” play speed. The deflection (d) was measured as the distance the tip of the sample deflected horizontally from the starting position as shown in Figure 31. Starting at 0V, the voltage was increased in 0.5V increments up to 6V.

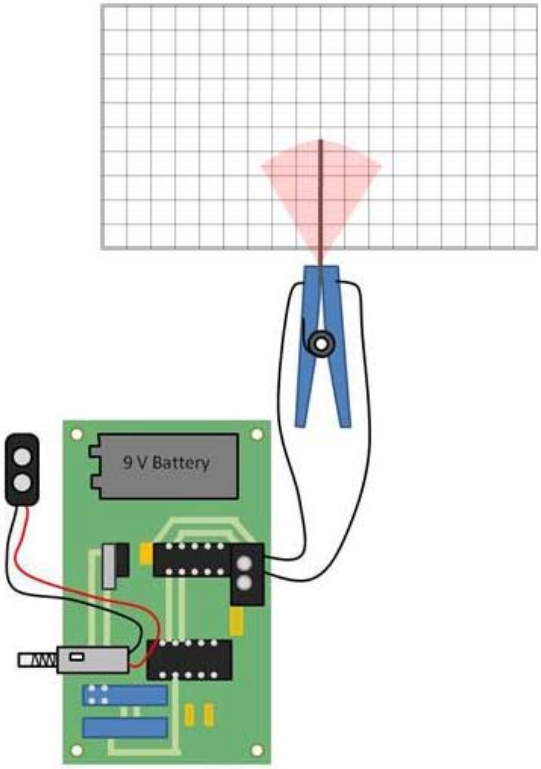

Figure 30. Deflection test setup.

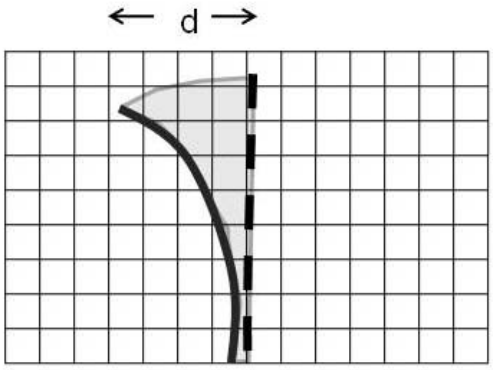

Figure 31. Deflection Measurement.

3.4 Force Testing

Since the IPMC membrane fabricated is only 0.007 inches thick, the expected force output is extremely small. With an experimental setup such as the one used by Cohen, et al in Figure 19, there would be difficulty in adding the small weights required by the small force output. Instead, it was decided to place the IPMC actuator over an analytical balance and allowing the IPMC to exert a force onto the balance. The accuracy of the balance permits an accuracy of 0.0001 of a gram. The setup is shown below in Figure 32. An applied voltage was increased from 0-6 V in 0.5 V increments. Again, a Nikon Coolpix (10.0 megapixel) digital camera was used to record video for analyzing the data offline for more accuracy. The camera was focused on the analytical scale readout and also the voltage applied. As the video was replayed using Windows Media Player using the "Slow" setting under play speeds, the applied voltage and corresponding force output were documented.

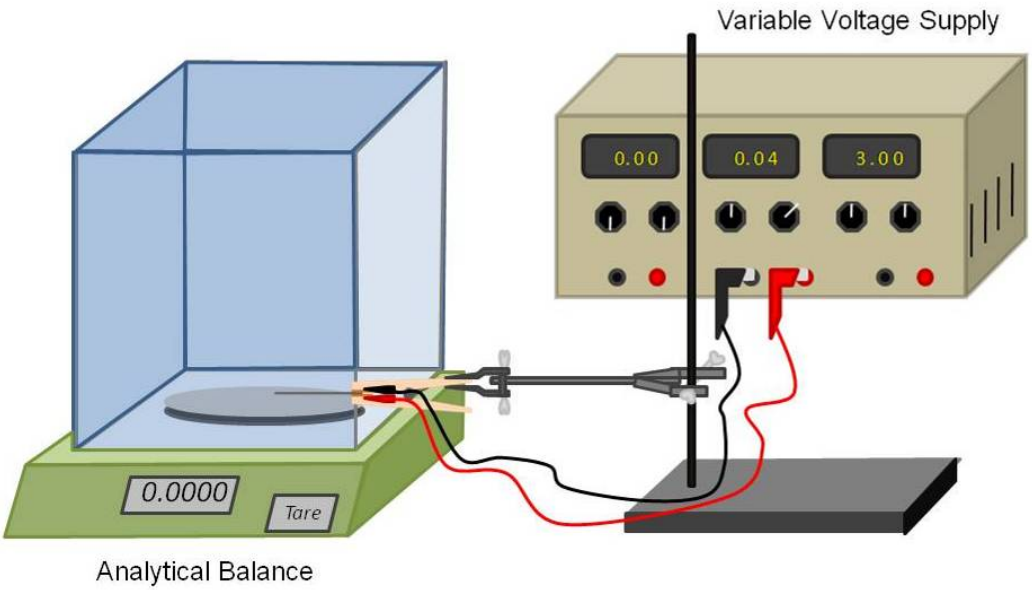

Figure 32. An analytical scale was used for measuring the force output of the IPMC actuator.

4. RESULTS AND DISCUSSION

4.1 Deflection Testing Results

The samples provided by the ERI kit were used as standards to compare to the lab fabricated IPMC samples results. The deflection testing of the ERI samples showed some variability in the maximum displacement. When a series of five tests of each ERI sample were averaged together (10 tests in total) for the case of applying a positive voltage to the ERI sample, the average maximum displacement was 12.1mm at 6V. The increases in the displacement were fairly linear with increases in the voltage shown in Figure 33.

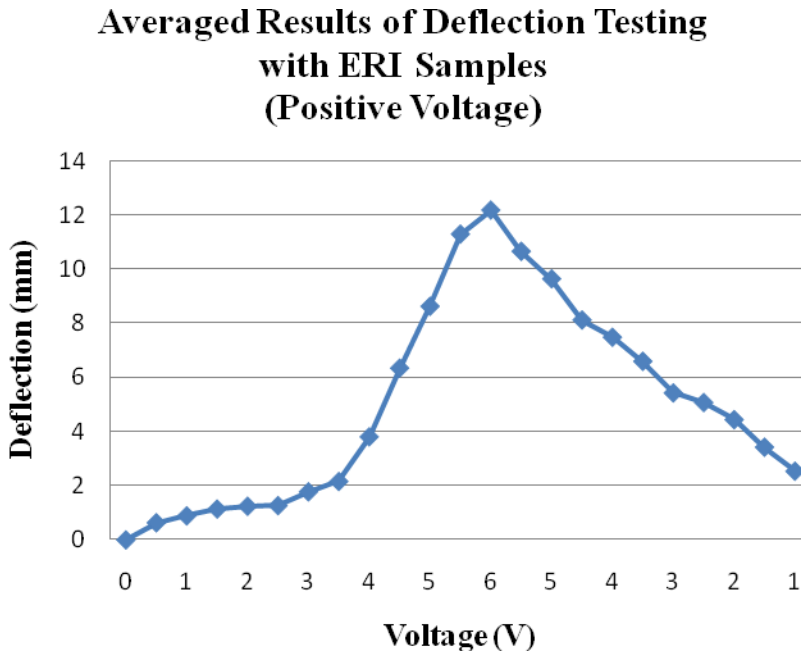

Figure 33. Positive voltage defection testing of ERI samples.

During the second testing using a negative voltage, the peak displacement was quite less than the positive voltage results. Again, the results of Figure 34 are the average of five test runs. The peak displacement with a negative voltage was only 3.55mm at -6V. This was an unexpected outcome since the positive voltage had a displacement of 12.1mm. The positive or negative bias should have no impact on the displacement characteristics of the sample. However, as shown in Figure 34, the sample only recovered about 1.5mm of the displacement as the voltage was returned to 0V. The reason for this is not known, but it is believed to be caused by the capacitance characteristics of the IPMC. Overall, the deflection test of the ERI sample with a negative voltage again showed a relatively linear trend in the displacement versus voltage as expected based on the results of Cohen [3].

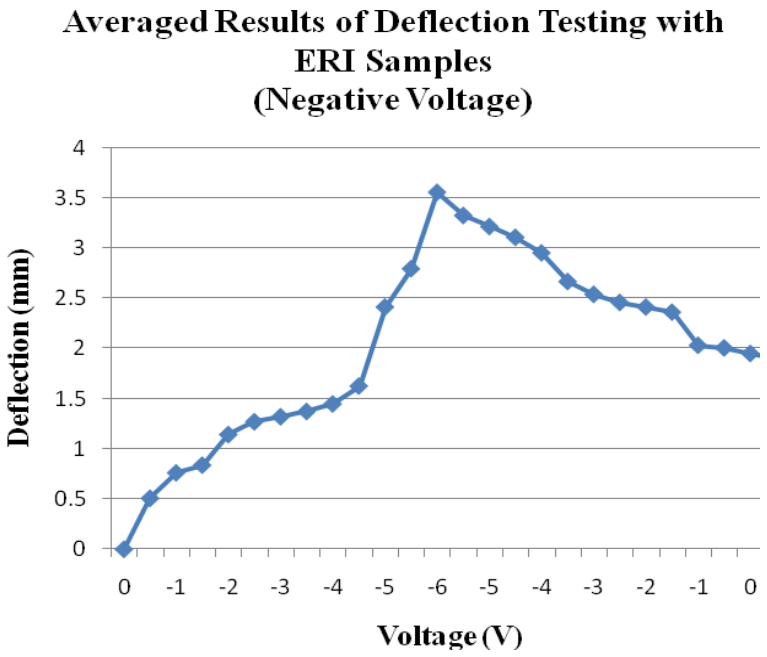

Figure 34. Negative Voltage Delfection Testing of ERI Samples.

Next, deflection testing was performed using the lab fabricated IPMC samples with the results of five runs averaged and graphed as shown in Figure 35. The second lab fabricated sample (the more uniform sample on the right in Figure 26) was tested first as it showed more deflection than the first lab fabricated samples during the verification process prior to testing. During the positive voltage test, the sample performed very similar to the ERI samples as the voltage was increased from 0-6V. The peak deflection was recorded at 7.49mm. However, as the voltage was decreased from 6-0V, the sample deflected back to the initial position at only 4.5V. As the voltage was decreased further, the sample deflected past the starting position, and ended at nearly -13mm. This characteristic did not fit with the ERI sample tests, but is most likely caused by an uneven distribution of Pt on the two surfaces of the membrane. The uneven distribution between the two sides could cause the unequal deflection. Overall, the net displacement was over 20.5mm which is double the displacement of the ERI samples.

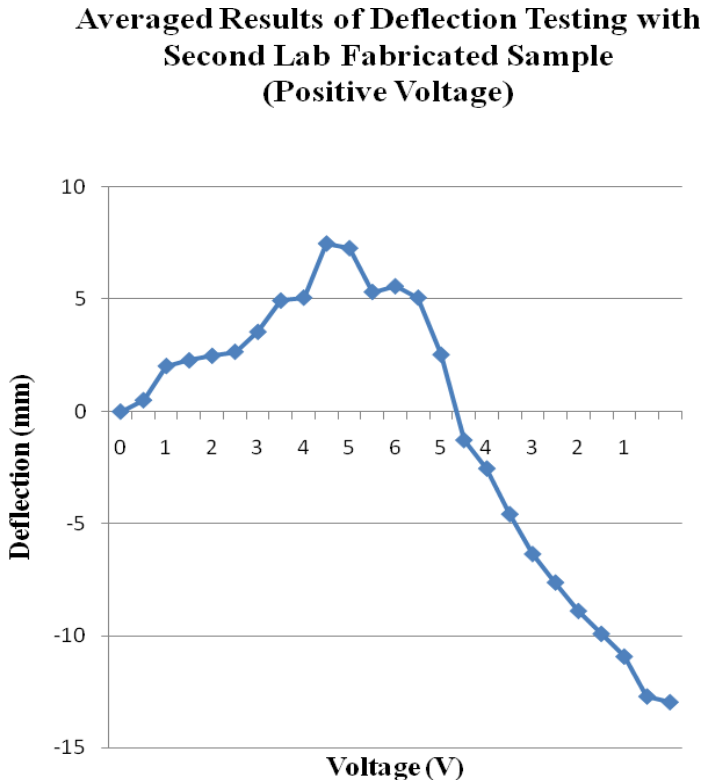

Figure 35. Positive voltage deflection test with second lab sample.

Next, the same lab fabricated sample tested with a positive voltage was tested five times with the application of a negative voltage and the results were averaged. The negative voltage again caused the deflection to occur in the opposite direction. Here, the displacement was again linear from 0V to -5V reaching an average of 8mm peak displacement , but as the voltage was gradually increased back to 0V, the sample recovered to within 2mm from the starting position (Figure 36). Again, this is most likely caused by the lack of uniformity in the deposition of Pt, or possibly due to the capacitance of the IPMC once charged. Using a multimeter, the sample held

a charge of approximately 0.25V once the supply voltage was returned to 0V. Overall, the average of the five test runs provided very uniform results that were predominately linear.

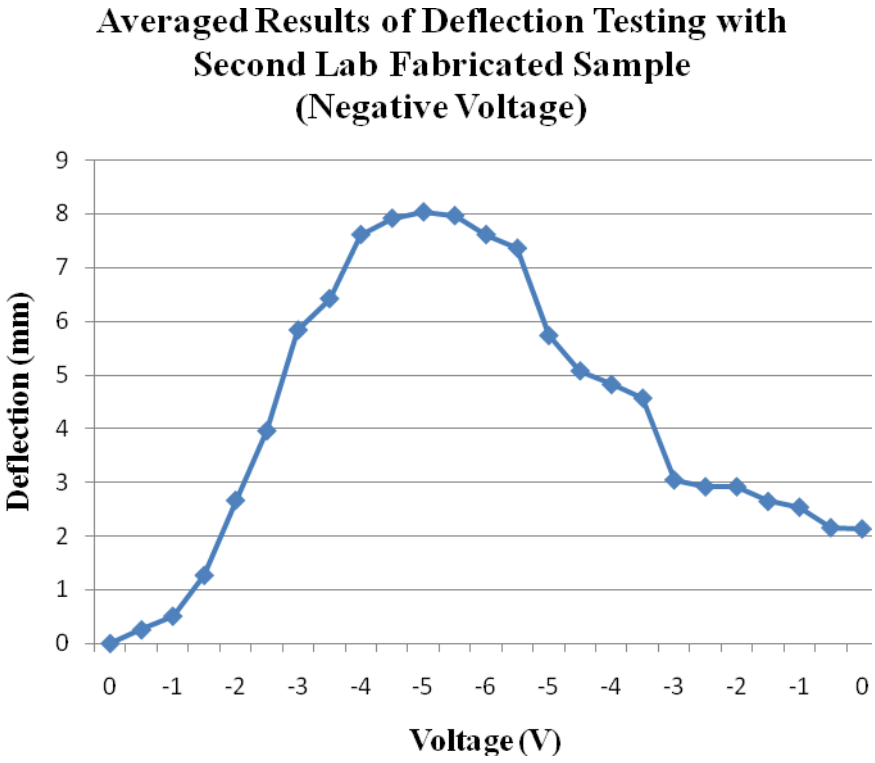

Figure 36. Negative voltage defection test with second lab fabricated sample.

Another test was done on a different piece of the lab fabricated IPMC that had a creased "bend" or "kink". This sample demonstrated different results than the previous sample. This sample, when under a positive voltage (Figure 37), deflected very little from 0-4V, but at 4V the deflection increased very rapidly. The sample deflected about 34mm from 4-5V (Figure 37). As the voltage was returned to 0V, the displacement decreased similar to that of the previous tests although still not to the original position. In this case, there was either a lack of uniformity in the

Pt deposition or the pre-stressed region of the crease in the membrane that had to be overcome prior to deflection since the direction of the deflection was opposite of the direction of the crease in the sample. The effect of the crease in the sample demonstrates the importance of sample uniformity.

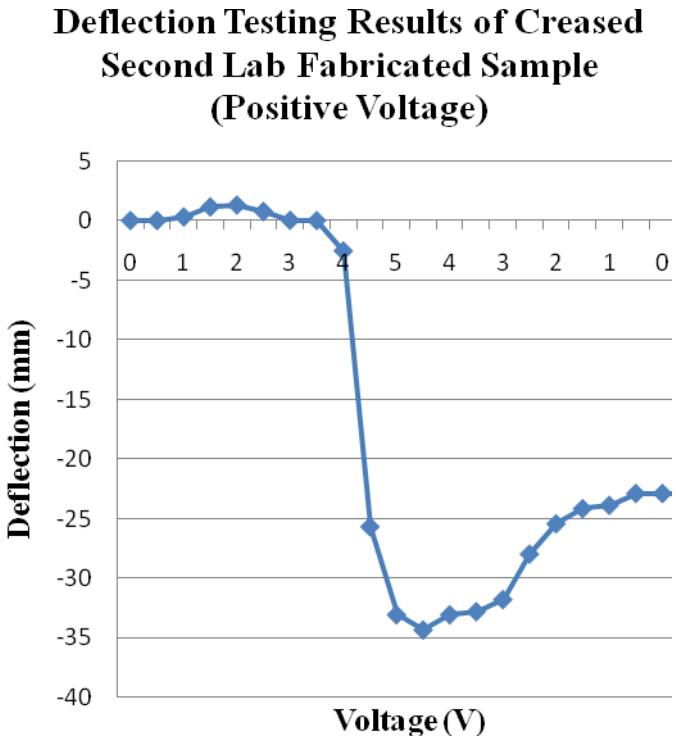

Figure 37. Deflection test with positive voltage of creased lab fabricated sample.

The same sample was then tested using a negative applied voltage to see if the same rapid response occurred due to the creased region The rapid deflection was not as defined with the negative voltage, because the deflection was in the direction of the "bend" or "crease" in the sample. Therefore, the sample did not have to overcome the force necessary to inflect the crease

prior to deflecting. There was still a faster increase in displacement from 1.5-2.5V compared to the results of tests in Figure 35 and Figure 36, but the very large deflection did not occur as in Figure 37. Instead, the negative voltage induced a deflection pattern similar to the ERI kit. A maximum displacement of 10mm occurred at about -3.5V (Figure 38).

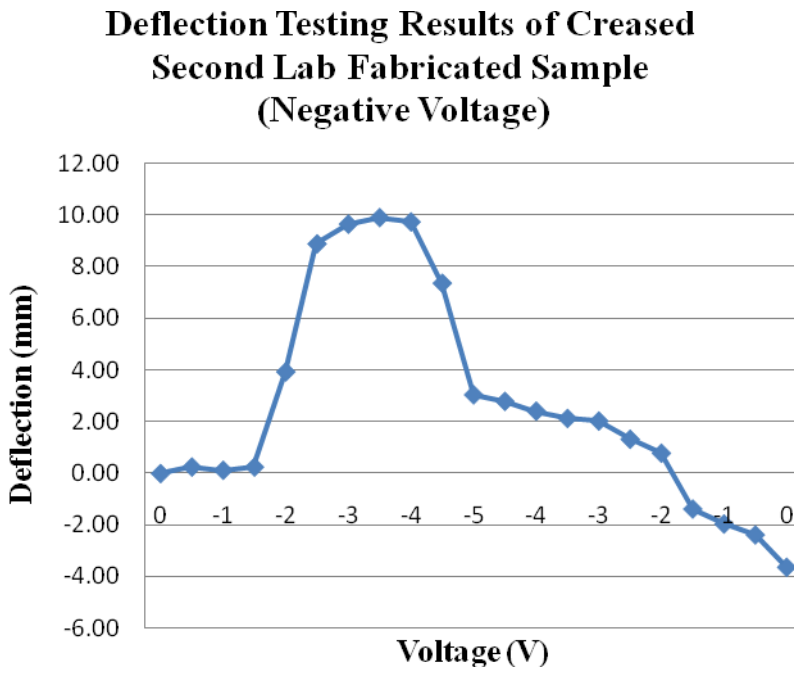

Figure 38. Deflection test with negative voltage of creased lab fabricated sample.

Finally, a sample from the first lab fabricated IPMC was tested. This sample, as shown on the left in Figure 26, was more transparent due to a lack of Pt deposition. Again, five tests were performed and averaged together. As shown in Figure 39, the interesting characteristic of this sample was the lack of a declining deflection as the voltage was returned to zero. Instead this sample showed "one-way" actuation. Even with a negative applied voltage, the sample did not deflect to the original starting point (Figure 39).

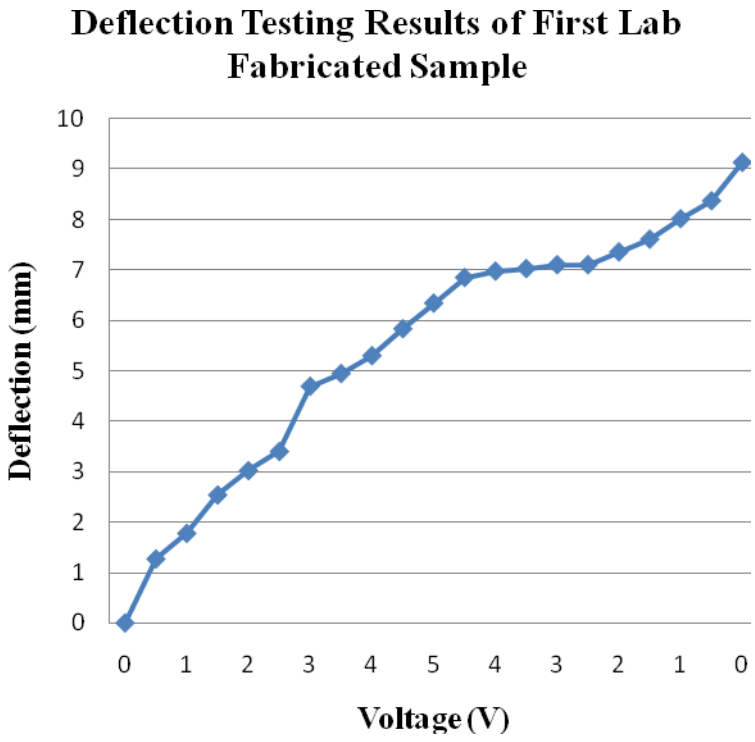

Figure 39. Positive voltage test of the first lab fabricated sample.

4.2 Force Testing Results

The ERI samples (with dimensions 20mm x 5mm x 0.3mm) were the first to be tested for the force output. The ERI results provided insight and expectations of what to expect from the lab fabricated samples. The sample was placed as close to the scale as possible without touching the scale's surface, and then the voltage was gradually increased from 0-6V and decreased from 6-0V. The test results of 5 trials were averaged together. The first of the two ERI samples, shown in Figure 40 below, provided extremely linear results. At approximately 1V, the sample first contacted the scale initiating a force readout on the scale. A peak force output of 0.555 grams was recorded at 4.5V. Also, as the voltage was decreased, the sample reached its starting position at 2.5V instead of 0V. Therefore, as the voltage continued to be decreased to 0V, the sample deflected past its starting position hence the "negative" displacement. In other words, the sample lifted off the scale at less than 2.5V resulting in a "zero" force from 2.5V down to 0V.

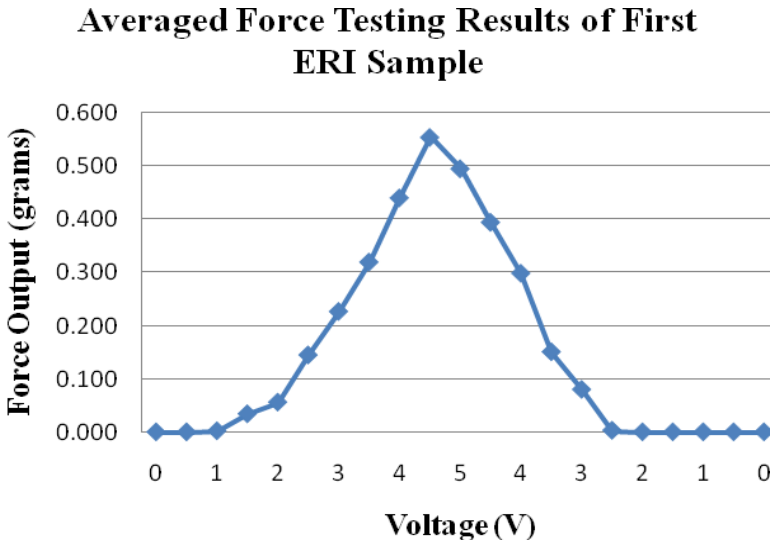

Figure 40. Force testing of first ERI sample.

Another force test was performed on the second ERI sample provided in the kit. The test was run five times with the results being averaged together in Figure 41. Again, the results were very linear, but the peak force was approximately half of the first test. This was not alarming due to the seemingly variable nature of the samples as observed thus far. However, it was expected that the ERI samples commercially produced would produce less variation. Also, the second samples deflected past the original starting position at about 1.5V as the voltage was decreased much like the force testing results of the first ERI sample above in Figure 40.

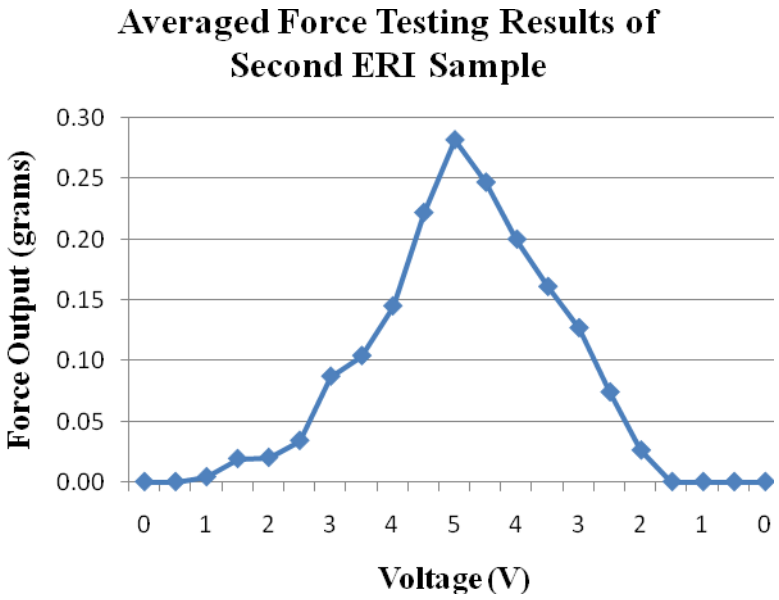

Figure 41. Force testing of second ERI sample.

With the ERI samples tested, the next step was the testing of the lab fabricated IPMC samples. The lab fabricated samples were 0.19mm in thickness while the ERI samples were 0.3mm in thickness. The prediction of the lab fabricated results was that the linearity observed from the commericially available ERI samples was not going to be present in the less uniform

lab fabricated samples. Also, the thinner lab fabricated samples should have a smaller force output since the force output is directly affected by the thickness of the actuator. Again, a series of five tests were performed with the results being averaged together. The voltage was gradually increased from 0-6V and back to zero while recording the force readout on the scale. As shown in Figure 42, it is evident that the lab fabricated sample responded fairly linearly with the voltage. The main difference in the lab fabricated samples and the ERI samples was the force output. The peak force ouput of the lab fabricated sample was 0.14 grams which is significantly less than the ERI samples. More interesting was the similarity of the deflection in returning past the orginal starting postion at 2V just as the ERI samples did. This is likely the result of the IPMC sample holding a charge due to its capacitance property, therefore changing the response as a charge is accumulated within the sample.

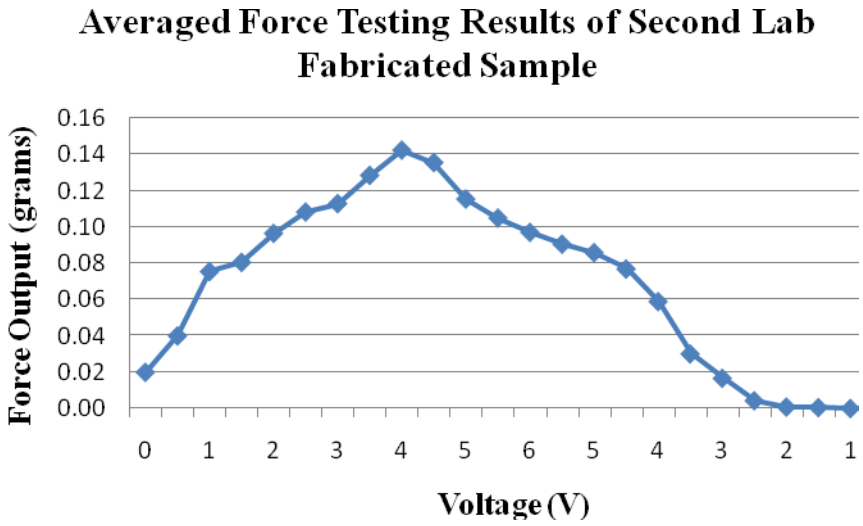

Figure 42. Force testing of second lab fabricated sample.

Again, another lab fabricated sample was tested to check uniformity. This second sample was chosen because it had a visible lack of uniformity. Certain regions of this sample were darker and lighter. This was caused by the uneven Pt deposition. As a result, the force output versus voltage was significantly different from that of the previous sample. Shown in Figure 43 as the voltage was increased and decreased, the force output sporadically, yet gradually increased. The peak force output of this sample was recorded at 2V during the reduction of the voltage. Clearly, the uniformity is a significant factor in the output characteristics of the IPMC sample.

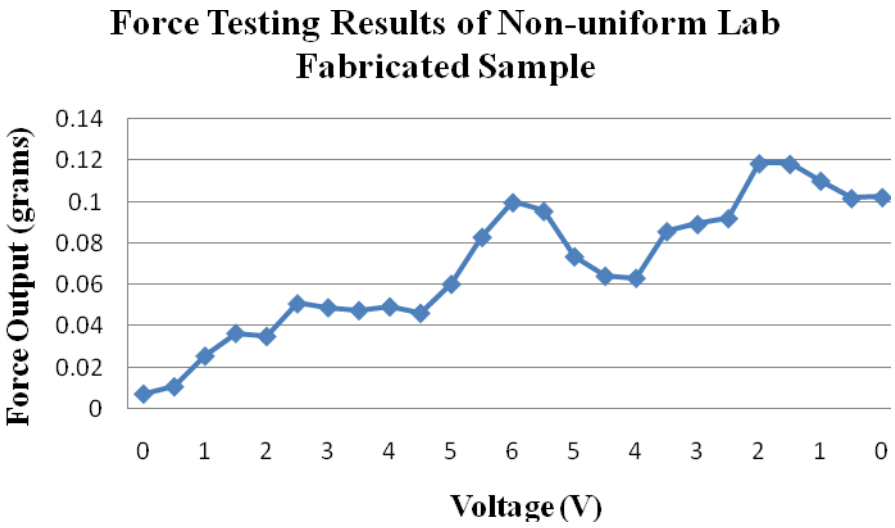

Figure 43. Force testing of first lab fabricated sample.

4.3 Discussion of Results

Evaluation of the results of the fabrication, deflection testing, and force testing allows a comparison with results in literature results along with developing conclusions for this thesis research. This discussion of the results concludes with the evaluation of IPMCs as potential actuators for implementation on a rolling robot.

The fabrication of the IPMC samples using the process provided by Dr. Oguro [18] worked well for this experiment. With limitations of commercially available EAPs, this process proved to be a good alternative to purchasing expensive educational kits. For roughly the same cost, the fabrication process can provide nearly twenty times more IPMC material than supplied with the educational ERI kit in addition to providing similar deflection and force output.

The deflection testing of the ERI samples and the lab fabricated samples correlated quite well, given the unknown materials and processing conditions of the ERI samples. The deflection distances varied linearly with the supply voltages as expected based on the results of Min Yu who achieved deflections of 5mm near the maxium tested voltage of 2.5V [36]. The deflections of this thesis research at 2.5V were 1-5mm. When comparing the maximum displacement of the ERI samples with the maximum displacement of the lab fabricated samples, both occurred near 5V (Figure 44) and achieved repeatable deflections between 5-10mm. The large displacements achieved will provide adequent design flexibility for many applications.

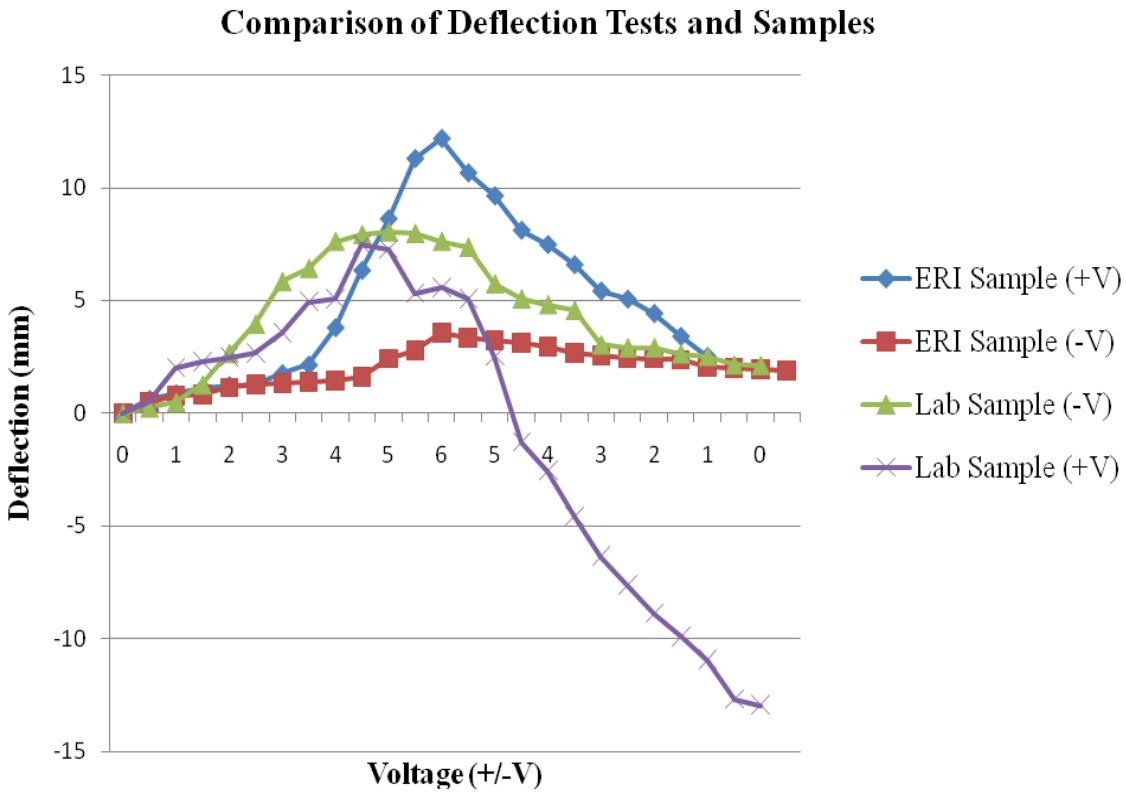

Figure 44. Comparison of Deflection Tests and Samples.

The force testing showed linear force outputs with respect to the supply voltage as well. The peak forces for both the ERI samples were between 0.28- 0.55 grams. The force outputs for the lab fabricated samples were around 0.1-0.14 grams. The small force output was expected of both the ERI samples and the lab fabricated samples [36] based on typical values provided in Table 5 [3]. In addition, the higher force outputs of the thicker ERI sample and the lower force outputs of the thinner lab fabricated samples correlated well with the theory [9]. The thicker force outputs were achieved by the large thickness of the ERI samples. Figure 45 shows a comparison of the force testing of the ERI samples and the lab fabricated samples.

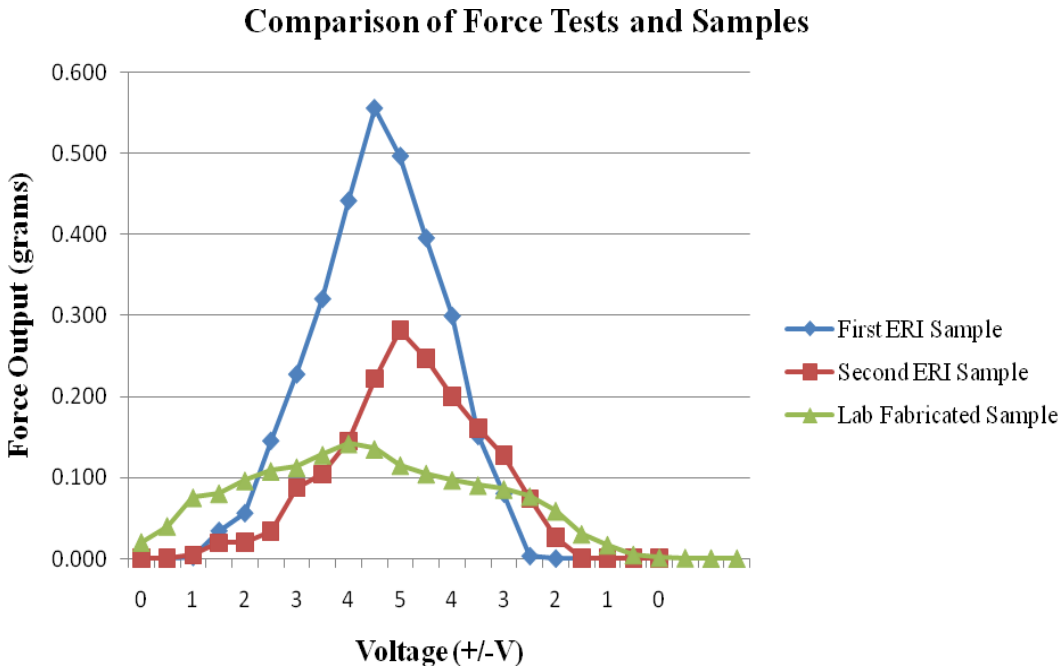

Figure 45. Comparison of Force Tests and Samples.

The tests provided the necessary results for evaluating the use of IPMC materials as a means of actuation on a small scale rolling robot. The large deflections provide many options for maximizing flexibility of the mechanical design options. If only small deflections were demonstrated, more constaints on the design of the actuation mechanism would be required to achieve the desired deflections. Also, the ability of the IPMC samples to be "tuned" to certain deflections with a predetermined voltage allow even great design flexibility. Additionally, more or less deflection can be obtained by increasing or decreasing the length of the IPMC respectively. One potential limitation is the low force output of the IPMC samples. The exact

forces required by a small scale rolling robot have not yet been determined, but the low force output of the IPMC samples must be considered during the design of the rolling robot.

5. CONCLUDING REMARKS

5.1 Summary

This materials based research of the actuation mechanism for the biomimetic rolling robot consisted of equal parts of literature research, evaluation of actuation materials, fabrication of the IPMCs, and experimental testing of the IPMCs. Beginning with extensive literature research, the wide range of actuation mechanisms was narrowed to the smart materials of shape memory alloys, piezoelectric materials, and electroactive polymers. From there, the choice was made to pursue electroactive polymers based on their physical, mechanical, and chemical properties. The material selection moved the research into fabrication and purchasing IPMCs. The fabrication process was well defined and led to relatively easy fabrication of the samples. Testing the fabricated and purchased samples provided valuable data necessary for the future design work of the rolling robot. The data from the deflection testing showed sufficient defection. Also the force testing provided results that were comparable to other similar research. The deflection and force output data will help in the mechanical design of the robot can be further investigated with the implementation of an IPMC actuation process. The mechanical design will help optimize the properties of the IPMC actuators.

A comparison of the original design criteria set forth at the beginning of the research to the results of the IPMC actuators tested is shown in Table 9. Overall, the IPMC actuators met all

of the design criteria. The low force output is the most limiting factor. However, with all other criteria satisfied with the IPMC actuators, the implementation of IPMCs on a rolling robot is very optimistic based on the preliminary results.

Table 9. Comparison of Design Criteria and IPMC Actuators.

Requirements	IPMC Actuators
Low Voltage	Low (2-6V)
Large Displacement	High (5-20mm)
Scalability	Good (0.1mm in thickness)
Manufacturability	Easy
Force Output	Low (0.1-0.5 grams)
Biomimetic Movement Preservation	Good
Biocompatibility	Possible

With the modeling of a rolling neutrophil as the initial motivation of this research, a comparison is made below in Figure 46 of diagrams depicting the rolling motion of an EAP rolling robot and another depicting the rolling motion of a neutrophil cell.

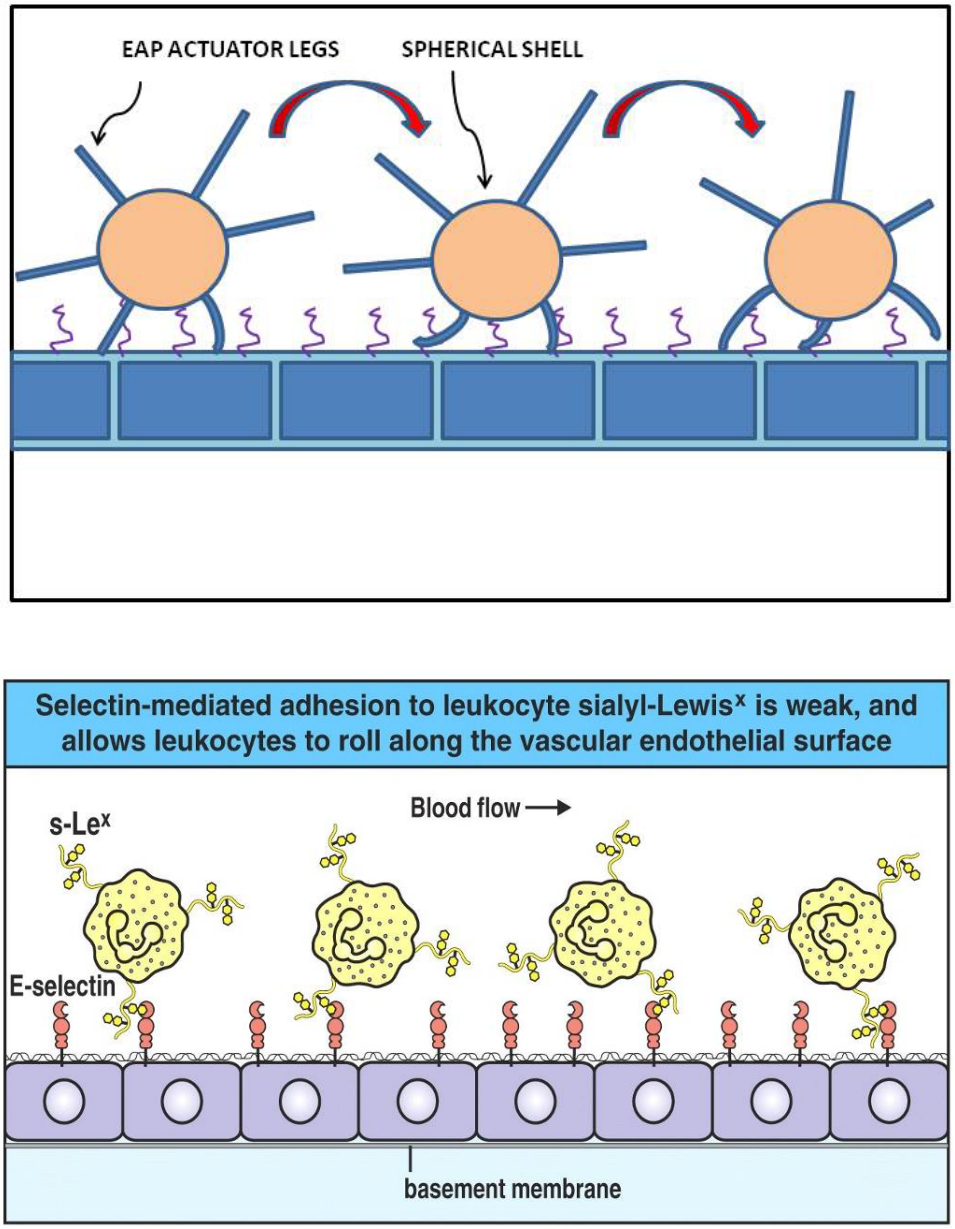

Figure 46. A comparison of a miniaturized rolling robot (Above) and a rolling neutrophil (Below) [12].

5.2 Future Work

One of the most important outcomes of this preliminary research was to provide direction and guidance for future research projects. Future research could be performed to improve many areas including biocompatibility, environment testing, actuator design, actuator timing, material improvement, and implementation of new technologies thus compounding the potential capability.

Further research on the effects of shape and electrode placement could provide specific deflections and force outputs. The electrode location on the IPMC can result in a wide variety of movements. This is especially useful for fine adjustments of force output and displacements. Specifically, this could be useful for the application in fluid flow environments to help generate the rolling motion. By minimizing the flat IPMC actuators' surface areas on the underside of the rolling robot with respect to the incident fluid flow and maximizing the surface area with respect to the fluid flow direction on the top of the rolling robot, the added force on the IPMC on the top of the rolling robot caused by the fluid flow with help to create the rolling motion. This concept is shown in Figure 47 in a simplified version with only two actuators.

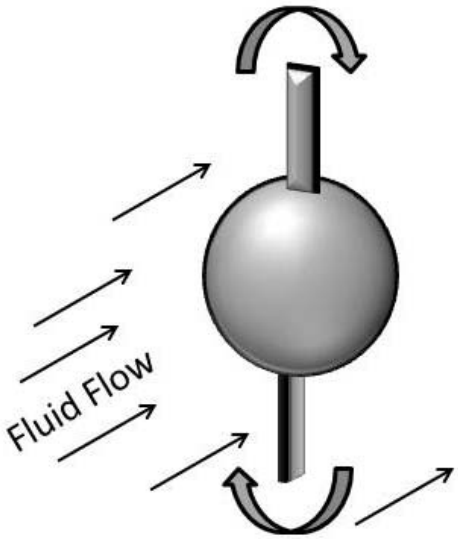

Figure 47. Orientation of IPMC actuators with respect to the fluid flow.

Clearly, this is a drastically simplified case as the actual robot would have several more legs. However, the concept is independent of the number of legs. That means any actuator legs on the upper portion of the sphere would be oriented to maximize the force caused by the fluid flow while the lower hemisphere of the rolling robot orients its actuators to minimize the force caused by the incident fluid flow. This concept does result in more complex control systems to sense which actuators to orient with or against the fluid flow. However, it does have the reverse capability to help slow the rolling motion. A capability such as this reinforces the concept that the material selection should supplement and enhance the biomimetic motion and not impede on the detailed characteristics of a rolling neutrophil. This concept could be utilized help mimic the slow rolling mechanism of a neutrophil.

Another area for future work is in the area of increasing the force output. Typically, the force output of IPMC actuators is relatively low. Further research could be done in experimenting with thicker membranes to achieve a higher force output. One possibility is to investigate a multilayered IPMC. The idea is similar to that of multilayer piezoelectric materials to increase the force output. However, the design would require a unique electrode configuration to electrically isolate the independent layers thus avoiding short circuiting the system.

As the design is miniaturized to the micro-scale, other biological interactions will become more important. For example, the molecular interactions that dominate the binding process of the neutrophil to the endothelial cell walls cannot be neglected at that scale. To more closely mimic the interactions attempting to be modeled, more research could be done on coatings that contain actual chemicals recognized or released by neutrophils. This sensing could enable the robot to sense where the inflammatory response is occurring, and initiate adhesion resulting in the slow rolling near the target region. This would not only allow the rolling robot to model neutrophil rolling from a locomotion standpoint, but also from a chemical or molecular interaction level.

Furthermore, the platform of this actuator design may soon allow for the useful implementation of recent technological advances with other research in the biotechnology industry. One such example is the incorporation of microsensors to the device. Microsensors have been fabricated on polymer substrates for such applications of sensing targeted chemicals in the blood. By combining the biomimetic motion capable of this robot design, with the ability to sense glucose or potassium ions, an extremely useful medical device could be fabricated. The

following two sensors are examples of potential devices that could be incorporated with the rolling robot resulting in powerful medical device.

5.2.1 Flexible Glucose Coil

Another recent technological advance has been the flexible coil biosensor. This type of sensors has been designed and manufactured for microcatheter-based cardiovascular in vivo monitoring. The sensor used to test this design, is a glucose sensor. Typically, glucose sensors have made use of amperometric detection. Materials used for such applications include glass, silicon, and other brittle or inflexible materials. These materials have resulted in larger packaging requirements of the sensors and thereby limit the usable environments and scaling [13].

The new design uses a spirally-rolled Kapton film to form the three dimensional device. The braided design yields the degree of rigidity necessary for cardiovascular catheterization. Nearly, all of the existing packaging of sensing mechanisms involves the assembly of rigid sensors onto commercially available catheters. The overall design results in a flexible tube for which multiple sensors can be mounted on both the internal and external surfaces of the coil. The design (Figure 48) reduces the complexity of wiring issues in conventional catheterized sensors [13].

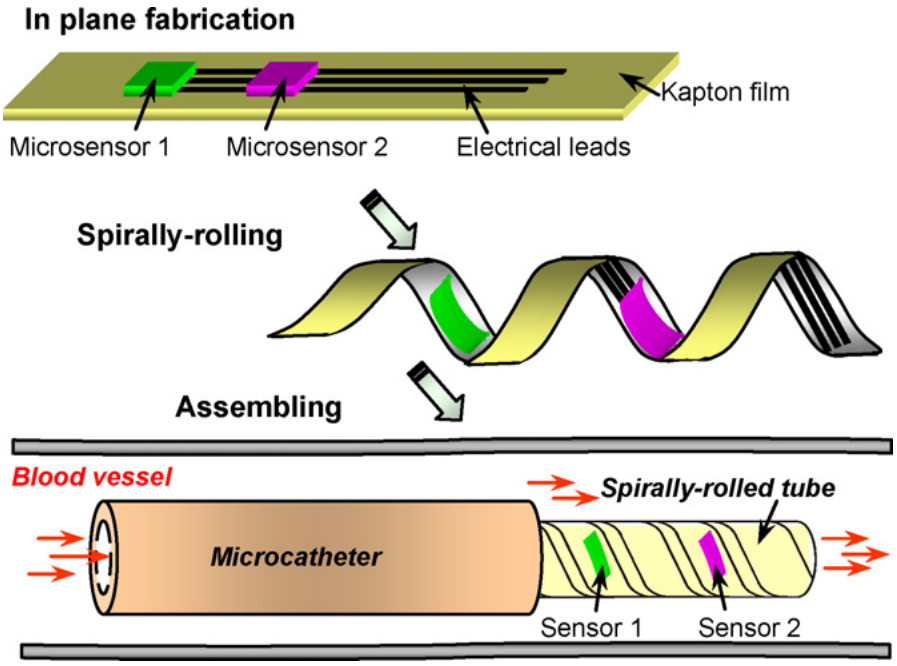

Figure 48. Flat and curved glucose sensor [13].

The coil glucose sensor begins with the in-plane assembly. Kapton film attached to a silicon wafer allows for the flat processing and easy removal after fabrication. Next, 1500 Å thick gold was deposited on 3-in. Kapton film with 200 Å thick adhesive layer of chrominium. Subsequently, the gold layer was formed into three electrode patterns constructing the glucose sensor and seed layer for the silver electroplating to serve as a reference electrode. This is shown in Figure 49 [13].

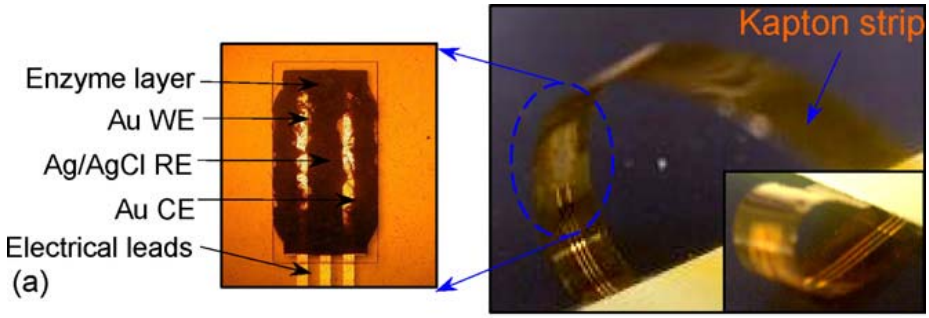

Figure 49. Formation of rolled sensor [13].

Two different spiral rolling methods were used and tested. Method one resulted in an overlapping region while method two used a braided structure without overlapping. However, both methods allowed the adhesive to cure and were then dipped into polyurethane in order to create a thin film thus improving biocompatibility. Both methods are shown in Figure 50 [13].

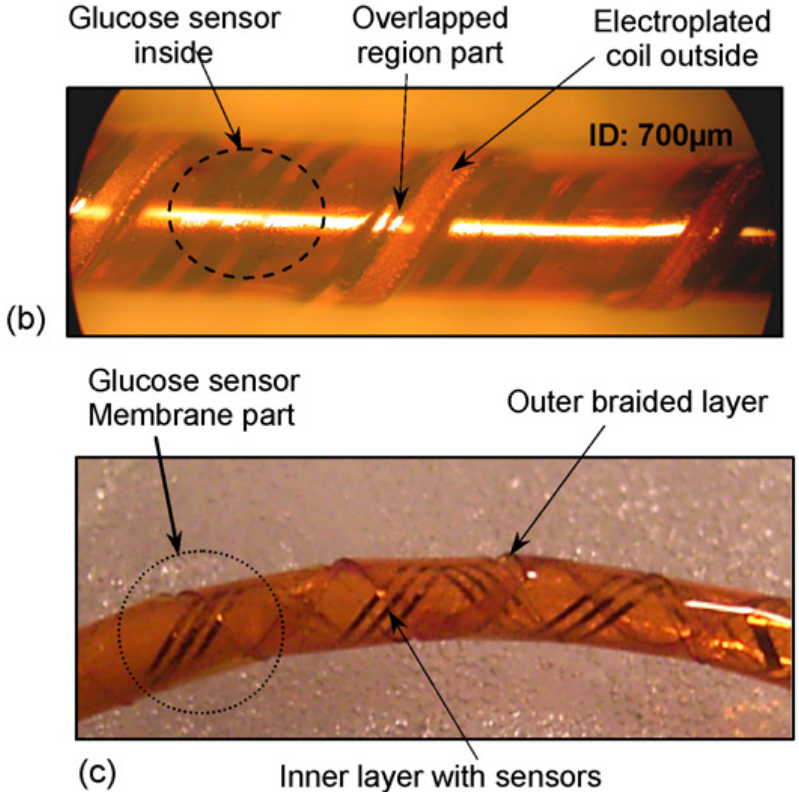

Figure 50. Photographs of overlapped and braided sensors [13].

Testing was performed on both methods to determine the most appropriate for the application. Compression testing was done to compare the stiffness of the two designs. The overlapped method was found to be less stiff, but to the extent that it was not suitable for navigating the vascular network [13]. Also, the inner and outer walls of the coil were not smooth due to the overlapped regions. This initiated flow disruption which may lead to inaccurate results. Furthermore, if any part of the overlapped design was damaged, the structural stability was compromised. The braided design was stable and performed even if a section was damaged. Also, the smoother surfaces of the braided design did not disrupt normal blood flow nor did it

harm the blood vessel endothelium. The obvious method to be used after testing was the braided design [13].

The results showed that the glucose sensors could be successfully fabricated and implemented on a flexible polymer base and rolled spirally into diameters ranging from 700 μm to 1.6 mm. The compact packaging of the sensor on the polymer film led to relatively easy integration to existing medical devices. This range allows implementation into existing commercially available micro catheters. The braided design yielded the correct axial and flexural rigidity for correct navigation control in cardiovascular catheterization applications. The basic design is generalized for any type of sensors. Depending on the application, a variety of sensors can be potentially fabricated and implemented on the platform of the tube micro-catheter. Future research may allow for wireless communication of the sensor along with controllable micro-actuators to allow un-tethered navigation [13].

5.2.2 Myocardial Ischemia and Potassium Sensing

Myocardial Ischemia (MI) also known as Ischemic Heart Disease (IHD) is characterized by a lack of blood supply to the heart muscle. MI affects millions of people and there is a need for a biosensor that would reduce the number of fatalities result from this condition [14]. This disease is usually due to coronary heart disease (athleroschlorsis of the coronary arteries). Increased risk for occurs with age, smoking, hypertension, and high cholesterol. With MI, the myocardium cells no longer contract correctly merely seconds after the onset of ischemia. If this is not rectified, myocytes become irreversibly injured and undergo cellular necrosis [35].

Research is being done on implantable microsensors designed to provide feedback on key information of MI. The proposed design would have passive wireless microsensors injected into the myocardium tissue. These sensors have the capability to provide doctor's a means of monitoring heart conditions, which could ultimately lead to the prevention of a heart attack or heart failure [35].

Extensive research has been performed on studying the basis of the mechanisms involved with MI. From that research, it has been shown that only seconds after the onset of MI, the levels of extracellular potassium increase suddenly from 5 mM to 10-20 mM by shrinking of the extracellular space and/or an increase of K^+ efflux of the cells. Though the basic mechanism which causes this almost instantaneous change in ion concentration is not fully understood, it provides a good parameter to monitor using microsensors [35].

The device has been designed to monitor, with sufficient resolution of time and space, ionic species important in MI. The microsensor is designed to be implanted directly into the myocardial muscle. By attempting to implant such a sensor on dynamic muscle tissue, certain challenges exist. This design requires a small size, mechanical flexibility to interact with the dynamic tissue without causing damage, high selectivity of ionic species, high sensitivity to low concentrations of extracellular ions, and above all, biocompatibility [26,35]. Shown in Figure 51 is a schematic of the sensor [35].

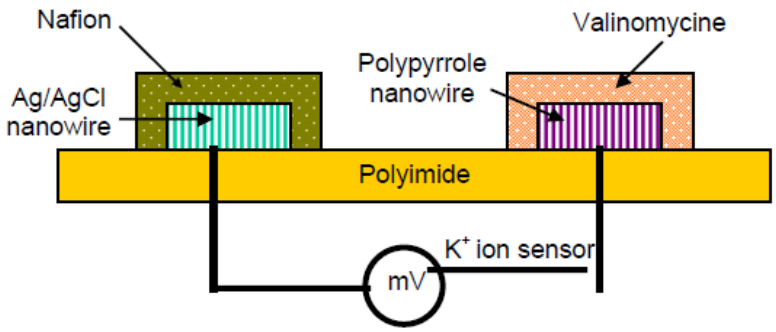

Figure 51. Schematic of potassium ion sensor [35].

With the requirements guiding the design, an all-solid state biosensor was chosen. This solid state basis eliminates the need for an inner filling solution typically found in ionic sensors. Nanowire is also implemented to optimize sensitivity and stable measurement. With potassium as the ion to be monitored, a conducting polymer nanowire is made of polyprrole which acts as an ion to electron transducer. Valinomycin and Nafion were selected as the ion selective membrane.

By further researching and combining the topics discussed above, the rolling robot could provide an extremely useful platform for a variety of devices including medical diagnostics, minimally invasive procedures, drug delivery, biological simulations, and many other uses. The wide range of applications is in part due to the rolling robot's flexible design capabilities that can be engineered to meet the requirements for the desired function. From the arbitrary posture of the design to the shell of the robot and the actuation legs, these design features have the potential to be engineered to meet the requirements of the specific application.

SUPPLEMENTAL INFORMATION

ACRONYMS

CP- Conducting Polymer

CNT- Carbon Nanotube

DEA- Dielectric Elastomer Actuator

EAP- Electroactive Polymer

EAC- Electroactive Ceramic

ERF- Electrorheological Fluid

ERI- Environmental Robots, Inc.

ICAM-1- Intercellular Adhesion Molecule -1

IPG- Ionic Polymer Gel

IPMC- Ionic Polymer Metal Composite

LCE- Liquid Crystal Elastomer

MEMS- Micro-Electrical-Mechanical Systems

MI- Myocardial Ischemia

PMN - Lead-Magnesium-Niobate

PVDF- Poly-Vinylidene Fluoride

PZT- Lead-Zirconate-Titanate

SMA- Shape Memory Alloy

TNFα - Tumor Necrosis Factor α

DEFINITIONS

Actuator- A device that converts a signal into a mechanical movement.

Biomimetic- The application of biological methods and systems found in nature to the study and the design of engineering systems and modern technology.

Inflammatory Response- A tissue reaction to an injury or an antigen that may include pain, swelling, itching, redness, heat, and loss of function. The response may involve dilation of blood vessels and consequent leakage of fluid, causing edema; leukocytic exudation; and release of plasma proteases and vasoactive amines such as histamine [16].

Neutrophil- A type of white blood cell, specifically a form of granulocyte, filled with neutrally staining granules, tiny sacs of enzymes that help the cell to kill and digest microorganisms it has engulfed by phagocytosis.

Pathogen- An infectious agent that causes disease or illness to the host.

Piezoelectric Material- Materials (notably crystals, certain ceramics, and bone) with the ability to generate an electric potential in response to applied mechanical stress.

Smart material- Materials that respond in a predicted manner to a stimulus such as pH, temperature, electric or magnetic fields, or force changes.

REFERENCES

1. Anson, Tony. "Shape Memory Alloys – Medical Applications," *Materials World* 7, no. 12 (1999): 745-747.

2. Bar-Cohen Y. and Leary S. Overviews of EAP Technologies. "EAP in the World." http://eee.deu.edu.tr/~ozkurt/eap/archive.htm.

3. Bar-Cohen, Y., T. Xue, J.O. Simpson, and J. Smith. "Low-mass muscle actuators using electroactive polymers (EAP)." In *Proceedings of SPIE's 5th Annual International Symposium on Smart Structures and Materials held in San Diego, CA.* 1998.

4. Buschow, K.H. Jürgen, Robert W. Cahn, Merton C. Flemings, Bernhard Ilschner, Edward J. Kramer, Subhash Mahajan. *Encyclopedia of Materials – Science and Technology*. Great Britain: Elsevier, 2001.

5. Caputo, Kelly. "Simulation of Neutrophil Rolling Dynamics and the Transition to Firm Adhesion." PhD diss., University of Pennsylvania, 2008.

6. Cohen, J.Y. Electroactive Polymers as Artificial Muscles. "Polymers and Separations Research Laboratory (PolySep)." http://www.polysep.ucla.edu/Research%20Advances/EAP/electroactive_polymers_as_artifi.htm.

7. Das, Tuhin and Lamkin-Kennard, Kathleen. "Design and Fabrication of Bio-Mimetic Milli-Robots." Rochester Institute of Technology.

8. Delves, Peter J. and Ivan M Riott. "Advances in Immunology: The Immune System," *The New England Journal of Medicine* 343, no. 1 (2000): 37-49.

9. EAMEX, Corporation. Ion Conductive Actuator. "Polymer Actuator Technology Summary." http://www.eamex.co.jp/index_e.html.

10. Gale, W.F. and T.C. Totemeier. *Smithells Metals Reference Book.* 8th ed. Great Britain: Elsevier, 2004.

11. Hin, Teoh Swee. *Engineering Materials for Biomedical Applications.* Hackensack, NJ: World Scientific, 2004.

12. Latting, John. The Role of E and P-Selection in Leukocyte Recruitment to Sites of Infection. "Davidson College." http://www.bio.davidson.edu/courses/immunology/Students/spring2006/Latting/home%20copy.html

13. Li, Chunyan, Han Jungyoup, and Ahn H. Chong. "Flexible Biosensors on Spirally Rolled MicroTube for Cardiovascular in vivo Monitoring," *Biosensors and Bioelectronics* 22 (2007).

14. Mallory, Glenn O. and Hajdu, Juan B. *Electroless Plating-Fundamentals and Application.* Norwich,NY: William Andrew Publishing/Noyes, 1990.

15. Medical applications of shape memory alloys. *L.G. Machado and M.A. Savi*. Brazilian Journal of Medical and Biological Research, 36 (6): 683, 2003.

16. *Mosby's Medical Dictionary,* 8th ed., s.v. "inflammatory response."

17. National Institute of Advanced Industrial Science and Technology. "Cyan-free electroless gold plating with high adhesion to various plastic films." www.aist.go.jp/.../20081105_2/20081105_2.html.

18. Oguro, Keisuke. Preparation Procedure: Ion-Exchange Polymer metal Composites (IPMC) Membranes. "Worldwide Electroactive Polymer (EAP) Webhub." http://ndeaa.jpl.nasa.gov/nasa-nde/lommas/eap/IPMC_PrepProcedure.htm.

19. Optotune. Electroactive Polymers. http://www.optotune.com/index.php?option=com_content&task=view&id=21&Itemid=40.

20. Oshida, Y. *Bioscience and Bioengineering of Titanium Materials.* Great Britain: Elsevier, 2007.

21. Piezo Systems, Inc. "Piezo actuators." www.piezo.com/tech2intropiezotrans.html.

22. Piezosystemjena. "Design of piezoactuators." www.piezojena.com/.../piezo_line/site__454/.

23. Piquepaille, Roland. Biomimetic Robots: A Photo Gallery. "Roland Piquepaille's Technology Trends." http://radio.weblogs.com/0105910/2004/10/11.html.

24. Quinn, Roger. Center for Biologically Inspired Robotics Research. "Case Western Reserve University." http://biorobots.cwru.edu/.

25. Roland, Piquepaille. Biomimetic Robots: A Photo Gallery. Last Updated 01/11/2004. http://radio.weblogs.com/0105910/2004/10/11.html.

26. Sadana, Ajit. *Engineering Biosensors – Kinetics and Design Applications.* Great Britain: Elsevier, 2002.

27. Schlesinger, Mordechey. Electroplating. "Electrochemistry Encyclopedia." http://electrochem.cwru.edu/encycl/art-e01-electroplat.htm.

28. Schwartz, Mel. *The Encyclopedia of Smart Materials.* Vol.1-2. Hoboken, NJ: John Wiley & Sons.

29. Shahinpoor, M., Y. Bar-Cohen, T. Xue, J.O. Simpson, and J. Smith. "Ionic Polymer-Metal Composites (IPMC) as Biomimetic Sensors and Actuators." In *Proceedings of SPIE's 5th Annual International Symposium on Smart Structures and Materials held in San Diego, CA,* 3324-3327, 1998.

30. Sheppard, Sally-Ann. Sheelagh A. Campbell, James R. Smith, Grongar W. Lloyd, Thomas R. Ralph, and Frank C. Walsh. "Electrochemical and microscopic characterisation of platinum-coated perfluorosulfonic acid (Nafion 117) materials." *The Analyst. (1998): 1923-1926.*

31. SMA/MEMS Research Group. How Shape Memory Alloys Work. "Shape Memory Alloys." http://www.cs.ualberta.ca/~database/MEMS/sma_mems/sma.html.

32. TRS Technologies. "Piezoelectric Actuators Overview." http://www.trstechnologies.com/Products/actuators.php.

33. Tucker, J.C. Actuation for Mobile Micro-Robotics. "North Carolina State University Electronics Research Laboratory." http://www.ece.ncsu.edu/erl/microrobotics/actuation/actuation.html.

34. Uhlig, Herbert H, R. Winston Revie. Corrosion and Corrosion Control. Third Edition. John Wiley and Sons. 1985.

35. Varadan , Vijay K. "The Role of Nanotechnology and Nano and Micro-Electronics in Monitoring and Control of Cardiovascular Diseases and Neurological Disorders." *Proceedings of SPIE.* Vol. 6258. San Diego, CA, 2007.

36. Yu, Min. Shen, Hui. Zhendong, Dai. "Manufacture and Performance Investigation of Ionic Polymer-Metal Composites (IPMC)." International Joint Conference of INABIO/SMEBA. 2006.

ACKNOWLEDGEMENTS

I would like to thank all of those involved for their expertise and input in their various professional fields. Specifically, I would like to thank my thesis advisor Dr. Kathleen Lamkin-Kennard for the opportunity to participate in this research and for all the guidance she provided during my research. This research was funded by the New Faculty Development Grant (Dr. Lamkin-Kennard). Also, I thank Dr. Massoud Miri for his direction during the fabrication process of the IPMC samples. Furthermore, I would like to thank the committee members Dr. Takacs, Dr. Kalathur Santhanam, and Dr. Tuhin Das for their guidance as well. Lastly, I would like to thank others who helped along the way: Dr. Brian Landi (RIT), Dr. Moshen Shahinpoor (University of Maine), Mansour Ravandoust (Environmental Robots, Inc.), Amanda Kristoff (fellow student), and Robert Marcello (fellow student).

********** REPRODUCTION PERMISSION STATEMENT **********

Permission Granted

MATERIAL SELECTION FOR THE ACTUATOR DESIGN FOR A BIOMIMETIC ROLLING ROBOT CONDUCIVE TO MINIATURIZATION

I, Zachary S. Dotson, hereby grant permission to the Wallace Library of the Rochester Institute of Technology to reproduce my thesis in whole or part. Any reproduction will not be for commercial use or profit.

JUNE 12, 2009. Signature of Author: _____

APPENDIX A.

Design and Fabrication of Bio-mimetic Milli-robots

By:

Dr. Tuhin Das
and
Dr. Lamkin-Kennard

DESIGN AND FABRICATION OF BIO-MIMETIC MILLI-ROBOTS

Investigators: Dr. Tuhin Das, Dr. Kathleen Lamkin-Kennard

Introduction

In recent years, the MEMS technology has revolutionized several areas of engineering and research. Robotics, and in particular mobile robotics, is beginning to reap the benefits of the MEMS technology through development of micro and millimeter scale robots. Millimeter scale robotic mechanisms, i.e. milli-robots, are the focus of the proposed research. Micro or milli-robots have the potential of revolutionizing several technological areas. For instance, miniature robots could be deployed individually or in swarms for reconnaissance, planetary exploration, performing operations in hazardous environments, etc. They could also be implanted into the human body for diagnosis, treatment, surgical procedures, and drug-delivery. In spite of recent progresses there still remain numerous challenges associated with miniaturization of mobile robots. Appropriate miniature power sources for satisfactory run-time, micro-fabrication of the mechanical assemblies, maneuverability, and computational requirements have posed hurdles in the development of miniature mobile robots.

In successful development of miniature robots, the choice of propulsion mechanism is critical. A simple yet effective mechanism must be designed to reduce complexity of fabrication, sensing, actuation, and control at miniature scales. To this end, the investigators propose a novel propulsion mechanism with superior maneuverability and ease of control. The design of this mechanism is motivated by the investigators prior research in robotics and bio-mimetics. Dr. Das has extensive experience in dynamical analysis and control of mobile robots. His doctoral research focused on self-propulsion with nonholonomic constraints, specifically on the development of a spherical mobile robot. Dr. Lamkin-Kennard's primary research is in the area of integrated systems analysis of physiological systems, with a specific focus on of flow and transport mechanisms in microscale blood vessels. At RIT, she has also developed several pneumatically controlled biomimetic robotic hand platforms.

In this project, feasibility of the proposed mechanism will be investigated in context of millimeter scale implementation. The use of MEMS based devices and powertrains, shape memory materials, and microfabrication techniques will be integral to the fabrication. The primary effort of this project will be to explore and optimize the propulsion mechanism so that it is readily implementable using available micro-fabrication techniques. Thus, the proposed mechanism will serve as a nominal concept and the final design will be driven by the available miniaturization technologies. This approach is necessary since miniaturization will presumably be the primary challenge in our research.

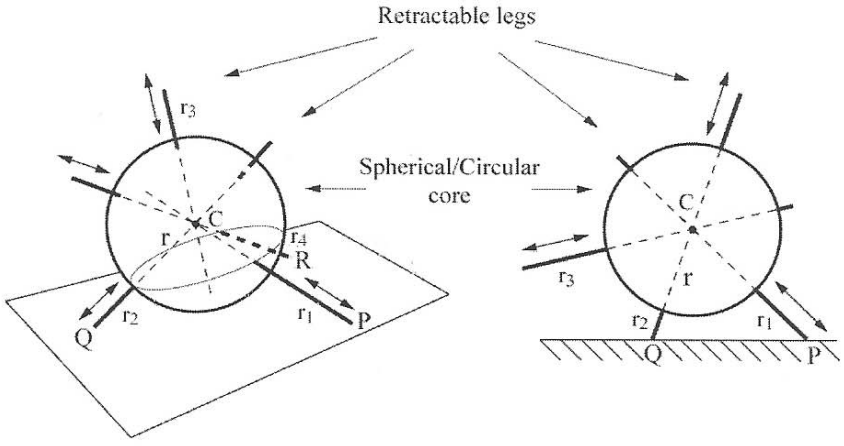

(a) Mechanism in three dimensions (b) Planar version

Figure 1: Schematic diagram of proposed miniature mobile robot

Robotic Mechanism

A schematic diagram of the proposed robotic mechanism is shown in Fig.1. Fig.1 (a) depicts the complete robotic configuration in three dimensions, whereas in Fig.1 (b) we illustrate a planar version of the mechanism which is a special case of the three dimensional version. The design is inspired by a spherical mobile robot [1]-[4]. A spherical robot has several advantages such as superior maneuverability, structural robustness and absence of postural preference. However, the path planning and control problems are complex [2] and have posed as hindrances to the development of such robots. The proposed mechanism combines the advantages of the spherical robot with ideas from cellular locomotion to significantly simplify the control issues. The salient features of the mechanism are listed below

- *Four and three legs are used for the 3D and planar versions respectively.* In the three dimensional version, the legs will form a regular *tetrahedron.* In the planar version the legs will be 60^{o} apart. A larger number of legs will result in smoother motion of the robot but at the same time increase sensing, actuation, and hardware complexity.
- *The means of propulsion lies external to the circular core*. This is in contrast to spherical mobile robots which have internal propulsion mechanisms [3], [4]. Although internal propulsion is appealing, such mechanisms require complicated and computation-intensive control strategies.
- *The mechanism retains the maneuverability of a spherical shape.* The robot can generate motion starting from any arbitrary configuration. The robot does not lose posture in any configuration and hence regaining posture is not a consideration.
- *The mechanism does not rely on weight unbalance for propulsion.* The mechanism uses surface friction rather than eccentric weight to generate propelling moment. This reduces the necessity of a relatively heavy central core. This is important, especially for miniature robots which are likely to be light-weight.

An important feature of the proposed milli-robot is its *bio-mimetic* locomotion. While bio-mimetic locomotion is prevalent in many robotic designs, these motions are primarily derived from locomotion in higher level macroscopic living organisms such as human or insect locomotion. Instead, our bio-mimetic mechanism is inspired by the fundamental rolling motion necessary for cellular locomotion. Numerous biological processes in the human body efficiently transport materials, such as cells, chemical species, or nutrients to target sites. The *inflammatory cascade* is an example of such a process. Leukocyte adhesion and *neutrophil* rolling phenomena are important components of the inflammatory cascade. Neutrophil rolling is the process that enables neutrophils to get from the blood stream to a target location site along a blood vessel wall to assist in fighting infection (acute inflammatory response) [5]. The proposed work seeks to mimic the neutrophil rolling process as a biomimetic locomotion mechanism for the milliscale robot, thus enabling the robot to get to its desired site of action. A key advantage of this mechanism is that it can easily be implemented in an aqeuous environment, a critical design requirement for future implementation in the human body.

Neutrophil Rolling and Adhesion

Neutrophil rolling and adhesion occurs in response to the inflammatory immune response. When certain pathogens in the body are encountered, macrophages release cytokines [6]. One of the cytokines released is Tumor Necrosis Factor α (TNFα). TNFα causes endothelial cells, lining microvessel walls, to express surface adhesion molecules. Neutrophils are initially drawn to the vessel wall, near the pathogen, as a result of cytokine signaling. Once in close enough proximity to the wall, the surface adhesion molecules on the vessel walls transiently bind with glycoproteins expressed on the surfaces of the neutrophils. Initially, only a small number of bonds are formed that are easily broken as a result of the shear forces imposed on the neutrophil by the flowing fluid in the vessel. The formation and breaking of transient bonds in the presence of shear flow is what ultimately causes the cell to roll. Over time, stronger bonds form with additional surface molecules, the cells eventually roll slower, and neutrophils finally become

firmly adherent (tight binding in Figure 2). Following firm adhesion, the cells undergo a conformational change and move across the vessel wall into surrounding tissue in a process known as diapedesis. Once in the tissue, the neutrophils assist in combating the pathogen. The steps in the adhesion cascade are illustrated in Figure 2.

The entire neutrophil rolling process is easily duplicated in the lab using protein coated microspheres and surfaces treated with adhesion molecules [7] and could thus be adapted as a transport mechanism for the milli-robot. The legs of the milli-robot will mimic the glycoproteins found on the surface of the neutrophil and the propulsion mechanism will mimic the neutrophil rolling process. In its final configuration, the robot could be delivered to specific target sites in the body using biochemical targeting mechanisms. Numerous applications have adapted a similar methodology for targeted delivery of drugs, contrast agents, or other applications in the body [8].

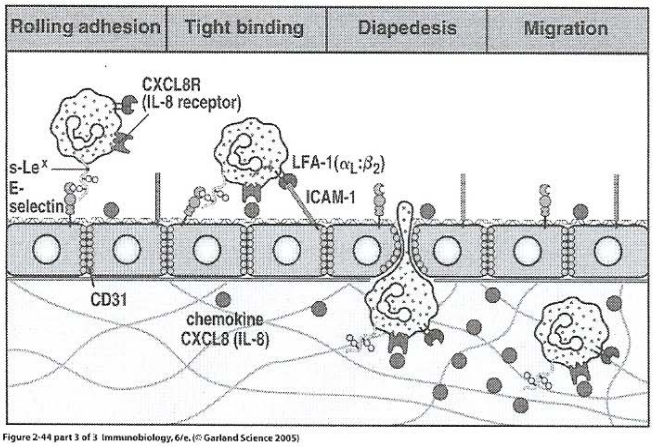

Figure 2: The neutrophil adhesion cascade. In the above diagram, the yellow spheres represent neutrophils and the blue squares represent endothelial cells. The cells are initially attracted to the surface through chemokine signaling then transiently bind to E-Selectin or ICAM-1 on the endothelial cell surface.

Robot Design and Fabrication

The proposed research will primarily emphasize on the design and implementation of the appendages of the robotic mechanism in millimeter scales. Our objective is to design the kinematics of the appendages in a manner that admits convenient micro-fabrication without compromising their mobility and that minimizes sensors, actuators and the overall power consumption. In addition to the linear motion of the legs as shown in Fig.1, we will provide additional degrees of freedom in the form of rotational motion, as shown in Fig.3 (a). The added rotational degrees of freedom will enhance the functionality of the robot in terms of negotiating intricate terrains and constrictions. This is especially important considering the future objective of implanting such a robot into the human body. The rotational degrees of freedom will introduce reconfigurability by allowing a second mode of locomotion, namely a *spider-like locomotion*, as shown in Fig.3 (b). Evidently, this second mode of locomotion is significantly more complicated and will require more sophisticated controls. With this flexibility, depending on the mission requirements, the robot will be able to switch between the two modes of locomotion.

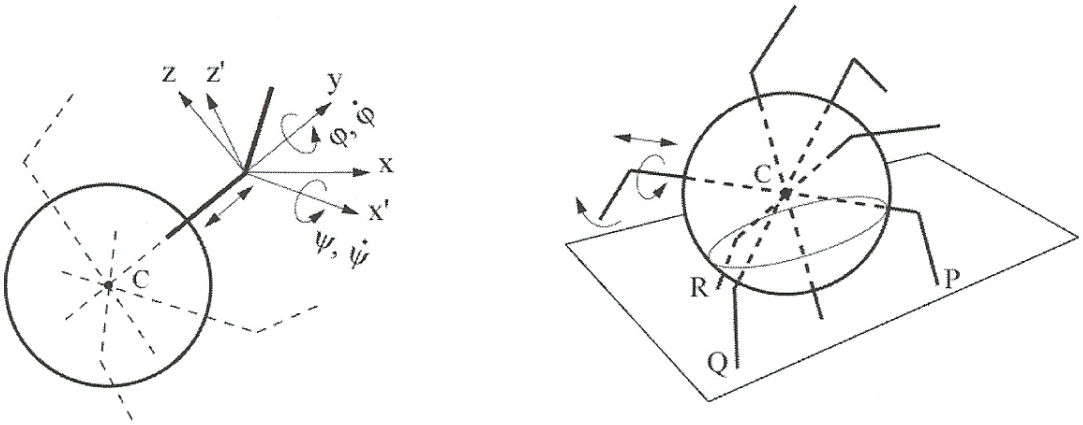

(a) Additional degrees of freedom

(b) Alternate means of locomotion (spider-like motion)

Figure 3: Enhanced mobility of the robotic mechanism

The investigators will perform a thorough survey of available materials and micro-fabrication techniques to optimize the kinematic design of the legs. The desired locomotion will be realized through implementation of miniature power-trains. The use of shape memory alloys (SMA) will also be explored as a means of actuation.

Motion Analysis and Control

Dr. Das has initiated analytical research to address motion planning and control for the mechanism. The analysis for the planar version in Fig.1 (b) has yielded elegant results and a geometric control strategy has been developed based on kinematic properties of the system. In the following discussion, we present an overview of the analytical treatment of the problem. The governing system equations are derived using the *Euler-Lagrange* formulation. From Fig.2 (b) and considering the inertias of the legs to be negligible in comparison to the core, the equations of motion are:

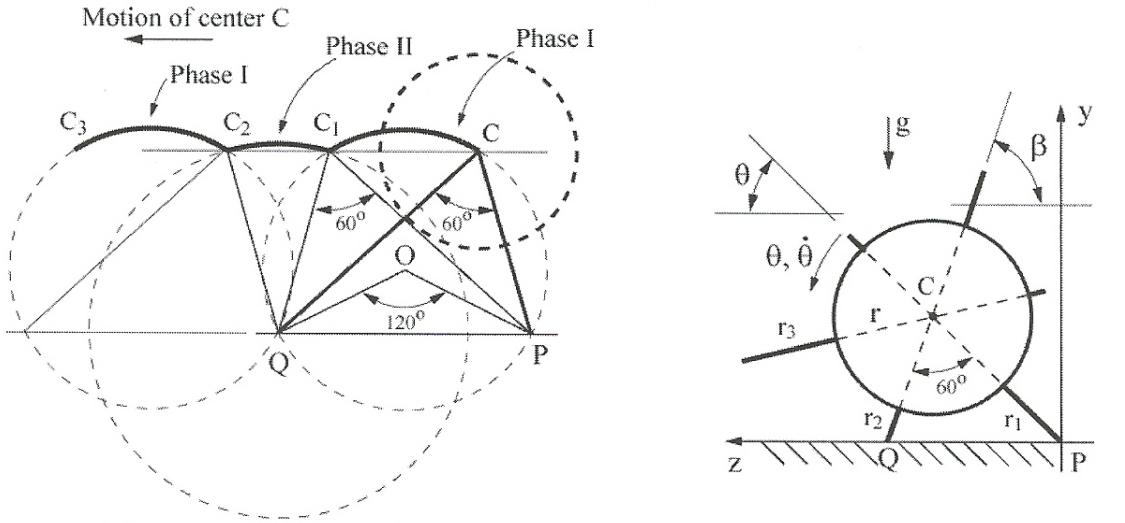

(a) Geometric motion control strategy

(b) Diagram with generalized coordinates

Figure 3: Generalized coordinates and geometric control strategy

$$\begin{aligned}&\left[I_c + M_d\left(r + r_1\right)^2\right]\ddot{\theta} + 2M_d\left(r + r_1\right)\dot{r}_1\dot{\theta} + M_d g\left(r + r_1\right)\cos\theta = 0\\&\ddot{r}_1 - \left(r + r_1\right)\dot{\theta}^2 + g\sin\theta = 0\end{aligned} \tag{1}$$

where, I_c is the moment of inertia of the disk about its center C, M_d is the mass and r is the radius of the disk, and θ and r_1 are the generalized coordinates used to mathematically express the motion of the disk.

The locomotion of the robot is designed using a repeating sequence of two phases, namely phase I and phase II, as shown in Fig.3 (a). In both phases, the center of the disk traces circular paths. Phase I is a controlled motion with *two-point contact* with the ground. During this phase, $(r+r_1)$ is increased from CP to C_1P through feedback based actuation. The *kinematic constraint* $\angle PCQ = 60^o$, (i.e. the angle between any two legs is constant and is 60^o for this design) automatically causes C to trace a circular arc CC_1 with center O. This can be proven using the *invariance property of inscribed angle of a circle* and is the unique trajectory of C during phase I that satisfies the kinematic constraint. The kinematic constraint also reduces the number of generalized coordinates, since during phase I,

$$\left(r + r_1(t)\right)\frac{\sin 60^\circ}{\sin\left(120^\circ - \theta(t)\right)} = PQ = const. \tag{2}$$

At C_1, the motion switches to Phase II which uses a *one point contact* with the ground. During phase II, the center of the robot traces a circular arc centered at Q from C_1 to C_2. Phase II constitutes of an uncontrolled motion where essentially the robot utilizes its kinetic energy gained during phase I to tip over about Q. Phase II is followed by another phase I motion and so on.

The above *analysis of the planar motion can be directly extended to the three dimensional version*. In the later case, the motion of the center C will be constrained along a *spherical surface instead of a circle* with the robotic motion switching between two and three point contacts with the ground. With this approach, the control strategy is significantly simplified as we favorably utilize the inherent kinematic constraint of the robot and can potentially lead to reduced sensor requirements. The simplicity of the control algorithm will be particularly helpful in miniaturization and in general will directly contribute to hardware simplification and costs effectiveness.

References

[1] Das, T., and Mukherjee, R., 2006, "Reconfiguration of a Rolling Sphere: A Problem in Evolute-Involute Geometry," *ASME Journal of Applied Mechanics*, **73**(4), pp. 590-597.

[2] Das, T., and Mukherjee, R., 2004, "Exponential Stabilization of the Rolling Sphere: An Intractable Nonholonomic System," *Automatica,* **40**, pp. 1877-1889.

[3] Das, T., and Mukherjee, R., 2001, "Dynamic Analysis of Rectilinear Motion of a Self-Propelling Disk with Unbalance Masses," *ASME Journal of Applied Mechanics*, **68**(1), pp. 58-66.

[4] Das, T., Mukherjee, R., and H. Yuksel, 2001, "Design Considerations in the Development of a Spherical Mobile Robot," *Proc. SPIE Vol. 4364, SPIE 15th Annual International Symposium on Aerospace/Defense Sensing, Simulation, and Controls*, Orlando, FL.

[5] K. Lamkin-Kennard, J.Y.H. Chuang, M.B. Kim, I.H. Sarelius and M.R. King, 2005. "The distribution of rolling neutrophils in venular convergences," *Journal of Biorheology* **42**, pp. 363-383.

[6] K. Lev, 2001, Physiology of Inflammation. New York: Oxford Press, Inc.

[7] M.R. King, M.B. Kim, I.H. Sarelius and D.A. Hammer, 2003, "Hydrodynamic interactions between rolling leukocytes in vivo", *Microcirculation* **10**(50), pp. 410-409.

[8] Dunehoo, A.L., Ande, M., 2006, "Cell adhesion molecules for targeted drug delivery", J. Pharm. Sci. 95(9), pp. 1856-1872.

APPENDIX B.

SMA Composition Properties

From Smithells Metals Reference Book (8th Edition) [10].

Table 15.9 COMPOSITIONS AND TRANSFORMATION TEMPERATURES OF SHAPE MEMORY ALLOYS

Alloy composition wt%[1]	M_s *temperature at zero stress at* °C	A_s *temperature at zero stress* °C	*Maximum shape memory strain* %	*Reference*
Au–28at% Cu–46 At.% Zn	−15			6
Au–47.5% Cd	60	70		13
Au–12.9% Cu–25.5% Zn	−100		1.55	32
Au–15.2% Cu–28.0% Zn	−50		~1.0; brittle g.b. phase	32

(continued)

Alloy composition wt%[1]	*M_s temperature at zero stress at* °C	*A_s temperature at zero stress* °C	*Maximum shape memory strain* %	*Reference*
Au–16.0% Cu–32.3% Zn	−118		ditto; Zn too high	32
Au–22.3% Cu–31.4% Zn	−64		2.15	32
Au–28.7% Cu–31.1% Zn	< −196		?; Zn too low	32
Cu–2.50% Al–31.75% Zn	−105		10.25	15
Cu–3.94% Al–25.60% Zn	54	48	> 2.0	23
Cu–4.00% Al–26.10% Zn	24	23	14% (5–6% reversible)	20
Cu–6.00% Al–22.00% Zn	−50		4.8	15
Cu–7.50% Al–17.00% Zn	−10		4	15
Cu–11.75% Al–6.00% Zn	50		2.8	15
Cu–10.50% Al–7.25% Zn	140		3.9	15
Cu–11.25% Al–4.75% Zn	170		2	15
Cu–11.75% Al–2.50% Zn	250		1.9	15
Cu–4.90% Sn–31.25% Zn	−70		1	15
Cu–1.75% Si–34.50% Zn	−140		6.3	15
Cu–2.25% Si–31.25% Zn	−50		6	15
Cu–3.25% Si–27.50% Zn	75		2.95	15
Cu–12.00% Al–2.00% Mn	240		0.95	15
Cu–11.25% Al–4.25% Mn	160		0.45	15
Cu–10.75% Al–6.00% Mn	100		0.45	15
Cu–10.40% Al–7.00% Mn	83			21
Cu–10.60% Al–7.00% Mn	52			21
Cu–11.00% Al–7.00% Mn	5			21
Cu–11.10% Al–7.00% Mn	−10			21
Cu–12.50% Al–1.00% Fe	300		1.75	15
Cu–12.50% Al–8.00% Fe	250		1.1	15
Cu–13.25% Al–2.75% Ni	82		2.9	15
Cu–8.0% Al	N.A.	N.A.	1.05	16
Cu–4.0% Si	N.A.	N.A.	1.4	16
Cu–14.2% Al–4.3% Ni	−20	−15		8
Cu–40% Zn	−70	−120		8
Cu–34.7% Zn–3.0% Sn	−52	−50	4.5 (polycrystal) 8.5 (single crystal)	9
Fe–15% Cr–15% Ni–15% Co	< −196	−196 to 40	1.45	16
Fe–20% Cr–10% Ni–1% Al	< −196	−196 to 40	0.45	16
Fe–20% Mn–3.75% Ti	< −196	−196 to 40	1.4	16
Fe–20% Cr–15% Ni	< −196	−196 to 40	1.05	16
Fe–17% Cr–19% Ni	> −196	−196 to 40	0.9	16
Fe–30% Mn–6.5% Si	< 20	20 to 400	2.1	22
Fe–24% Mn–3% Si	123	188	1.5–1.75	24
Fe–26% Mn–4% Si	106	182	1.5–1.75	24
Fe–27% Mn–3% Si	103	176	1.5–1.75	24
Fe–28% Mn–3% Si	102	164	1.5–1.75	24
Fe–28% Mn–4% Si	62	162	1.5–1.75	24
Fe–29% Mn–4% Si	88	164	1.5–1.75	24
Fe–32% Mn–4% Si	27	134	1.5–1.75	24
Fe–33% Mn–4% Si	22	131	1.5–1.75	24
Fe–34% Mn–4% Si	8	127	1.5–1.75	24
Fe–35% Mn–4% Si	−10	123	1.5–1.75	24
Ti–50.2at% Ni	35	50	1.4 (reversible)	17
Ti–50.2at% Ni	10	57		18
Ti–50.2at% Ni	~25	~55	5.5% (~4% reversible)	19
Ti–56.4% Ni	5			26
Ti–55.5% Ni	10			26
Ti–55.0% Ni	35			26

Alloy composition wt%[1]	*M_s temperature at zero stress at* °C	*A_s temperature at zero stress* °C	*Maximum shape memory strain* %	*Reference*
Ti–53.7% Ni	75			26
Ti–54.8% Ni	62			27
Ti–52–56% Ni	~RT			1
Ti–53.5% Ni	98			2
Ti–54.0% Ni	140			2
Ti–54.5% Ni	170	175	8.0	2, 4
Ti–55.0% Ni	140			2
Ti–55.5% Ni	30			2
Ti–56.0% Ni	−25			2
Ti–56.5% Ni	−50			2
Ti–51at% Ni	28	62		7
TiNi[2]	166			3
TiCo	−238			3
$TiNi_xCo_{1-x}$[3]	166 where $x = 1$ −238 where $x = 0$			3
TiFe	~ − 269			
Ti–35% Nb	−175	184	~2.5	10
Ti–51.4% Ni–3.57% Co				
0.3 in. rod	−51	−40	6 to 10	11
0.003 in. foil	−65	−45	6 to 10	11
0.01 in. wire	−73	−51	6 to 10	11
Ti–55.0% Ni-0.07% C				
0.2 in. rod	21	60	6 to 10	11
0.003 in. foil	27	43	6 to 10	11
0.01 in. wire	18	43	6 to 10	11
Ti–54.6% Ni–0.06% C				
0.625 in. rod	43	71	6 to 10	11
0.003 in. foil	38	66	6 to 10	11
0.01 in. wire	32	54	6 to 10	11
Ti–47.0% Ni–7% Cu	63			27
Ti–44.5% Ni–10% Cu	52			27
Ti–32.0% Ni–22% Cu	74			27
Ti–27.0% Ni–29% Cu	20			27
Ti–47.0at% Ni–3at% Fe	−180	−88		30
Ti–52.85% Ni–0.28% Fe	34	35	8 (0.094 rad in torsion)	14, 33, 34
Ti–47.0at% Ni–9at% Nb	−90	−56 up to 55		30
Ti–50at% Pd	533	573	~2.0	28, 29
Ti–50at% Pd	510	520		36
Ti–50at% Pd	563	580	2.39	35
Ti–40.0at% Pd–10.0at% Ni	403	419	2.66	35
Ti–30.0at% Pd–20.0at% Ni	241	230	4.38	35
Ti–20.0at% Pd–30.0at% Ni	95	90	1.84	35
Ti–10.0at% Pd–40.0at% Ni	−18	−26		35
Ti–50.0at% Ni	55	80		35
Ti–5.0at% Pt–45.0at% Ni	29	36		35
Ti–10.0at% Pt–40.0at% Ni	18	−27		35
Ti–20.0at% Pt–30.0at% Ni	300	263	2.17	35
Ti–30.0at% Pt–20.0at% Ni	619	626		35
Ti–50.0at% Pt	1 070	1 040		36
Ti–44at% Pd–6at% Fe	321	335	5.0	28, 29
Ti–42at% Pd–8at% Fe	293	250		28
Ti–40at% Pd–10at% Fe	173	178		28
Ti–38at% Pd–12at% Fe	96	99		28
Ti–36at% Pd–14at% Fe	25	25		28
Ti–34at% Pd–16at% Fe	−49	−45		28

Table 15.9 COMPOSITIONS AND TRANSFORMATION TEMPERATURES OF SHAPE MEMORY ALLOYS—*continued*

Alloy composition wt%[1]	*M_s temperature at zero stress at* °C	*A_s temperature at zero stress* °C	*Maximum shape memory strain* %	*Reference*
Ti–42at% Pd–4at% Fe	228	216		28
Ti–40at% Pd–6at% Fe	119	124		28
Ti–38at% Pd–8at% Fe	18	3		28
ZrRu[4]	−233			3
ZrRh[4]	380			3
ZrPd[4]	727			3
U–4.0% Mo		200		31
U–4.5% Mo		80		31
U–5.0% Mo		50	3.2	31
U–6.0% Mo		−50		31
U–4.0% No		~250		31
U–5.0% Nb		~200		31
U–7.0% Nb		~100		31
U–14at% Nb	160	90	4.8	25
U–9at% Nb[5]	0	150		5
U–12at% Nb[5]	0	150		5
U–15at% Nb[5]	0	60		5
U–18at% Nb[5]	−196	0		5

[1] Unless otherwise stated.
[2] *See also* Figure 15.2.[3]
[3] *See* Figures 15.3.
[4] Non-linear interpolation between their compounds is possible. Relationship is of form $\log_e (M_s K) \propto x$ where x is in the range 0–1 in $Zr–Ru_x–Rh_{1-x}$ etc.
[5] M_s and A_s not accurately determined but are within these temperature ranges.

Table 15.10 PHYSICAL AND MECHANICAL PROPERTIES OF A TITANIUM–55% NICKEL SHAPE MEMORY ALLOY

Property	*Value*
Density	6.45 g cm^{-3}
M.p.	1 310°C
Magnetic permeability	< 1.002
Electrical resistivity	80 $\mu\Omega$ cm at 20°C 132 $\mu\Omega$ cm at 900°C
Coefficient of thermal expansion (24–900° C)	10.4×10^{-6} °C^{-1}
Mechanical properties at 20°C (i.e. below M_s)	
0.2% yield stress	207 MPa
UTS	861 MPa
Elongation %	22
Reduction in area %	20
Impact (unnotched)	159 J at 20°C 95 J at 80°C
Fatigue (rotating beam)	$>25 \times 10^6$ cycles at 483 MPa

Note
If recovery is prevented mechanicaly, the TiNi will exert a stress and is capable of doing work when heated to above the A_s temperature. Samples of Ti–55.0% Ni–0.07%*C* were capable of exerting a stress of up to 758 MPa at 171°C (*see* Figure 15.5). The amount of mechanical work which this alloy was capable of doing was 17–20 J cm^{-3} on heating from 24°C to 171°C.

APPENDIX C.

Ordered Materials

Ordered Material	Supplier	Cost
1. Nafion 117 by Dupont (15x15 cm) (7 mil thickness)	Fuel Cell Scientific	$ 80.00
2. Platinum ammine complex Product # 275905 (1g)	Sigma Aldrich	$ 105.00
3. Hydrazine Hydrate Product # 53847 (50ml)	Sigma Aldrich	$ 26.20
4. Hydroxylamine hydrochloride Product # LC155301 (500ml)	LabChem, Inc.	$ 31.00
5. Deluxe Complimentary Package (Includes: Two IPMC samples, variable power supply, and mounting device)	Environmental Robots, Inc.	$ 249.00

*Note: Refer to company websites for availability and ordering.

APPENDIX D.

Experimental Setup Figures

Experimental Setup

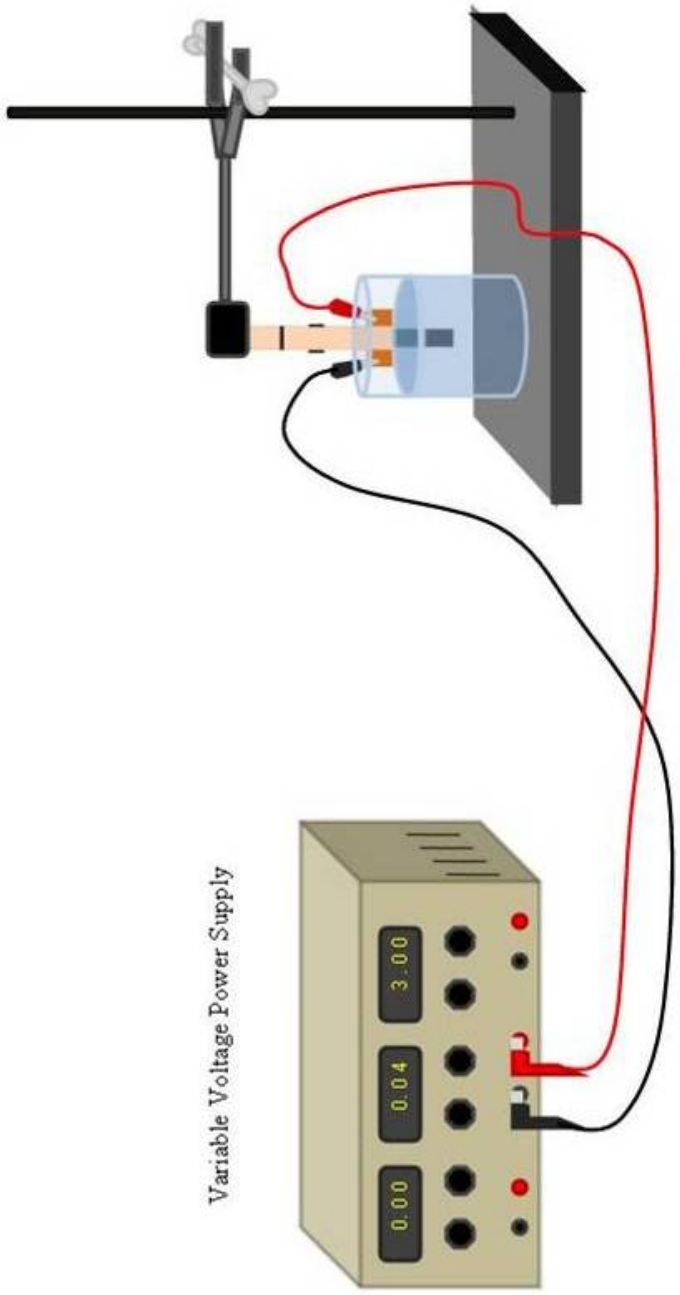

Clothespin and Copper Electrodes

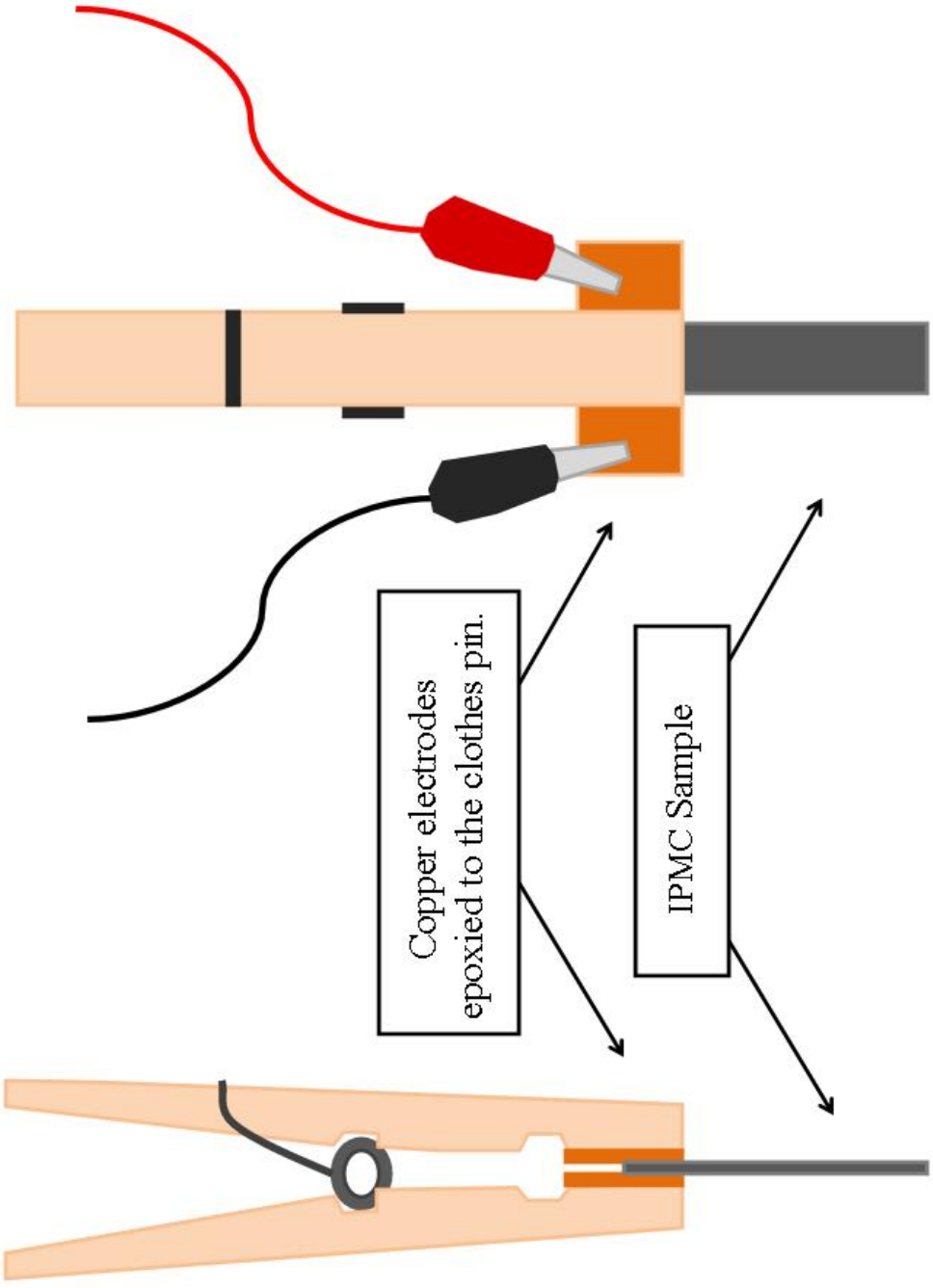

Deflection Testing Setup with ERI Kit

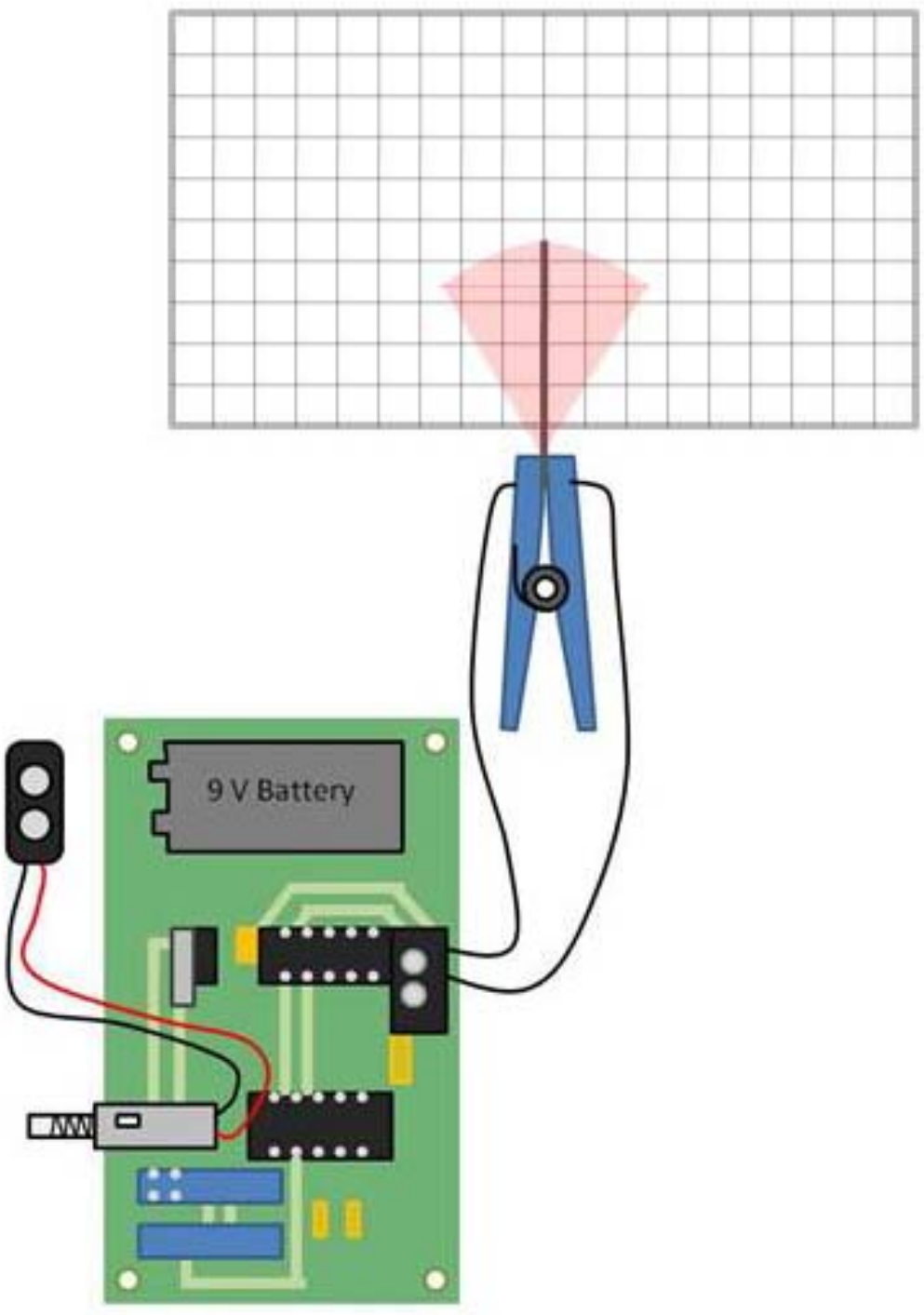

Force Output Testing Using Fabricated Materials

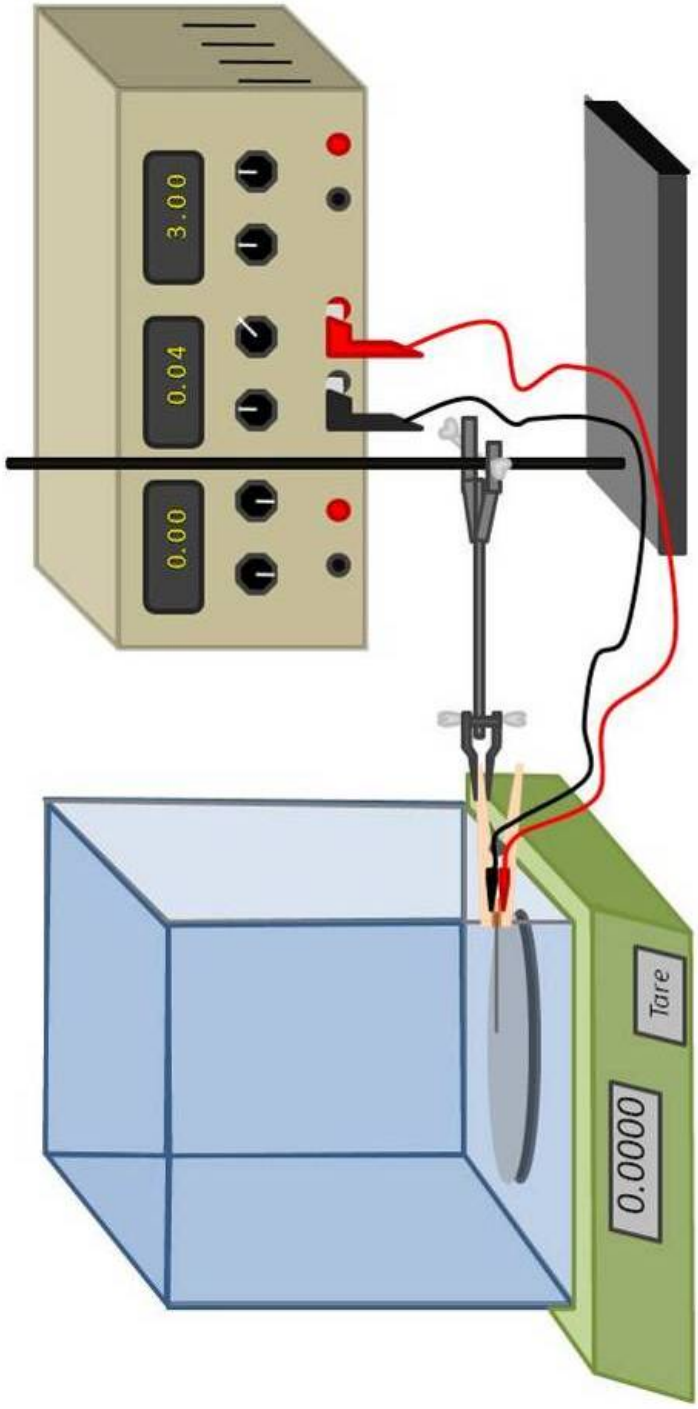

Force Output Testing Using ERI Kit

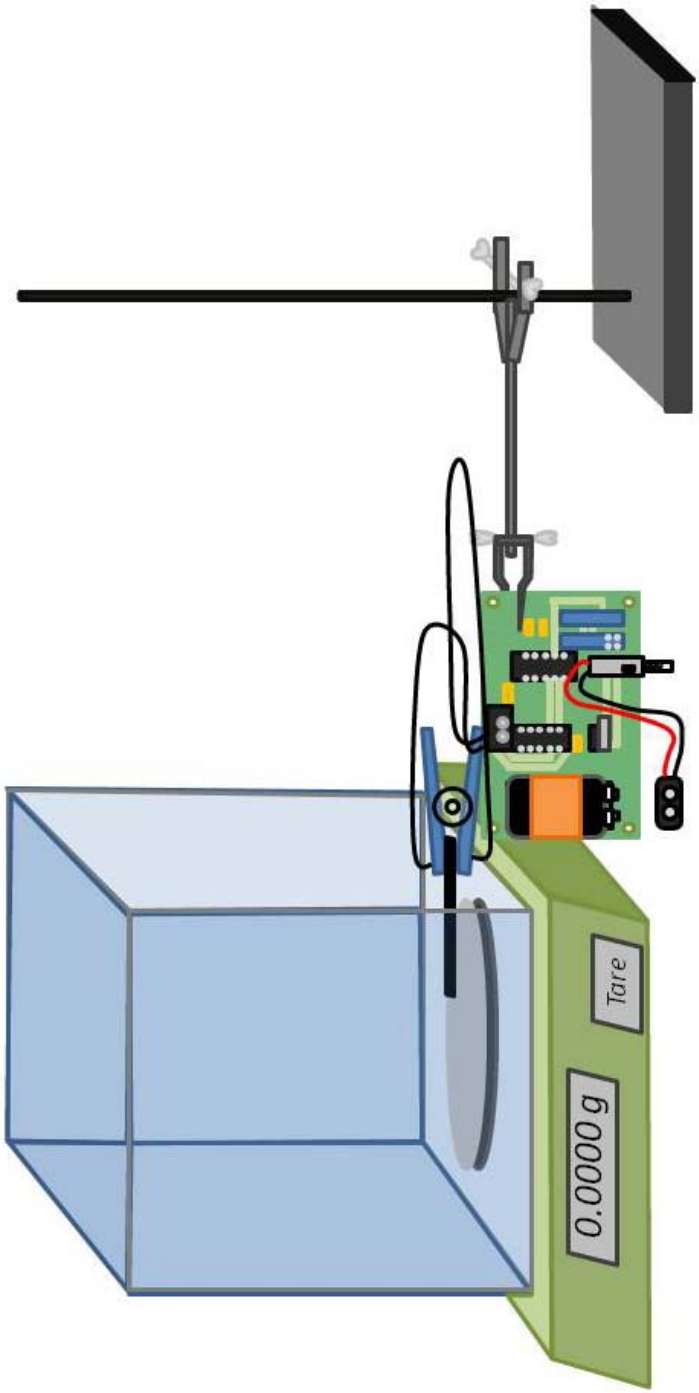

APPENDIX E.

Raw Data from Deflection Testing and Force Testing

Averaged Results of Deflection Testing with ERI Samples (Positive Voltage)		
Trial #	Voltage (V)	Deflection (mm)
1	0	0
2	0.53	0.635
3	0.93	0.889
4	1.42	1.143
5	1.97	1.2446
6	2.56	1.27
7	2.99	1.778
8	3.45	2.159
9	3.95	3.81
10	4.53	6.35
11	5.03	8.636
12	5.56	11.303
13	6.01	12.192
14	5.53	10.668
15	4.96	9.652
16	4.47	8.128
17	4.03	7.493
18	3.51	6.604
19	2.98	5.4356
20	2.5	5.08
21	2.03	4.445
22	1.52	3.429
23	1.36	2.54

Averaged Results of Displacement Testing with ERI Sample (Negative Voltage)		
Trial #	Voltage (V)	Deflection (mm)
1	0	0
2	-0.39	0.508
3	-0.94	0.762
4	-1.57	0.8382
5	-2.09	1.143
6	-2.46	1.27
7	-3.04	1.32
8	-3.47	1.3726
9	-4.06	1.4478
10	-4.54	1.6256
11	-5.03	2.413
12	-5.51	2.794
13	-6.03	3.556
14	-5.54	3.325
15	-5.06	3.215
16	-4.52	3.107
17	-4.09	2.953
18	-3.58	2.667
19	-3.51	2.54
20	-2.99	2.459
21	-2.48	2.413
22	-2	2.3622
23	-1.45	2.032
24	-0.91	2.006
25	-0.55	1.9506
26	-0.1	1.901

Averaged Results of Deflection Testing with Second Lab Fabricated Sample (Positive Voltage)		
Trial #	Voltage (V)	Deflection (mm)
1	0	0
2	0.44	0.508
3	1.07	2.032
4	1.56	2.286
5	2.08	2.489
6	2.5	2.667
7	2.98	3.556
8	3.53	4.95
9	4.11	5.08
10	4.58	7.493
11	4.96	7.289
12	5.58	5.334
13	6.06	5.588
14	5.48	5.08
15	4.97	2.54
16	4.51	-1.27
17	4.06	-2.54
18	3.54	-4.572
19	3.08	-6.35
20	2.54	-7.62
21	2.07	-8.89
22	1.56	-9.906
23	0.93	-10.922
24	0.56	-12.7
25	0.41	-12.954

Averaged Results of Deflection Testing with Second Lab Fabricated Samples (Negative Voltage)		
Trial #	Voltage (V)	Deflection (mm)
1	0	0
2	-0.53	0.254
3	-0.96	0.508
4	-1.43	1.27
5	-1.96	2.667
6	-2.46	3.9624
7	-3.01	5.842
8	-3.47	6.426
9	-3.94	7.62
10	-4.47	7.924
11	-4.94	8.042
12	-5.52	7.9735
13	-6.11	7.62
14	-5.54	7.366
15	-5.11	5.7404
16	-4.52	5.08
17	-4.06	4.826
18	-3.52	4.572
19	-2.93	3.048
20	-2.41	2.921
21	-1.97	2.921
22	-1.4	2.647
23	-1.02	2.54
24	-0.58	2.159
25	-0.47	2.136

Deflection Testing Results of Creased Second Lab Fabricated Sample (Positive Voltage)		
Trial #	Voltage (V)	Deflection (mm)
1	0	0.000
2	0.56	0.305
3	1.14	1.143
4	1.47	1.295
5	1.95	0.762
6	2.48	0.019
7	2.95	0.000
8	3.50	-2.540
9	3.99	-25.643
10	4.48	-33.020
11	5.18	-34.29
12	4.52	-33.02
13	4.10	-32.760
14	3.56	-31.750
15	3.08	-27.940
16	2.56	-25.400
17	2.03	-24.130
18	1.51	-23.851
19	1.08	-22.86
20	0.53	-22.86
21	0.35	-22.86

Deflection Testing Results of Creased Second Lab Fabricated Sample (Negative Voltage)		
Trial #	Voltage (V)	Deflection (mm)
1	-0.09	0.00
2	-0.55	0.254
3	-0.98	0.127
4	-1.56	0.254
5	-2.04	3.937
6	-2.46	8.890
7	-3.00	9.652
8	-3.51	9.906
9	-4.02	9.738
10	-4.58	7.366
11	-4.96	3.048
12	-4.51	2.794
13	-3.97	2.413
14	-3.52	2.1336
15	-3.12	2.032
16	-2.45	1.328
17	-2.12	0.787
18	-1.56	-1.372
19	-1.03	-1.952
20	-0.49	-2.374
21	-0.34	-3.627

Deflection Testing Results of First Lab Fabricated Sample		
Trial #	Voltage (V)	Deflection (mm)
1	0	0
2	0.44	1.270
3	1.01	1.778
4	1.52	2.540
5	1.98	3.023
6	2.52	3.404
7	2.99	4.699
8	3.48	4.953
9	3.97	5.308
10	4.42	5.842
11	4.97	6.350
12	4.57	6.858
13	4.07	6.985
14	3.55	7.036
15	3.05	7.112
16	2.45	7.112
17	2.03	7.366
18	1.57	7.620
19	1.05	8.026
20	0.45	8.382
21	0.00	9.144

Averaged Force Testing Results of First ERI Sample		
Trial #	Voltage (V)	Force (grams)
1	0.00	0.000
2	0.54	0.000
3	1.05	0.002
4	1.55	0.034
5	2.04	0.056
6	2.5	0.145
7	2.93	0.227
8	3.48	0.320
9	3.98	0.441
10	4.50	0.555
11	5.00	0.496
12	4.53	0.395
13	4.09	0.299
14	3.47	0.151
15	2.98	0.080
16	2.51	0.003
17	2.00	0.000
18	1.50	0.000
19	1.00	0.000
20	0.50	0.000
21	0.00	0.000

Averaged Force Testing Results of Second ERI Sample		
Trial #	Voltage (V)	Force (grams)
1	0.00	0.00
2	0.55	0.000
3	1	0.004
4	1.51	0.019
5	2.01	0.02
6	2.54	0.034
7	2.96	0.087
8	3.50	0.104
9	3.96	0.145
10	4.52	0.222
11	4.96	0.282
12	4.51	0.247
13	4.03	0.200
14	3.53	0.161
15	2.99	0.127
16	2.53	0.074
17	1.97	0.026
18	1.56	0.000
19	1.0	0.000
20	0.05	0.000
21	0.00	0.000

Averaged Force Testing Results of Second Lab Fabricated Sample		
Trial #	Voltage (V)	Force (grams)
1	0.02	0.02
2	0.54	0.0400
3	1.02	0.0754
4	1.53	0.0805
5	1.94	0.0964
6	2.51	0.1082
7	3.10	0.1128
8	3.47	0.1283
9	4.04	0.1422
10	4.51	0.1354
11	5.00	0.1153
12	5.51	0.1049
13	5.96	0.0970
14	5.43	0.0905
15	5.02	0.0858
16	4.52	0.0768
17	3.94	0.0589
18	3.49	0.0301
19	2.97	0.0167
20	2.53	0.0044
21	2.18	0.0009
22	1.50	0.0006
23	1.00	0.0001
24	0.53	0.0000

Force Testing Results of Non-uniform Lab Fabricated Sample		
Trial #	Voltage (V)	Force (grams)
1	0.07	0.0074
2	0.53	0.0109
3	0.98	0.0257
4	1.58	0.0367
5	2.05	0.0352
6	2.47	0.051
7	2.93	0.0491
8	3.52	0.0477
9	3.95	0.0495
10	4.47	0.0464
11	5.08	0.0604
12	5.55	0.0831
13	6.06	0.0998
14	5.47	0.0956
15	5.02	0.0737
16	4.46	0.0643
17	4.06	0.0633
18	3.42	0.0858
19	3.03	0.0893
20	2.51	0.0921
21	2.12	0.1186
22	1.54	0.1183
23	0.93	0.1102
24	0.49	0.1018
25	0.34	0.1023